MULTISCALE ANALYSIS AND TEXTURE DESIGN FOR INTERFACES HYDRODYNAMICALLY LUBRICATED BY VARIABLE VISCOSITY AND DENSITY LIQUIDS

A THESIS SUBMITTED TO

THE GRADUATE SCHOOL OF ENGINEERING AND SCIENCE

OF BILKENT UNIVERSITY

IN PARTIAL FULFILLMENT OF THE REQUIREMENTS FOR

THE DEGREE OF

MASTER OF SCIENCE

IN

MECHANICAL ENGINEERING

By

Sarp Ilgaz Koç

August 2024

Multiscale Analysis and Texture Design for Interfaces Hydrodynamically Lubricated by Variable Viscosity and Density Liquids
By Sarp Ilgaz Koç
August 2024

We certify that we have read this thesis and that in our opinion it is fully adequate, in scope and in quality, as a thesis for the degree of Master of Science.

Luca Biancofiore(Advisor)

İlker Temizer(Co-Advisor)

Ali Javili

Stanisław Stupkiewicz

Approved for the Graduate School of Engineering and Science:

Orhan Arıkan
Director of the Graduate School

ABSTRACT

MULTISCALE ANALYSIS AND TEXTURE DESIGN FOR INTERFACES HYDRODYNAMICALLY LUBRICATED BY VARIABLE VISCOSITY AND DENSITY LIQUIDS

Sarp Ilgaz Koç
M.S. in Mechanical Engineering
Advisor: Luca Biancofiore
August 2024

Optimization is fundamental in lubrication, as it is utilized to minimize the energy and durability loss due to friction. To be able to analyze such systems, efficient and accurate mathematical and numerical techniques are required during the modeling and the computation process. Although direct analyses of smooth surfaces for both Newtonian and non-Newtonian flows are well documented in literature, analysis for rough surface textures can be challenging both in terms of modeling and solution. As severity of roughness increases, the accuracy of the available models decreases while the necessary computational cost increases substantially. In this work, a model is developed for piezoviscous, compressible and shear-thinning lubricants using the novel modified viscosity approach alongside homogenization as a mathematical technique for the solution of the Reynolds equation to alleviate the inherent computational difficulties to model roughness. Our results demonstrate good agreement between rough DNS and Reynolds and homogenized results. Furthermore, the developed numerical framework has been used in conjunction with topology optimization algorithm to acquire different surface textures dependent on the fluid rheology. The obtained textures are shown to (i) minimize energy dissipation, or (ii) increase the traction to amplify the grip between the surfaces depending on the respective lubrication application.

Keywords: Reynolds Equation, Homogenization, Piezoviscosity, Compressibility, Shear-Thinning, Topology Optimization, MMA.

ÖZET

NEWTONIAN OLMAYAN AKIŞKANLARLA YAĞLANMIŞ ARAYÜZEYLER İÇİN ÇOK ÖLÇEKLI ANALİZ VE DESEN TASARIMI

Sarp Ilgaz Koç
Makine Mühendisliği, Yüksek Lisans
Tez Danışmanı: Luca Biancofiore
Ağustos 2024

Triboloji çalışmalarında optimizasyon uygulamaları, sürtünmeden dolayı oluşan enerji ve mukavemet kaybını azaltma konusunda oldukça önemlidir. Bu tarz sistemlerin doğru ve tam analizi için, verimli ve hassas matematiksel ve sayısal tekniklerin bütün modelleme ve hesapla sürecinde kullanılabilmesi lazımdır. Pürüzsüz yüzeylerin Newtonian ve Newtonian olmayan akışkanlarla olan analizleri her ne kadar kapsayıcı bir literatüre sahip olsalar da, pürüzlü yüzeylerin analizi hem modelleme hem de çözüm aşamasında zorlu olabilir. Var olan pürüzlerin şiddeti arttıkça, kullanılmakta olan modellerin doğruluğu azalmakla beraber gereken işlemci gücü de bir hayli yükselmektedir. Bu çalışmada, orijinal bir yaklaşım olan Modifiye Viskozite kullanılarak piezoviskoz, sıkıştırılabilir ve kayma incelmesi özelliklerini gösteren yağlayıcılar için geliştirilmiş bir modelin, matematiksel bir teknik olan türdeşleştirme yardımıyla Reynolds denkleminin pürüzlü yüzeyler için verimli cözümünü sağlayacak bir sayısal bir çerçeve yaratılması amaçlanmaktadır. Elde edilen doğrudan sayısal benzetim ve Reynolds denklemi sonuçları arasında birebir uyum bulunmaktadır. Ayrıca, geliştirilmiş sayısal çerçeve bir topoloji optimizasyonu algoritmasıyla birleştirilerek, kullanılan akışkanın reolojisine özel desenler elde etmeye kullanılmıştır. Karakteristik olarak elde edilen desenlerin (i) arayüzeyden olan enerji kaybını azaltabildiği, veya (ii) sürtünmeyi arttırarak, yüzeyler arasındaki tutuşu güçlendirebildiği doğrulanmıştır.

Anahtar sözcükler: Reynolds Denklemi, Türdeşleştirme, Piezoviskozite, Sıkıştırılabilirlik, Kayma İncelmesi, Topoloji Optimizasyonu, MMA.

Acknowledgement

I acknowledge the support of TÜBİTAK for this graduate work under the program No. 1001, Project number 221M576.

Contents

List of Figures

Chapter 1

Introduction

1.1 Motivation

Tribology studies are fundamental for applications that involve a machine element or a multitude parts of importance where lubricated surfaces are contacting each other, since the lubrication enables the prevention of the energy loss due to friction while easing the power transmission on components of high importance [1, 2, 3]. It should also be noted that, the optimization of surface topology and the correct choice of lubricants ought to yield a superior response [4, 5]; provided that the modelling and the necessary analyses are conducted thoroughly for the system of interest. An engineered surface finish, or any structural application of a plausible a texture to an lubrication interface can cause an alteration in performance parameters; whether desired or not [6, 7, 8, 9]. All of which require a comprehensive and rigorous computational or experimental analysis process for the interface of interest.

For a meticulous analysis necessary for a lubrication problem, distinctive models must be developed, valid for the case of interest. Several hardships may be encountered during the modelling process a lubrication interface. Firstly, due to multiscale nature of physics in such systems, theoretical, mathematical and computational problems are posed [10]. With the incorporation of complex fluid rheologies in the study [11, 12] observable in heavily loaded hydrodynamic contacts, the mathematical and theoretical impediments are amplified significantly; creating a need for more sophisticated equations and models. For all of which, since the original derivation by Reynolds [13], The Reynolds Equation in some form suitable for the case, has been employed exhaustively for lubrication studies. Nevertheless, the consideration of apparent roughness in these systems as necessitated by engineering practices under physical circumstances, results in an overall unprecedented complexity for all aspects of analysis [14, 15, 16]. Furthermore, the inclusion of roughness and severity of it might alter the nature of the lubrication problem entirely, invalidating Reynolds Equation as the flow regime can shift towards Stokes, an intricacy discussed in detail in past literature [17, 18, 19, 20].

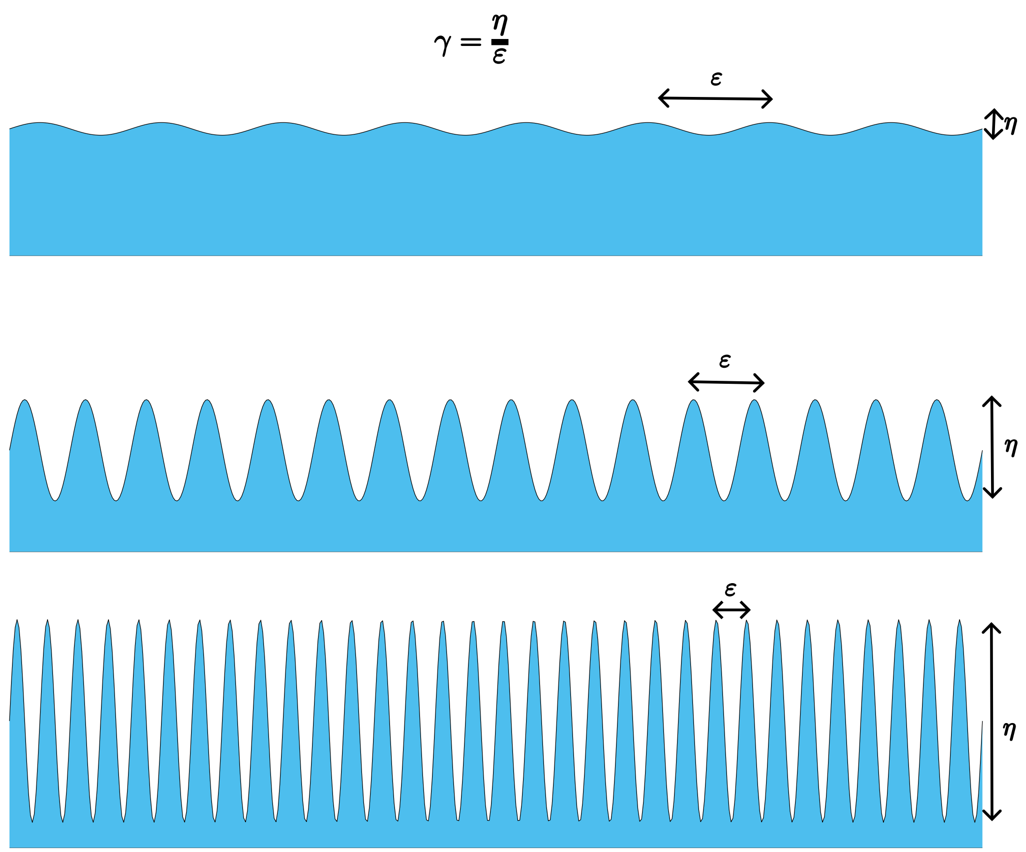

Figure 1.1: Roughness Profile and severity of it, linked to the $\gamma = \eta/\varepsilon$ to distinguish between flow regimes.

The mechanics of a thin fluid film can be analyzed in a extensive manner, both theoretically and computationally, by the Reynolds Equation or its variations for lubrication studies [13, 4, 2]. For Newtonian flows without any deformation on the interface surfaces, that is for contacts with low pressure and small loading [21], The classical Reynolds Equation-explained in detail on Sec. 2.1, is quite valid [1, 2]. However, its reliability suffers substantially when complex rheology fluids are considered [22], typical of heavily loaded contacts where the film pressure is high or machine elements requiring specialized lubricants. The Reynolds Equation fails to suffice also when the previously discussed issue of severity of roughness related to parameter ($\gamma = \eta/\varepsilon \gg 1$) (illustrated on Fig. 1.1) and the dilemma of resolving it [23]; which causes an increase in non-linearity [24] alongside highly possible computational inefficiencies. This issue can be linked to the failure of constant viscosity μ assumption [25], as the massive film pressure and high strain rates, both of which observable in hydrodynamically lubricated bearings, induce non-Newtonian effects [26]. The heavy loading of the contact also leads to alteration of rheological properties, such as thickening due to pressure [27, 2, 22]. Although not being in the scope of this work, the pressure levels mentioned can realistically cause deformations in the interface walls [28, 29, 30]. For a formulation of Reynolds Equation considering the wall deformations in the context of elastohydrodynamic lubrication (EHL), reader is referred to [31] and for a coverage on the effect of surface roughness in EHL [32]. One may also find studies on effect of roughness for high pressure contacts in the context of mixed lubrication in Refs. [33, 14]. Various models based on Reynolds Equation can be identified in the literature for different fluid rheologies and special cases. Nonetheless, many of which, is devised at the cost computational efficiency and the simplicity of Linear Reynolds Equation (LRE), such as Generalised Reynolds Equation (GRE) and its variants; for a detailed discussion see Refs. [34, 35, 36, 37, 38]. The examples can be extended to modified Reynolds equations for power-law obeying non-Newtonian models [39, 40, 41, 42]. Even though it is not part of this research, the viscoelastic effects do also become significant under high pressure. For reference, one may check Refs. [43, 44, 45]. Hence, the development of computationally efficient, robust models that can account for multiple fluid effects relevant for thin film flows while being able to overcome the inherent difficulty of resolving roughness by means of possible simplifications, is a complicated; yet crucial ambition that may facilitate a computational breakthrough for tribology studies.

1.2 Homogenization of Reynolds Equation

One of possible methods used in alleviating the computational issues related to roughness in the context of hydrodynamic lubrication in literature is a mathematical technique called homogenization [46, 47]. Homogenization is widely applied as a mathematical technique when the physical setup has a multi-scale setting, where one of which can be considered a heterogeneity. Within the scope of this work, a rigorous homogenization process for interface roughness is carried out on Reynolds Equation, which was done in detail by employing classical asymptotic expansions [48, 49, 50, 51, 46, 51]. Reader is referred to Refs. [52, 53, 54] for earlier works on Reynolds Equation employing asymptotic expansions to handle roughness effects. Although, the application of homogenization of Reynolds Equation for both incompressible and compressible Newtonian flows is well reviewed [55, 56, 49, 57, 18, 58]. For variable viscosity and density fluids, the literature on Newtonian effects is vast, but the models used are either outdated or not empirically proven to be valid. Some of which, albeit being comprehensive studies, they account for a single fluid effect, which again, may not be realistic in the context of hydrodynamic lubrication [2, 22]. The reader is referred to following papers for engineering applications utilizing homogenization for the analyses regarding porous medium [59, 25, 60, 61, 56, 62, 63]. One may also find example studies on thin film flows with Stokes Equation [59] and Navier-Stokes directly [64, 65]. Moreover, the applications utilizing homogenization of Reynolds Equation, are not enumerated or discussed adequately. Therefore, there is a void in the literature which can be filled by obtaining a model (i) that can combine multiple relevant fluid effects observable in contacts hydrodynamically lubricated by liquids while also accounting for roughness, (ii) with empirically well-verified rheological models.

Since this work is mainly focused on the numerical analyses of lubrication systems such as bearings and transmission machine elements, the high strain rates and immense pressure levels encountered in such thin-film flows dictate the inclusion of potent fluid effects such as piezoviscosity and compressibility [66, 67, 68], alongside the non-Newtonian effect of shear-thinning for a complete study [69, 70, 22]. For the modelling of a piezoviscous, compressible and shear-thinning fluid flow, denoted by PCST acronym for the rest of this work, under a periodic rough texture, homogenization has to be carried out on already complicated governing equations. Combining all of these non-linear rheological fluid effects shown to be apparent in heavily loaded hydrodynamic contacts, where the physical quantities and coefficients would fluctuate continuously due to roughness, a homogenization scheme where governing equation is a higher order Reynolds equation is an appreciably intricate task. Hence, in this work, a simplification is made by exploiting an approach called Modified Viscosity (MV) [22]. By making a dextrous manipulation to the diffusive coefficient of Stokes Equations, a modified term can be obtained for viscosity μ. Provided that one uses this approach for a PCST fluid, or a flow where shear-thinning is existant, Linear Reynolds Equation (LRE) in its most simple format, can be safely used for a wide range of bearing numbers. Being able to use LRE as the governing equation for the homogenization procedure, albeit all the possible non-linearities that may need to be handled, is a substantial ease for the entire scheme. More details can be found on Modified Viscosity Approach on section 2.5 and Ref. [22].

1.3 Surface Texturing

Since the ultimate goal of tribology studies is facilitating the sustainability and the mechanical performance of a machine element of interest, both the rheological properties of the lubricant and the texture of the interface surfaces are degrees of freedom which can be altered. The scope of this work does not involve a discourse on distinctive lubricants, but it aims to numerically optimize the performance parameters related to friction and wear for a set of variable viscosity and density liquids used on hydrodynamically lubricated contacts by exploiting topology optimization. Numerous ways of surface texturing have been devised, both computationally and experimentally, in the context of tribology studies, see the Ref. [71] for a thorough review. Many of the plausible attempts of surface texturing can be attained to the goal of reducing friction and wear for mechanical components [72]. The breakthrough on surface texturing occured with the development of Laser Surface Texturing (LST) [73], enabling both experimental studies on topology optimization and the implementation of computationally obtained textures-see Refs. [72, 71, 74, 75] for a exhaustive review of the literature. On the other hand, there may be high friction applications that should benefit from a boosted traction, such as a Continuously Variable Transmission (CVT) for increased torque [76, 75] or surface textures to increase braking performance in a high pressure environment [77], or increasing skid resistance of tires on road [78]. Appropriately for the current work, PCST fluid is quite fitting for bearing analyses. The structural topology optimization was done previously to bearings of different kind-see Refs. [79, 80, 81, 82]. The homogenization for roughness, was also implemented vastly in literature [83, 84, 85, 86, 27], however, not in conjunction with optimization algorithms to create textures designed for specific performance amplifications relevant in engineering applications-see Refs. [49, 57, 87, 31]. For structural optimization, by solving a series of micro problems, in same fashion as the current work, is generally used in conjunction with Method of Moving Asymptotes (MMA) [88, 89] for details, and the Refs. [49, 57, 90] for the previous implementations; as a precursor to the current work, see Ref. [91]. Large number of studies researching roughness effects involving a non-Newtonian fluids can be found [92], but none of which has used LRE in the context of hydrodynamic lubrication with a piezoviscous, compressible and shear-thinning liquid to best of our knowledge.

Hence, the main goal of this work is the development of a computationally efficient, well-valid and novel homogenized model for variable viscosity and density liquids, which utilizes the Linear Reynolds Equation (LRE) with the aid of modified viscosity (MV) approach, then utilize it in conjunction with an optimization framework for tuning performance parameters such as friction and energy dissipation by attaining textures for different lubrication interfaces. Correct implementation of such a distinguished framework would allow for a thorough analysis of mechanical components, such as bearings used to reduce wear or contact, under roughness or with a periodic texture, with a focus on energy loss minimization and increased grip for applications facilitated by traction amplification. The system response can then be compared to a case without any optimized texture in a computational environment to assess the performance of the attained textures.

1.4 Objective & Structure of the Thesis

The aimed objectives of this thesis can be summed up as follows:

- Develop a homogenized model for a piezoviscous, compressible and shear-thinning fluid using the Linear Reynolds Equation.
- Validate the homogenized model using DNS results for pressure p and traction on walls τ from OpenFoam simulations.
- Use the homogenized model alongside optimization algorithm MMA to create textures which can alter traction and energy dissipation properties.

The thesis starts with the introduction of fluid models, modified viscosity approach and how homogenization is carried out for a PCST fluid in Chapter 2: Models and Methodology.

The homogenized equation, numerical methods and optimization procedure is introduced in Chapter 3: Numerical Methods.

The entirety of homogenized results and DNS validations are illustrated alongside with texture optimization performance assessment in Chapter 4: Results and Discussion.

Lastly, what has been achieved with respect to the Introduction is discussed, reinforced with possible extensions on the subject of the thesis, on Chapter 5:

Conclusions. The additional optimized textures and OpenFoam solvers can be found in the Appendices.

Chapter 2

Models and Methodology

2.1 Reynolds Equation

The Reynolds Equation, in its most general form for a Newtonian fluid flow, can be acquired with a simplification of the Navier-Stokes Momentum Equations and Continuity Equation. For an **incompressible, isoviscous** fluid with dynamic viscosity η_0, the Stress Tensor $\boldsymbol{T}$ can be written as [2],

$$\boldsymbol{T} = -p\boldsymbol{I} + 2\eta_0\boldsymbol{D}, \qquad \boldsymbol{D} = \frac{1}{2}\left(\nabla\boldsymbol{u} + (\nabla\boldsymbol{u})^T\right) \tag{2.1}$$

With $\boldsymbol{D}$ being the Strain Rate Tensor. **Cauchy Momentum Equation**:

$$\rho\frac{d\boldsymbol{u}}{dt} = \rho\boldsymbol{f} + \nabla\cdot\boldsymbol{T}. \tag{2.2}$$

In this expression, $\boldsymbol{f}$ is the body forces acting on the fluid. Substitution of Eq. 2.2 into the Cauchy Momentum Equation, yields **Navier-Stokes Equations**:

$$\rho\frac{d\boldsymbol{u}}{dt} = \nabla p + \nabla\cdot(2\mu\boldsymbol{D}) + \rho\boldsymbol{f}. \tag{2.3}$$

The equation 2.3 has to be simplified to get the equations utilized in Elementary Lubrication Theory. This can be done using the Thin-Film Approximation. The original assumptions made by Reynolds during the derivation [13]

- Continuum description is valid.
- Navier-Stokes equations are valid.
- Compressibility is **ignored**.
- The viscosity is **constant**.
- The film is *thin*
  1. Lubricant flow is free of eddies (Laminar Flow).
  2. Lubricant inertia is **negligible**.

If the following assumptions are applied to 2.3, one should arrive at a set of equations which include terms of order ε; where $\varepsilon = \frac{h}{L}$. Terms of smaller order are assumed to be negligible. This procedure results in the following system of equations:

$$\frac{\partial p}{\partial x} = \eta_0 \frac{\partial^2 u}{\partial y^2}, \tag{2.4}$$

$$\frac{\partial p}{\partial z} = \eta_0 \frac{\partial^2 w}{\partial y^2}, \tag{2.5}$$

$$\frac{\partial u}{\partial x} + \frac{\partial v}{\partial y} + \frac{\partial w}{\partial z}. \tag{2.6}$$

The set of equations given above 2.4 to 2.6 are sufficient in describing the pressure and velocity distribution in a thin film lubricant flow. Hence, the classical Reynolds Equation can be obtained in its 2D form provided that the system is in steady-state $\left(\frac{\partial h}{\partial t} = 0\right)$:

$$\frac{\partial}{\partial x}\left(\frac{h^3}{12\eta_0}\frac{\partial p}{\partial x}\right) + \frac{\partial}{\partial z}\left(\frac{h^3}{12\eta_0}\frac{\partial p}{\partial z}\right) = \frac{\boldsymbol{U}}{2}\frac{\partial h}{\partial x} + \frac{\boldsymbol{W}}{2}\frac{\partial h}{\partial z}. \tag{2.7}$$

Here, $\boldsymbol{U} = \boldsymbol{U_1} + \boldsymbol{U_2}$ and $\boldsymbol{W} = \boldsymbol{W_1} + \boldsymbol{W_2}$ is the sum of the velocities for the of the surfaces in x and z directions respectively. If the lubricant utilized can be assumed to be incompressible and isoviscous, the equation can be rewritten in the following form:

$$\frac{\partial}{\partial x}\left(\frac{h^3}{12}\frac{\partial p}{\partial x}\right)+\frac{\partial}{\partial z}\left(\frac{h^3}{12}\frac{\partial p}{\partial z}\right)=\eta_0\frac{\boldsymbol{U}}{2}\frac{\partial h}{\partial x}+\eta_0\frac{\boldsymbol{W}}{2}\frac{\partial h}{\partial z}. \tag{2.8}$$

However, the assumption that the flow is incompressible and isoviscous may not be correct, as fluid properties are altered due to different effects like temperature and pressure. Furthermore, high strain rates and pressure that are most possibly existent in a system like a bearing, do induce non-linear effects within the lubricant. For such a case, the 2.7 can be used with a slight change:

$$\frac{\partial}{\partial x}\left(\frac{\rho h^3}{12\mu}\frac{\partial p}{\partial x}\right)+\frac{\partial}{\partial z}\left(\frac{\rho h^3}{12\mu}\frac{\partial p}{\partial z}\right)=\frac{\rho\boldsymbol{U}}{2}\frac{\partial h}{\partial x}+\frac{\rho\boldsymbol{W}}{2}\frac{\partial h}{\partial z}. \tag{2.9}$$

In this expression, μ is the non-linear viscosity that is a function of pressure and strain rate within the system $\mu=\mu(p,\dot{\gamma})$.

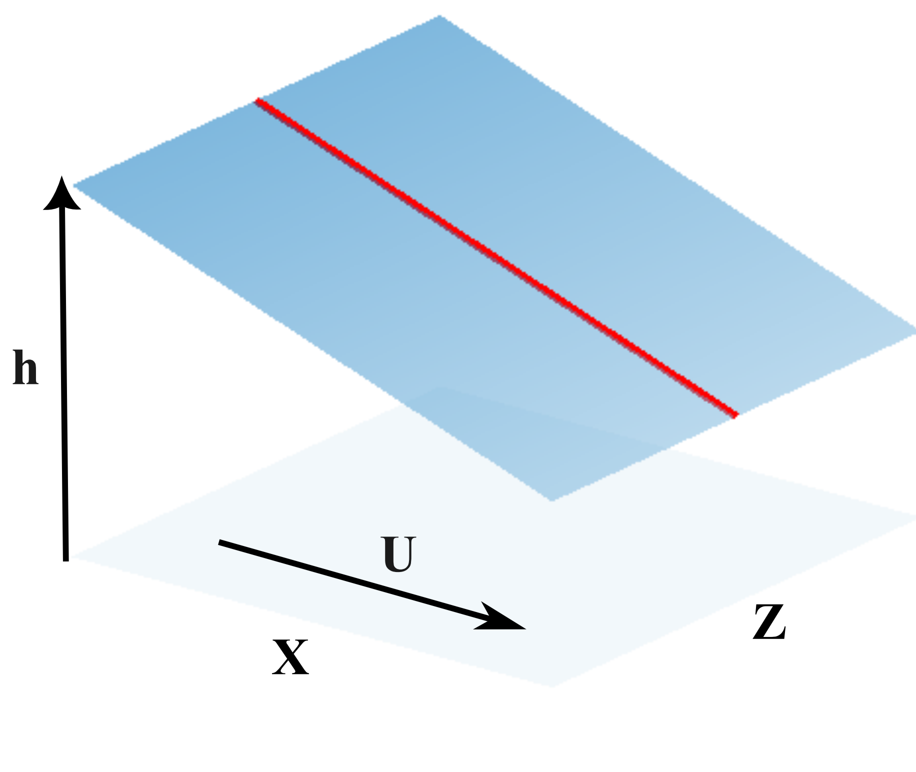

Figure 2.1: 2D Plane Slider setup definition, suitable for Eq. 2.10.

Albeit derivation is done in the format provided on Eq. 2.9, the general analyses can be carried out in tensorial form:

$$-\nabla \cdot \boldsymbol{Q} = -\nabla \cdot \left(-\frac{\rho h^3}{12\mu} \nabla p + \frac{\rho h}{2} \boldsymbol{U} \right) = 0. \tag{2.10}$$

Here, the equation is given for a case where $\boldsymbol{W} = 0$; suitable for all sliding cases studied in this work, as illustrated on Fig. 2.1. On the other hand, the Reynolds Equation shown in Eq. 2.10 can be used for a steady state flow, one may also aim to analyze a squeeze film [22, 49]. For a squeeze film setup, where there is no motion in streamwise and spanwise directions as shown on Fig. 2.2, $\boldsymbol{U} = \boldsymbol{W} = 0$, the equation is,

$$-\nabla \cdot \boldsymbol{Q} = -\nabla \cdot \left(-\frac{\rho h^3}{12\mu} \nabla p \right) = \frac{\partial (\rho h)}{\partial t}. \tag{2.11}$$

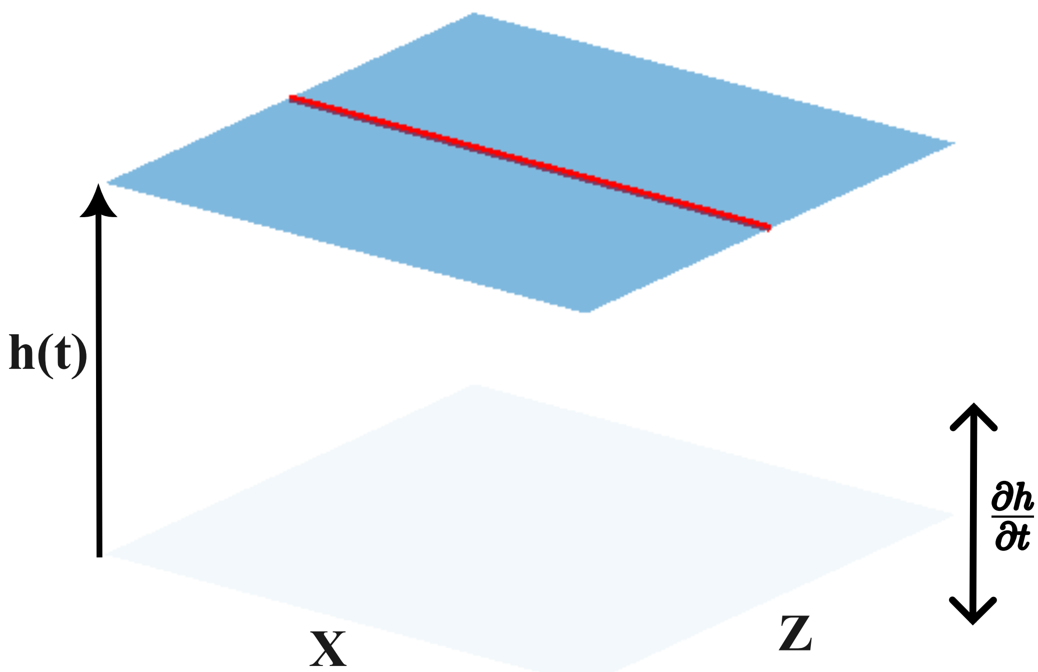

Figure 2.2: 2D Squeeze Film setup definition, suitable for Eq. 2.11.

The forms given in Eqs. 2.10 and 2.11 are highly relevant for the cases described before, however, the results obtained from Eqs. 2.10 and 2.11 are only accurate when the normal strain rate $\frac{\partial u}{\partial x}$ is quite small; therefore, further modifications may be necessary when the non-linearities related to pressure and strain rate are dominant. This problem is applicable specifically for non-Newtonian lubricants. The alleviation of this issue can be done by deriving an entirely new Reynolds Equation, starting from the Eq. 2.1, which may prove to be too challenging depending on the non-linear effects involved in fluid flow. Alternatively, one may try to modify the μ included in Eq. 2.10 to a different form to ensure the validity of the classical Reynolds Equation. To be able to obtain a suitable Reynolds Equation, firstly, one should be able to model these non-linearities with valid and applicable fluid models. The chosen models and the reasoning behind them are provided in the following sections.

2.2 Piezoviscosity

Piezoviscosity can be described as the pressure dependence of the fluid lubricant's viscosity [68, 2]. Even though this increase may not be apparent in all cases, when the pressure is sufficiently large, typical for a heavily loaded hydrodynamic contact, the increase in viscosity follows a non-linear pattern. For the work at hand, the Roelands model has been chosen to account for piezoviscosity in computations [93]:

$$\eta = \eta_0 \left((\ln \eta_0 + 9.67) \left(-1 + \left(1 + \frac{p}{p_0} \right)^Z \right) \right). \tag{2.12}$$

Above, η_0 is the viscosity at atmospheric pressure, p_0 and Z are constants specified by experiments. Roelands model is chosen as it was shown to fit better with empirical data; making it a appropriate choice for numerical analyses of thin film lubrication. One may find the illustration of model prediction on Fig. 2.3 below.

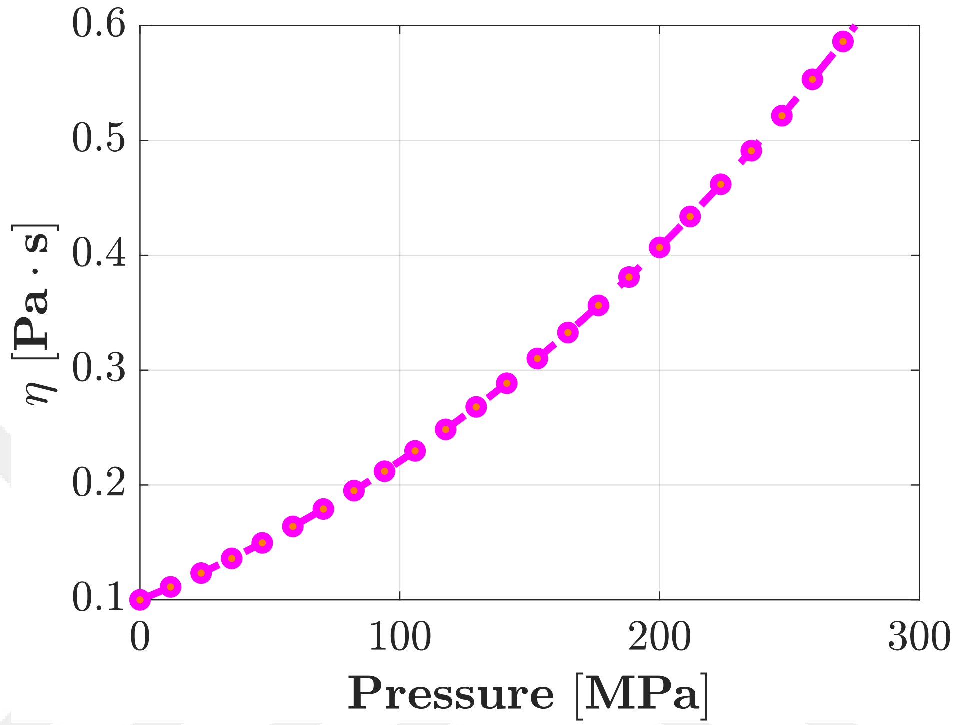

Figure 2.3: Roelands Model Viscosity prediction w.r.t. pressure for $p_0 = 0.15 \cdot 10^9$ Pa and $Z = 0.34$.

2.3 Shear-Thinning

Shear-thinning is an highly relevant non-Newtonian effect; describing the shear stress or strain rate dependency of the fluid viscosity [94, 95]. It is an experimentally observed effect where lubricants undergo a substantial decrease in viscosity due to high strain rates that are found in thin contacts. It can be said that, for piezoviscosity to exist, the shear-thinning should also be effective within the flow, as shear-thinning of a fluid diminishes the dominance of piezoviscosity. Although there are various models utilized in the literature, such as Power Law fluids, the two prominent models used in in the scope of this work are Ree Eyring and Bair-Winer Models. Ree-Eyring relation, was a popular choice in literature due to its simple form [96]:

$$\mu = \frac{\tau_0}{\dot{\gamma}} \sinh\left(\frac{\tau}{\tau_0}\right). \tag{2.13}$$

Main problem with the Ree-Eyring relation is that, increase in shear-stress does not saturate, even after yield point is crossed for the fluid; which is inconsistent with the previous experimental results [97]. On the other hand, the Bair-Winer model is able to alleviate this issue by also taking shear modulus into account. Hence, for this work, Bair-Winer model is used in place of Ree-Eyring, as it agrees better with the empirical results [98]:

$$\mu = \frac{\tau_0}{\dot{\gamma}} \tanh\left(\frac{\eta_0 \dot{\gamma}}{\tau_0}\right). \tag{2.14}$$

Here, $\dot{\gamma}$ is the magnitude of the strain rate, and $\tau = \eta_0 \dot{\gamma}$. The relation 2.14 is valid for high strain rates that are quite important for this study. One may observe the issue explained for 2.13 and compare the predictions of both models in the Fig. 2.4 provided below.

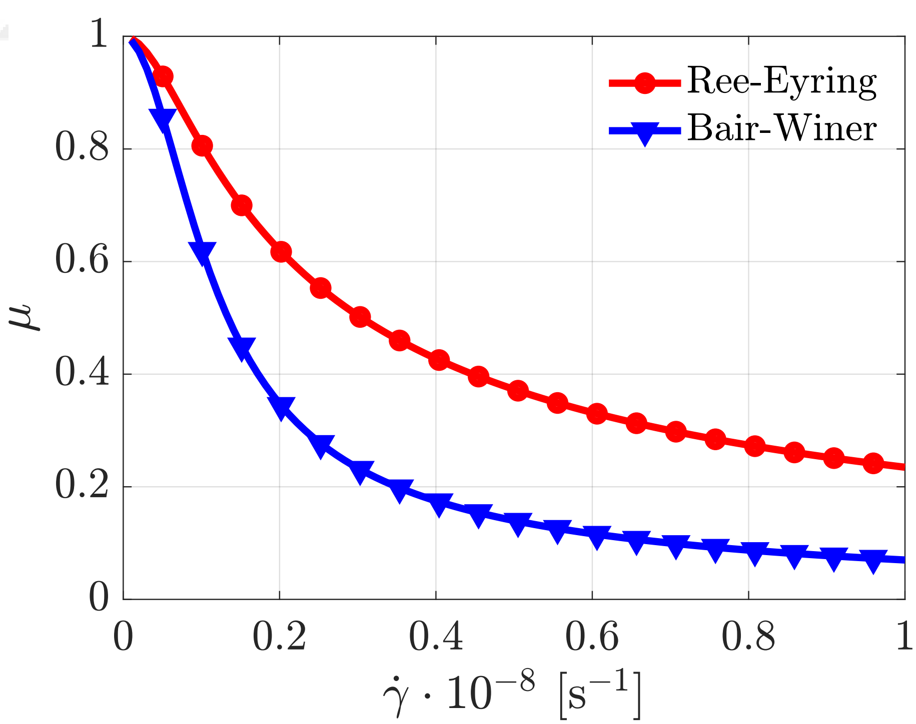

Figure 2.4: Ree-Eyring and Bair-Winer Viscosity prediction with respect to strain rate for $\tau_0 = 7 \cdot 10^6$ Pa.

2.4 Compressibility

Albeit it is of secondary importance for the work at hand, realistically, for pressure magnitudes in which piezoviscosity is important, the compressibility effect for the fluid should also be apparent [99]. The compressibility is taken into account by the usage of Dowson-Higginson Model shown below [100]:

$$\rho = \rho_0 \frac{C_1 + C_2 p}{C_1 + p}. \tag{2.15}$$

Although it is a non-linear effect, its implementation into the numerical framework can be entirely decoupled from viscosity if it is necessary for the solution procedure.

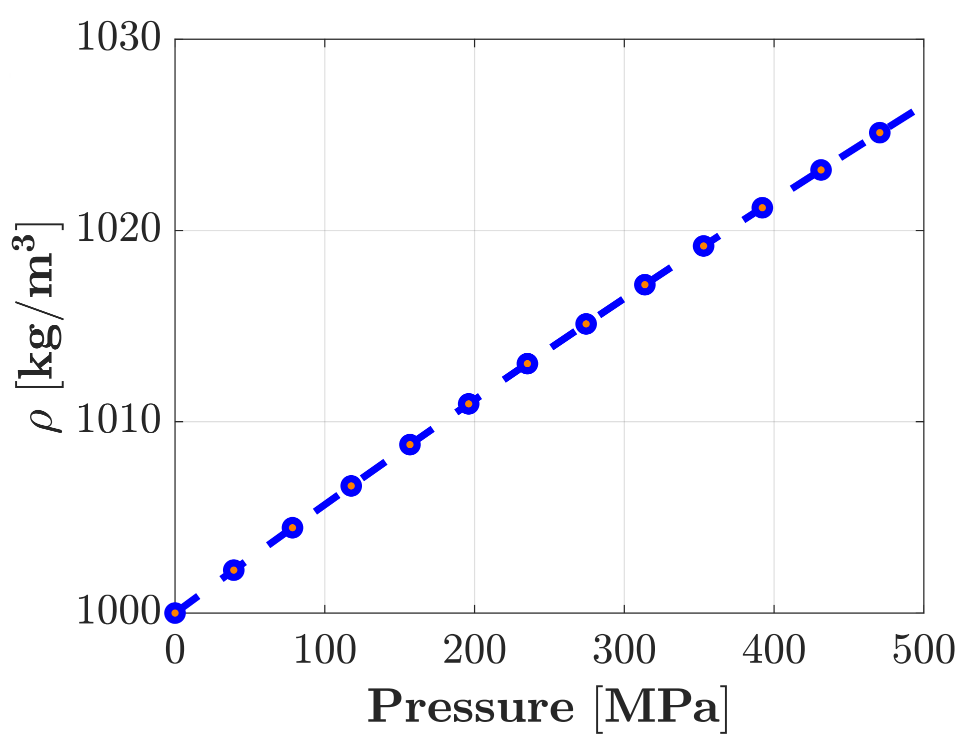

Figure 2.5: Dowson-Higginson Model Density prediction w.r.t. pressure for $\rho_0 = 1000$ kg/m^3, $C_1 = 5.9 \cdot 10^9$ and $C_2 = 1.34$.

2.5 Modified Viscosity Approach

To be able to combine the described fluid effects in the previous section, the higher order models should be utilized, such as generalized Reynolds Equation (GRE) discussed in Sec. 1.2. However, GRE is computationally quite expensive and complex; this situation is worse when non-linear fluid effects are taken into account.

This situation can be alleviated by utilizing a manipulation proposed by [22]. Consider the x-momentum equation obtained from **thin-film approximation**:

$$-\frac{\partial p}{\partial x} + \frac{\partial}{\partial y}\left(\mu \frac{\partial u}{\partial y}\right) = 0. \tag{2.16}$$

By exploiting the equality of strain rate $\frac{\partial u}{\partial y} = \dot{\gamma}_{eq}$ to get

$$-\frac{\partial p}{\partial x} + \frac{\partial \mu}{\partial y}\dot{\gamma}_{eq} + \mu \frac{\partial \dot{\gamma}_{eq}}{\partial y} = -\frac{\partial p}{\partial x} + \left(\mu + \frac{\partial \mu}{\partial \dot{\gamma}_{eq}}\dot{\gamma}_{eq}\right)\frac{\partial^2 u}{\partial y^2} = 0, \tag{2.17}$$

which is used to correct the viscosity due to **strain rate** by following equation:

$$\mu_m = \mu + \frac{\partial \mu}{\partial \dot{\gamma}_{eq}}\dot{\gamma}_{eq}, \qquad \dot{\gamma}_{eq} = \sqrt{\dot{\gamma}_{xy} + \dot{\gamma}_{yz}}. \tag{2.18}$$

Here, the strain rate components in x and z directions $\dot{\gamma}_{xy}$ and $\dot{\gamma}_{yz}$ are respectively defined in their most general form

$$\dot{\gamma}_{xy} = \frac{1}{2\Lambda\mu_m}\frac{\partial p_0}{\partial x}h^2\left(2\chi - 1\right) + \left(U_2 - U_1\right)\frac{1}{h}, \tag{2.19a}$$

$$\dot{\gamma}_{yz} = \frac{1}{2\Lambda\mu_m}\frac{\partial p_0}{\partial z}h^2\left(2\chi - 1\right), \tag{2.19b}$$

in which, p_0 is the macroscopic pressure $\chi = y/h$ which denotes the fraction of the film thickness where the strain rate is evaluated. For cases in which streamwise relative velocity component $\boldsymbol{U} = U_2 - U_1 \neq 0$ the $\dot{\gamma}_{xy} \gg \dot{\gamma}_{yz}$; the spanwise strain rate component can be disregarded. In addition, for $\chi = 0.5$, the value in which error for pressure and load is minimized for a Couette flow [22], the $\dot{\gamma}_{xy}$ expression can be simplified. Therefore, for unidirectional sliding case, the equivalent strain rate can be written as

$$\dot{\gamma}_{eq} = \dot{\gamma}_{xy} = \left| \frac{U_2 - U_1}{h} \right|. \tag{2.20}$$

Nonetheless, it should be emphasized that for a squeeze film case, the ideal location for strain rate evaluation of a shear-thinning flow is given to be $\chi = 0.25$ or $\chi = 0.75$ [22]. Therefore, the simplification shown on Eq. 2.20, won't be possible. More details on the squeeze film setup can be found in Sec. 4.3.3. By correcting the shear-thinning piezoviscous viscosity μ with strain rate, one can use linear Reynolds Equation (LRE) shown on Eq. 2.10 directly for a wide range of bearing numbers. This completely leads to a computational efficiency increase, since Linear Reynolds Equation is the simplest format that can be used in such a cases. By exploiting this approach, homogenization is carried out for a compressible, piezoviscous and shear-thinning fluid flow by directly utilizing linear Reynolds Equation (LRE), which is done in the following Sec. 2.6.

2.6 Piezoviscous, Compressible, Shear-Thinning Reynolds Homogenization

2.6.1 Definitions

Homogenization requires a periodic highly oscillatory heterogeneity, which is separated from macroscopic domain by a scale separation of ε. How small this ε should be, is dependant on the application, and it is explained further at the end of the section.

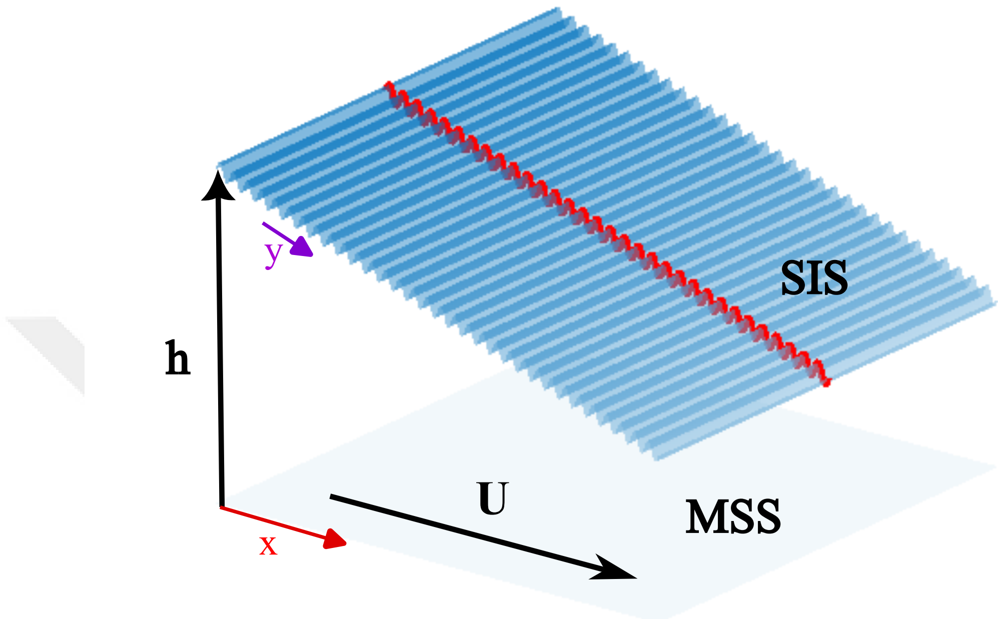

Figure 2.6: Arbitrary Heterogeneous interface for analysis with macro and micro length scales x and y.

Firstly, one may define the length scale and operators [48, 49]:

$$x_\varepsilon = x + \varepsilon y. \tag{2.21}$$

Above, x and y are the macroscopic and microscopic length scale respectively. Following from this definition, one might define ∇ as:

$$\nabla = \nabla_x + \frac{1}{\varepsilon}\nabla_y \tag{2.22}$$

Assuming steady, compressible, piezoviscous and shear-thinning flow, one may define following variables to be used:

$$a_\varepsilon = a(x,y) = \frac{h_\varepsilon^3(x,y)}{12\mu}, \qquad b(x,y) = \frac{h_\varepsilon}{2}, \qquad \rho_\varepsilon = \rho(p). \tag{2.23}$$

Substituting these variables into the Steady Reynolds Equation, the equation to be solved becomes:

$$-(\nabla_x + \frac{1}{\varepsilon}\nabla_y) \cdot \left(-a(x,y)\rho_\varepsilon(\nabla_x + \frac{1}{\varepsilon}\nabla_y)p_\varepsilon + \rho_\varepsilon \frac{h_\varepsilon}{2}\boldsymbol{U}\right) = 0. \tag{2.24}$$

In this expression, the first term in the paranthesis is **Poiseuille** and the latter one is **Couette** term. They are analyzed separately, and the results are than combined using superposition. To start the homogenization procedure, p_ε and ρ_ε are expanded asymptotically as:

$$p_\varepsilon(x,y) = p_0 + \varepsilon p_1 + \varepsilon^2 p_2, \tag{2.25}$$

$$\rho_\varepsilon(x,y) = \rho_0 + \varepsilon \rho_1 + \varepsilon^2 \rho_2. \tag{2.26}$$

Since ρ depends on p, terms provided in Eq. (2.26) can be expanded as follows on the ρ as an example;

$$\begin{aligned} \rho_0 &= \rho(p_0), \\ \varepsilon\rho_1 &= \varepsilon(\frac{\partial \rho}{\partial p}\frac{\partial p}{\partial \varepsilon}), \\ \varepsilon^2\rho_2 &= \varepsilon^2(\rho_0'' p_1^2 + 2\rho_0' p_2). \end{aligned} \tag{2.27}$$

where, $'$ indicates a derivative with respect to the pressure p_0. Finally, we define an important correlary, which is being used in the derivations:

$$\int \nabla \cdot q(y) dy \;=\; 0. \tag{2.28}$$

In this section, all integral domains are the unit cell that will not be denoted explicitly for sake of simplicity. The expression Eq. 2.28 holds for any 1-periodic function q.

2.6.2 Derivation of the Operator Heterogeneous Quantities

$$(\nabla_x + \frac{1}{\varepsilon}\nabla_y) \cdot (a(x,y)\rho_\varepsilon(\nabla_x + \frac{1}{\varepsilon}\nabla_y)) \tag{2.29}$$

Expanding ρ_ε using Eq. (2.26):

$$(\nabla_x + \frac{1}{\varepsilon}\nabla_y) \cdot (a(x,y)(\rho_0 + \varepsilon\rho_1 + \varepsilon^2\rho_2)(\nabla_x + \frac{1}{\varepsilon}\nabla_y)). \tag{2.30}$$

Multiplication in Eq. (2.30) results in the following:

$$\begin{aligned}(\nabla_x(a\rho_0\nabla_x) + \frac{1}{\varepsilon}\nabla_x(a\rho_0\nabla_y) + \varepsilon\nabla_x(a\rho_1\nabla_x) + \nabla_x(a\rho_1\nabla_y) + \ldots \\ \varepsilon^2\nabla_x(a\rho_2\nabla_x) + \varepsilon\nabla_x(a\rho_2\nabla_y) \\ +\frac{1}{\varepsilon}\nabla_y(a\rho_0\nabla_x) + \frac{1}{\varepsilon^2}\nabla_y(a\rho_0\nabla_y) + \nabla_y(a\rho_1\nabla_x) + \frac{1}{\varepsilon}\nabla_y(a\rho_1\nabla_y) + \ldots \\ \varepsilon\nabla_y(a\rho_2\nabla_x) + \nabla_y(a\rho_2\nabla_y)).\end{aligned}$$

Terms with positive powers of ε are all zero as $\varepsilon \longrightarrow 0$. Separating the terms into powers of ε:

$$\frac{1}{\varepsilon^2}(-\nabla_y(a\rho_0\nabla_y)), \tag{2.31}$$

$$\frac{1}{\varepsilon}(-\nabla_x(a\rho_0\nabla_y) - \nabla_y(a\rho_0\nabla_x) - \nabla_y(a\rho_1\nabla_y)), \tag{2.32}$$

$$\frac{1}{\varepsilon^0}(-\nabla_x(a\rho_0\nabla_x) - \nabla_x(a\rho_1\nabla_y) - \nabla_y(a\rho_1\nabla_x) - \nabla_y(a\rho_2\nabla_y)). \tag{2.33}$$

2.6.3 Equations

Multiplying Eqs. (2.31)-(2.32)-(2.33) with $p_\varepsilon = p_0 + \varepsilon p_1 + \varepsilon^2 p_2$ to get final terms and getting rid of the terms with $\varepsilon^{x>0}$

$$-\frac{1}{\varepsilon^2}(\nabla_y(a\rho_0\nabla_y)) \cdot (p_0 + \varepsilon p_1 + \varepsilon^2 p_2), \tag{2.34}$$

$$-\frac{1}{\varepsilon}(\nabla_x(a\rho_0\nabla_y) + \nabla_y(a\rho_0\nabla_x) - \nabla_y(a\rho_1\nabla_y)) \cdot (p_0 + \varepsilon p_1 + \varepsilon^2 p_2), \tag{2.35}$$

$$-(\nabla_x(a\rho_0\nabla_x) + \nabla_x(a\rho_1\nabla_y) + \nabla_y(a\rho_1\nabla_x) + \nabla_y(a\rho_2\nabla_y)) \cdot (p_0 + \varepsilon p_1 + \varepsilon^2 p_2). \tag{2.36}$$

Resulting equations from operations provided above are listed in the respective order:

$$-\frac{1}{\varepsilon^2}\nabla_y(a\rho_0\nabla_y)p_0 - \frac{1}{\varepsilon}\nabla_y(a\rho_0\nabla_y)p_1 - \nabla_y(a\rho_0\nabla_y)p_2, \tag{2.37}$$

$$-\frac{1}{\varepsilon}(\nabla_x(a\rho_0\nabla_y)p_0 + \nabla_y(a\rho_0\nabla_x)p_0 + \nabla_y(a\rho_1\nabla_y)p_0)$$
$$-(\nabla_x(a\rho_0\nabla_y)p_1 + \nabla_y(a\rho_0\nabla_x)p_1 + \nabla_y(a\rho_0\nabla_y)p_1), \tag{2.38}$$

$$-(\nabla_x(a\rho_0\nabla_x)p_0 + \nabla_x(a\rho_1\nabla_y)p_0 + \nabla_y(a\rho_1\nabla_x)p_0 + \nabla_y(a\rho_2\nabla_y)p_0). \tag{2.39}$$

Which yields the following three equations to be worked on for results by combining terms of the same order $(1/\varepsilon^2, 1/\varepsilon, 1)$:

$$-\nabla_y(a\rho_0\nabla_y)p_0 \;=\; 0, \tag{2.40}$$

$$\nabla_y(a\rho_0\nabla_y)p_1 = (-\nabla_x(a\rho_0\nabla_y) - \nabla_y(a\rho_0\nabla_x) - \nabla_y(a\rho_1\nabla_y))p_0, \tag{2.41}$$

$$\nabla_y(a\rho_0\nabla_y)p_2 = (-\nabla_x(a\rho_0\nabla_x) - \nabla_x(a\rho_1\nabla_y) - \nabla_y(a\rho_1\nabla_x) - \nabla_y(a\rho_2\nabla_y))p_0 +$$
$$(-\nabla_x(a\rho_0\nabla_y) - \nabla_y(a\rho_0\nabla_x) - \nabla_y(a\rho_1\nabla_y))p_1. \tag{2.42}$$

In the next section, the obtained equations would be used to obtain homogenized tensor for Poiseuille term of the Reynolds Equation.

2.6.4 Homogenization of Poiseuille Term

Analyzing the Eq. (2.40), one may notice that

$$-\nabla_y \cdot (a\rho_0\nabla_y)p_0 \;=\; 0, \tag{2.43}$$

for this to hold, $p_0 = p_0(x)$. Since the ρ_0 is also defined as $\rho_0(p_0)$, it is also only a function of x. Therefore, the first parameter in the multiscale expansion is *independent* of y

$$p_0 \;=\; p_0(x), \qquad \rho_0 \;=\; \rho_0(x). \tag{2.44}$$

Moving on to the Eq. (2.41), the equation can be written in the following form:

$$-\nabla_y \cdot (a\rho_0\nabla_y)p_1 \;=\; \nabla_y \cdot (a\rho_0\nabla_x)p_0. \tag{2.45}$$

The other terms have vanished, due to previous correlary of $p_0 = p_0(x)$. Manipulating the right hand side:

$$-\nabla_y \cdot (a\rho_0 \nabla_y) p_1 = \nabla_y \cdot (a\rho_0) \cdot \nabla_x p_0. \tag{2.46}$$

Seeking a solution of the form $p_1 \ = \ \boldsymbol{\chi_p} \cdot \nabla_x p_0 - U\mu_0 \boldsymbol{\chi_c}$ where $\boldsymbol{\chi_p}, \boldsymbol{\chi_c}$ stands for a y-periodic vector for Poiseuille term and Couette term respectively. For this section, only the term with χ_p would be included as the other term is ineffective for this particular section. Substituting it into the Eq. (2.46):

$$-\nabla_y \cdot (a\rho_0 \nabla_y) \boldsymbol{\chi_p} \cdot \nabla_x p_0 = \nabla_y \cdot (a\rho_0) \cdot \nabla_x p_0. \tag{2.47}$$

One may cancel out the $\nabla_x p_0$ terms. In addition, the ρ_0 term can also be cancelled out, as it does not depend on y. This leaves the cell problem for Poiseuille contribution:

$$\nabla_y \cdot (a \nabla_y \boldsymbol{\chi_p}) = -\nabla_y \cdot (a). \tag{2.48}$$

Lastly, using Eq. (2.42) to get homogenized equation, many of the terms can be removed due to first correlation from Eq. (2.44):

$$\begin{aligned} \nabla_y \cdot (a\rho_0 \nabla_y) p_2 \ &= \ -(\nabla_x \cdot (a\rho_0 \nabla_x) + \nabla_y \cdot (a\rho_1 \nabla_x) p_0 - \\ (\nabla_x \cdot (a\rho_0 \nabla_y) &+ \nabla_y \cdot (a\rho_0 \nabla_x) + \nabla_y (a\rho_1 \nabla_y)) p_1. \end{aligned} \tag{2.49}$$

Integrating both sides, and utilizing the correlary proposed in Eq. (2.28) by periodicity:

$$\int -\nabla_x \cdot (a\rho_0 \nabla_x p_0) dy - \int \nabla_x \cdot (a\rho_0 \nabla_y p_1) dy = 0. \tag{2.50}$$

For the expression above, manipulating the terms within the integral and substituting the expression for p_1:

$$-\nabla_x \cdot \left[\left(\int a\rho_0 dy \right) \nabla_x p_0 \right] + -\nabla_x \cdot \left[\left(\int a\rho_0 \nabla_y \boldsymbol{\chi_p} dy \right) \nabla_x p_0 \right]. \tag{2.51}$$

Hence, one may write homogenized tensor for Poiseuille term $\boldsymbol{A}$:

$$\boldsymbol{A} = \left(\int (a\boldsymbol{I} + a\nabla_y \boldsymbol{\chi_p}) dy \right). \tag{2.52}$$

The full equation would be written in the end, after contributions from the Couette term are also included.

2.6.5 Homogenization of Couette Term

Starting from the equation

$$-(\nabla_x + \frac{1}{\varepsilon}\nabla_y) \cdot (\rho_\varepsilon \frac{h_\varepsilon}{2}\boldsymbol{U}), \tag{2.53}$$

and using the expansion shown in Eq. (2.26) and making the substitution $\frac{h_\varepsilon}{2} = b$ the equation can be modified to the following form:

$$-\boldsymbol{U}(\nabla_x + \frac{1}{\varepsilon}\nabla_y) \cdot (b\rho_0 + \varepsilon b\rho_1 + \varepsilon^2 b\rho_2). \tag{2.54}$$

One may write down individual terms:

$$-U(\nabla_x(b\rho_0) + \varepsilon\nabla_x(b\rho_1) + \varepsilon^2\nabla_x(b\rho_2) + \frac{1}{\varepsilon}\nabla_y(b\rho_0) + \nabla_y(b\rho_1) + \varepsilon\nabla_y(b\rho_2)). \tag{2.55}$$

Terms containing positive power of ε go to zero as $\varepsilon \ll 1$:

$$-\boldsymbol{U}(\nabla_x \cdot (b\rho_0) + \nabla_y \cdot (b\rho_1) + \frac{1}{\varepsilon}\nabla_y \cdot (b\rho_0)). \tag{2.56}$$

Starting with the term of $\frac{1}{\varepsilon}$, it would be equated to left hand side term in Eq. (2.46) as the chosen substitution of p_1 also accounts for Couette contribution:

$$-\nabla_y \cdot (a\rho_0\nabla_y)p_1 \;=\; \boldsymbol{U}\nabla_y(b\rho_0). \tag{2.57}$$

Substituting the $p_1 = \boldsymbol{\chi_p} \cdot \nabla_x p_0 - \boldsymbol{U}\mu_0\boldsymbol{\chi_c}$ and only using the second term in it now:

$$\nabla_y \cdot (a\rho_0\nabla_y)(\boldsymbol{\chi_c} \cdot \mu_0 U) = \boldsymbol{U}\rho_0\nabla_y \cdot b. \tag{2.58}$$

Since it has already been established that $\rho_0 = \rho_0(x)$, it can also be said that $\rho_0, \mu_0 = \rho_0(x), \mu_0(x)$. Therefore, they are separated from the ∇_y as it is done in the Eq. (2.58). Taking out all of these terms outside and simplifying leads to the following cell problem for Couette Term:

$$\nabla_y \cdot (a \nabla_y \boldsymbol{\chi_c}) = \nabla_y b. \tag{2.59}$$

Remaining terms of order ε^0 in Eq. (2.56) are equated to left hand side of Eq. (2.49); with the exclusion of terms not involving p_1,

$$\begin{aligned} \nabla_y \cdot (a\rho_0 \nabla_y) p_2 = \boldsymbol{U} \nabla_x \cdot (b\rho_0) + \boldsymbol{U} \nabla_y \cdot (b\rho_1) + \nabla_x \cdot (a\rho_0 \nabla_y) p_1 + \\ \nabla_y \cdot (a\rho_0 \nabla_x) p_1 + \nabla_y \cdot (a\rho_1 \nabla_y) p_1, \end{aligned} \tag{2.60}$$

if we integrate both sides with respect to y, and utilize the correlation proposed in Eq. (2.28), one is left with following:

$$\boldsymbol{U} \int \nabla_x \cdot (b\rho_0) dy + \int \nabla_x \cdot (a\rho_0 \nabla_y) p_1 dy = 0. \tag{2.61}$$

If one employs the substitution for $p_1 = \boldsymbol{\chi_p} \cdot \nabla_x p_0 - \boldsymbol{U} \mu_0 \boldsymbol{\chi_c}$ with only second term, and manipulating the terms within the integrals:

$$\nabla_x \cdot \boldsymbol{U} \left(\int b\rho_0 dy \right) + \nabla_x \cdot U \left(\int a\rho_0 \mu_0 \nabla_y \boldsymbol{\chi_c} dy \right). \tag{2.62}$$

After simplifying, the homogenized tensor for Couette term $\boldsymbol{C}$, with $b = \frac{h_0}{2}$ can be written as:

$$\boldsymbol{C} = \left(\int (b\boldsymbol{I} + a \nabla_y \boldsymbol{\chi_c}) dy \right). \tag{2.63}$$

The terms can now be combined to write down the macroscopic flux term. Results obtained in Eqs. (2.52)-(2.63) are employed with this purpose.

2.6.6 Summary of Homogenization

Thus, the **cell problems** for Poiseuille and Couette terms can be written as follows

$$-\nabla_y \cdot (a\nabla_y \boldsymbol{\chi_p}) = \nabla_y a, \tag{2.64}$$

$$\nabla_y \cdot (a\nabla_y \boldsymbol{\chi_c}) = \nabla_y b. \tag{2.65}$$

Additionally, the **homogenized tensors $\boldsymbol{A}$ and $\boldsymbol{C}$** being:

$$\boldsymbol{A} = \int \left(\frac{h^3}{12\mu}\boldsymbol{I} + \frac{h^3}{12\mu}\nabla_y \boldsymbol{\chi_p} \right) dy, \tag{2.66}$$

$$\boldsymbol{C} = \int \left(\frac{h}{2}\boldsymbol{I} + \frac{h^3}{12\mu}\nabla_y \boldsymbol{\chi_c} \right) dy. \tag{2.67}$$

With macroscopic flux being:

$$\boldsymbol{Q} \;=\; -\boldsymbol{A}\rho_0 \nabla_x p_0 + \rho_0 \boldsymbol{C}\boldsymbol{U}. \tag{2.68}$$

Resulting in the **Homogenized Reynolds Equation**:

$$-\nabla_x \cdot \boldsymbol{Q} \;=\; \nabla_x \cdot (-\boldsymbol{A}\rho_0 \nabla_x p_0 + \rho_0 \boldsymbol{C}\boldsymbol{U}) \;=\; 0. \tag{2.69}$$

It should be highlighted that compressible pressure dependent density $\rho = \rho_0(p)$ stays as a macroscopic quantity; and need not to be incorporated into cell problems. For a Newtonian fluid flow, the homogenized tensors $\boldsymbol{A}$ and $\boldsymbol{C}$ were:

$$\boldsymbol{A} = \int \left(\frac{h^3}{12}\boldsymbol{I} + \frac{h^3}{12}\nabla_y \boldsymbol{\chi_p} \right) dy, \tag{2.70}$$

$$\boldsymbol{C} = \int \left(\frac{h}{2}\boldsymbol{I} + \frac{h^3}{12}\nabla_y \boldsymbol{\chi_c} \right) dy. \tag{2.71}$$

Hence, only modification necessary for the homogenization of a PCST fluid flow is the addition of viscosity $\mu = \mu(x, y, p)$ into the cell problems of Eq. 2.64, 2.65 with tensors of Eq. 2.66 and 2.67. This significantly eases the numerical implementation as the non-linearities only require handling on the macroscale, with the aid of any iterative scheme.

2.7 Shear-Stress Modeling

The shear-stress is important for this work, as it is directly related to the friction existant in the interface. It can be directly used for minimization or maximization of the friction in the interface; either for maximizing the grip or reducing the energy loss. Therefore, it should be modeled by taking surface properties into account. Homogenization enables one to obtain expressions for shear-stress on either **moving smooth (MSS)** or **stationary inclined surfaces (SIS)** as defined in the Fig. 2.7 below.

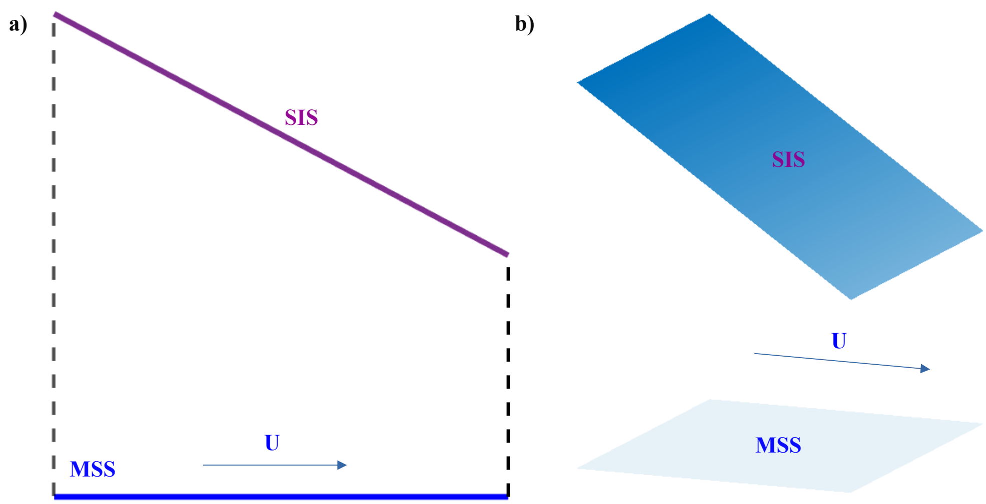

Figure 2.7: Plane Slider interface surface definition, shown in 1D at part a) and 2D at part b). $\boldsymbol{U}$ indicates the constant surface velocity of MSS (Moving Smooth Surface).

The macroscopic traction $\bar{\boldsymbol{T}}$, can be defined using the homogenized tensors $\bar{\boldsymbol{D}}$ and $\bar{\boldsymbol{F}}$, (For the derivation of the tractions, see Ref. [87]) which are defined as follows for MSS and SIS respectively:

$$\bar{\boldsymbol{T}}_{\boldsymbol{MSS}} = \boldsymbol{D}\nabla_x p_0 + \boldsymbol{F}\boldsymbol{U}, \tag{2.72}$$

$$\bar{\boldsymbol{T}}_{\boldsymbol{SIS}} = \boldsymbol{D}\nabla_x p_0 - \boldsymbol{F}\boldsymbol{U}. \tag{2.73}$$

Above, the homogenized tensors $\bar{\boldsymbol{D}}$ and $\bar{\boldsymbol{F}}$ can be defined using the cell problem solutions $\nabla_y \chi_c$, $\nabla_y \chi_p$ of Eq. 2.64 and Eq. 2.65:

$$\boldsymbol{D} = \left\langle \left(\frac{h}{2}\boldsymbol{I} + \frac{h^3}{12\mu}\nabla_y \boldsymbol{\chi_c}\right)\left(\boldsymbol{I} + \nabla_y \boldsymbol{\chi_p}\right)^T \right\rangle, \tag{2.74}$$

$$\boldsymbol{F} = \left\langle \frac{\mu}{h}\boldsymbol{I} + \frac{h^3}{12\mu}\left(\nabla_y \boldsymbol{\chi_c} \nabla_y \boldsymbol{\chi_p}\right)^T \right\rangle. \tag{2.75}$$

Above, the stress factor tensor $\boldsymbol{D} = \boldsymbol{C}^T$. Nonetheless, it should also be indicated that, for direct usage of LRE on smooth and rough interfaces, the tensors are reduced to $\boldsymbol{D} = \frac{h}{2}\boldsymbol{I}$ and $\boldsymbol{F} = \frac{\mu}{h}\boldsymbol{I}$. Moreover, one may find the equations used for wall tractions on MSS and SIS for DNS results; to be compared to Eqs. 2.72 and 2.73:

$$\boldsymbol{\tau} = \boldsymbol{\sigma}\boldsymbol{n} = -\left(\frac{\partial u}{\partial y} + \frac{\partial v}{\partial x}\right)\mu, \tag{2.76}$$

$$\boldsymbol{\tau} = \boldsymbol{\sigma}\boldsymbol{n} = \left(\frac{\partial u}{\partial y} + \frac{\partial v}{\partial x}\right)\mu + p_0\frac{dh_0}{dx}. \tag{2.77}$$

In the above expressions, $\boldsymbol{\sigma} = -p_0\boldsymbol{I} + \boldsymbol{\tau}$, and $\boldsymbol{n}$ is the surface normal vector, respectively can be defined in the following manner for MSS and SIS,

$$\boldsymbol{n}_{MSS} = \begin{vmatrix} 0 \\ -1 \\ 0 \end{vmatrix}, \qquad \boldsymbol{n}_{SIS} = \begin{vmatrix} -\frac{dh_0}{dx} \\ 1 \\ 0 \end{vmatrix}, \tag{2.78}$$

which leads to the expressions provided in the Eqs. 2.76 and 2.77 when substituted. The traction validation between DNS, LRE and homogenized LRE can be found in Sec. 4.2.3.

2.8 Dissipation Modeling

2.8.1 Plane Slider Dissipation Modelling

For optimization, another possible important tribology application in a hydrodynamic contact is minimizing energy dissipation. Following a similar approach to one done on the previous section on shear stress Sec. 2.7, the total or pointwise dissipation can be defined in tensorial form by once again inducing the homogenization. The energy dissipation Π through the interface is defined on **macroscale** as an integral quantity [87]:

$$\Pi = \int_{\mathcal{L}} (\nabla p_0 \cdot \boldsymbol{A} \nabla_x p_0 + \boldsymbol{U} \cdot \boldsymbol{F} \boldsymbol{U})\, da \geq 0. \tag{2.79}$$

In this expression, $\boldsymbol{A}$ and $\boldsymbol{F}$ are **homogenized tensors** in their alternative forms; modified for a piezoviscous, shear-thinning and compressible fluid flow [87]:

$$\boldsymbol{A} = \langle (\boldsymbol{I} + \nabla_y \boldsymbol{\chi}_{\boldsymbol{p}}) \left(\frac{h^3}{12\mu} \boldsymbol{I} + \frac{h^3}{12\mu} \nabla_y \boldsymbol{\chi}_{\boldsymbol{p}}^T \right) \rangle, \tag{2.80}$$

$$\boldsymbol{F} = \langle \frac{\mu}{h} \boldsymbol{I} + \frac{h^3}{12\mu} \nabla_y \boldsymbol{\chi}_{\boldsymbol{c}} \left(\nabla_y \boldsymbol{\chi}_{\boldsymbol{c}} \right)^T \rangle. \tag{2.81}$$

An important corollary can be reached by analysing the terms for the **pointwise dissipation** that can be separated into components at each cell:

$$\phi = \phi_A + \phi_F, \qquad \phi_A = \nabla_x p_0 \cdot \boldsymbol{A} \nabla_x p_0, \qquad \phi_F = \boldsymbol{U} \cdot \boldsymbol{F} \boldsymbol{U}. \tag{2.82}$$

Here, ϕ_A denotes Poiseuille and ϕ_F Couette contribution to dissipation respectively. While Poiseuille term can be increased and decreased at will with specific micro-textures, the Couette contribution amplifies substantially when the texture is not *smooth*. Therefore, any application of periodic micro-texture onto the surface would lead to the maximization of ϕ_F. Limitations caused by this problem is further discussed in 4.3.

2.8.2 Squeeze Film Energy Dissipation Minimizing Principle

As explained briefly in the 2.8.1, while the governing equations and terms for energy dissipation ϕ remain unchanged, as provided on Eq. 2.82, the squeeze film allow for the diminishing of the ϕ_F term; due to 0 streamwise and spanwise velocities U_x and U_z respectively. This allows for a case in which Eq. 2.82 can be rewritten as

$$\phi = \phi_A \quad , \quad \phi_A = \nabla_x p_0 \cdot \boldsymbol{A} \nabla_x p_0, \tag{2.83}$$

where ϕ_A is a term that is both maximizable and minimizable by applying a periodic texture to the interface. However, texture optimization is carried out on a single point of the domain where ∇p_0 and h_0 values are taken from as explained on Sec. 3.5; therefore, the obtained texture may not reflect the ideal response for another point in the analysis domain, causing a possible energy dissipation maximization in total instead of a decrease. By utilizing the finite element formulation for the optimization framework, a principle is obtained for how energy dissipation minimization can be achieved so that the attained total energy dissipation ϕ would be smaller than smooth surface energy dissipation ϕ_0. If we start by defining the LRE for a squeeze film flow, following the notation of [87]:

$$-\nabla_x \cdot \boldsymbol{Q} = \frac{\partial h}{\partial t}, \quad \boldsymbol{Q} = -\boldsymbol{A} \nabla_x p_0 \tag{2.84}$$

And defining a functional, representative of total energy dissipation over domain as J while also denoting the:

- J_0 indicating the smooth energy dissipation
- $\bar{J}$ indicating the optimized energy dissipation
- J indicating the true energy dissipation

With these, one can define the above three quantities in the following form, obtained in a identical fashion to weakening applied to Reynolds Equation in

Sec. 3.2:

$$J_0 = \int_{\partial\Omega} (-p_0)\,\boldsymbol{Q}\cdot\boldsymbol{m}dl + \frac{1}{2}\int_{\Omega} \boldsymbol{G_0}\cdot\boldsymbol{A_0}\boldsymbol{G_0}da + \int_{\Omega} p_0\frac{\partial h}{\partial t}da, \tag{2.85}$$

$$\bar{J} = \int_{\partial\Omega} (-p_0)\,\boldsymbol{Q}\cdot\boldsymbol{m}dl + \frac{1}{2}\int_{\Omega} \boldsymbol{G_0}\cdot\boldsymbol{A}\boldsymbol{G_0}da + \int_{\Omega} p_0\frac{\partial h}{\partial t}da, \tag{2.86}$$

$$J = \int_{\partial\Omega} (-p)\,\boldsymbol{Q}\cdot\boldsymbol{m}dl + \frac{1}{2}\int_{\Omega} \boldsymbol{G}\cdot\boldsymbol{A}\boldsymbol{G}da + \int_{\Omega} p\frac{\partial h}{\partial t}da. \tag{2.87}$$

Here, $\boldsymbol{G} = \nabla_x p_0$ and the first integral in each equation can also be defined to be objective dissipation ϕ:

$$\phi_0 = \int_{\Omega} \boldsymbol{G_0}\cdot\boldsymbol{A_0}\boldsymbol{G_0}da, \tag{2.88}$$

$$\bar{\phi} = \int_{\Omega} \boldsymbol{G_0}\cdot\boldsymbol{A}\boldsymbol{G_0}da, \tag{2.89}$$

$$\phi = \int_{\Omega} \boldsymbol{G}\cdot\boldsymbol{A}\boldsymbol{G}da. \tag{2.90}$$

One may exploit the fact that the $\frac{\partial h}{\partial t}$ can be substituted by Eq. 2.84 for the $\boldsymbol{Q}$ for altering the expressions further. In addition, provided that $\bar{\phi} > \phi_0$, that is if the optimization aims to *maximize* the dissipation, and a substitution alongside a manipulation is done in the following manner for final term on Eqs. 2.85, 2.86 and 2.87:

$$p_0\frac{\partial h}{\partial t} = p_0\left[-\nabla_x\cdot\left(\boldsymbol{A_0}\boldsymbol{G_0}\right)\right] = \nabla_x\left(p_0\left(\boldsymbol{A_0}\boldsymbol{G_0}\right)\right) - \boldsymbol{G_0}\cdot\boldsymbol{A_0}\boldsymbol{G_0}. \tag{2.91}$$

Combining all of these priorly described substitutions and applying the Gauss Divergence Theorem [101] on all of the first terms in Eqs. 2.85, 2.86 and 2.87 to get:

$$\int_{\partial\Omega} (-p_0)\,\boldsymbol{Q}\cdot\boldsymbol{m}dl = \int_{\Omega} -\nabla_x\cdot\left(p_0\boldsymbol{Q}\right)da. \tag{2.92}$$

Similarly, the term $\nabla_x\left(p_0\left(\boldsymbol{A_0}\boldsymbol{G_0}\right)\right)$ in Eq. 2.91 can be written as $\nabla_x\cdot\left(-p_0\boldsymbol{Q}\right)$. When all of which provided above substituted back into the Eqs. 2.85, 2.86 and

2.87 respectively, one is left with:

$$J = -\frac{1}{2}\int_{\Omega} \boldsymbol{G} \cdot \boldsymbol{A}\boldsymbol{G} da = -\frac{1}{2}\phi, \tag{2.93}$$

$$\bar{J} = \frac{1}{2}\int_{\Omega} \boldsymbol{G_0} \cdot \boldsymbol{A}\boldsymbol{G_0} da - \int_{\Omega} \boldsymbol{G_0} \cdot \boldsymbol{A_0}\boldsymbol{G_0} da = \frac{1}{2}\bar{\phi} - \phi_0. \tag{2.94}$$

Since $J > \bar{J}$ due to pressure increase of applied texture, one may write down the following inequality:

$$-\frac{1}{2}\phi > \frac{1}{2}\bar{\phi} - \phi_0. \tag{2.95}$$

From the derivation above, it is found that optimization procedure should *maximize* the ϕ_0 to be $\bar{\phi}$, so that the energy dissipation minimization may be achieved. This is proven to be from the governing inequality shown below:

$$\phi < 2\phi_0 - \bar{\phi}, \tag{2.96}$$

which indicates that for any arbitrary dissipation maximizing surface, the "true" response of this optimized texture would actually may lead to a energy dissipation minimizing surface such that $\phi < \phi_0$. From the inequality, it is also apparent that this holds only for the case for which $\bar{\phi} > \phi_0$. The results acquired by utilizing the principle provided in Eq. 2.96 can be found on Sec. 4.3.3.

Chapter 3

Numerical Methods

3.1 Homogenized Reynolds Equation

When the analyzed microscopic interface is entirely smooth as illustrated in Fig. 2.1, **Linear Reynolds Equation** can be used directly due to viscosity correction described in the section 2.5. This modification enables one to alleviate the possible computational difficulties associated with the inclusion of a PCST fluid effects, and directly employ the following linear format:

$$-\nabla_x \cdot \left(-\frac{\rho_0 h^3}{12\mu} \nabla_x p_0 + \frac{\rho_0 h}{2} \boldsymbol{U} \right) \;=\; 0. \tag{3.1}$$

However, when the analysis is carried out on a texture that is *rough* the usage of Eq. 3.1 becomes computationally inefficient as it requires highly refined mesh to get accurate results. In the scope of this research, the roughness in micro scale is assumed to be periodic to exploit homogenization approach elaborated in the Sec. 2.6. For validation of this approach, a sinusoidal roughness is applied to the smooth interface of the form: $h = h_0 + a \sin(\omega x/L)$. Where a and ω are the amplitude and frequency of the roughness respectively.

Hence, expectancy is that, as $\omega \longrightarrow \infty$, the **Homogenized Reynolds Equation** should yield a matching result to the LRE solution for an arbitrary periodic rough interface,

$$-\nabla_x \cdot (-\rho_0 \boldsymbol{A} \nabla_x p_0 + \rho_0 \boldsymbol{C} \boldsymbol{U}) \ = \ 0. \tag{3.2}$$

The Eqs. 3.1 and 3.2 are solved in the MATLAB environment on the setup shown in Fig. 3.1 as shown below. using an in-house code for different geometries using Galerkin Finite Element method, which described briefly in Sec. 3.2. In the context of lubrication, finite volume and finite difference methods are generally more widespread, however, the variational basis of finite elements for optimization purposes provides a powerful numerical advantage-see Refs. [102, 103] for explanation on its multiscale implementation, and [104, 105] for hydrodynamic lubrication examples other than [49, 57, 87]; all of which are previous works utilizing the earlier versions of the current framework developed for this study.

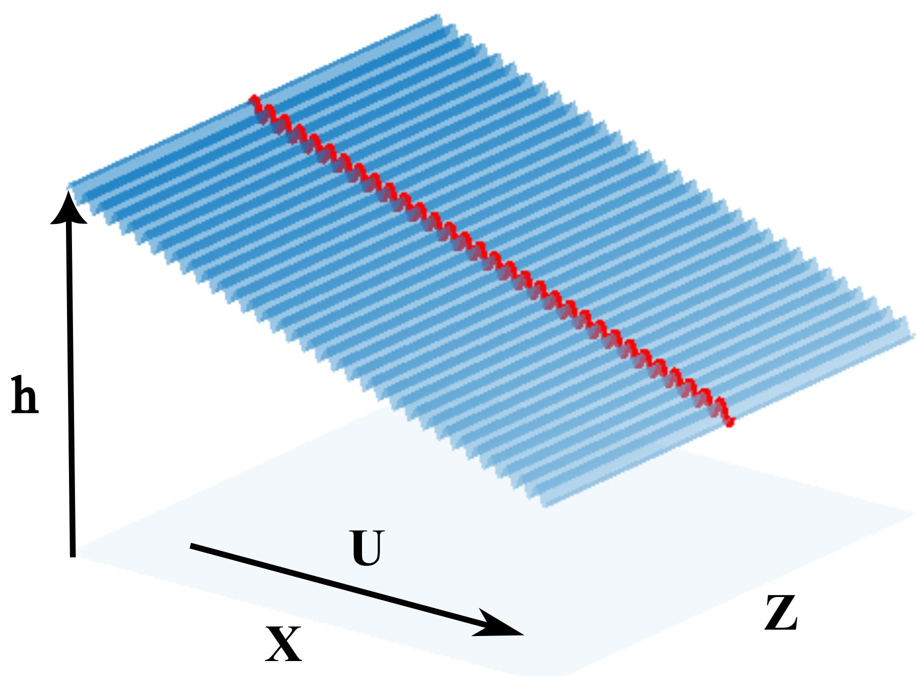

Figure 3.1: Heterogeneous domain representation for a plane slider, to be used on Eqs. 3.1 and 3.2.

3.2 Finite Element Discretization

Finite element discretization is carried out in a similar fashion shown below for Reynolds Equation, for all necessary computations in this work. Derivation of Homogenized Reynolds Equation in its weak form, where η is a test function, can be found below:

$$\int_{\Omega} \eta \left[\nabla_x \cdot \left(\rho_0 \boldsymbol{A} \nabla_x p_0 - \rho_0 \boldsymbol{C} \boldsymbol{U} \right) \right] d\Omega = 0. \tag{3.3}$$

The above expression can be rewritten in the following fashion, by exploiting the property of divergence operator,

$$\int_{\Omega} \nabla_x \cdot \left(\eta \rho_0 \boldsymbol{A} \nabla_x p_0 - \eta \rho_0 \boldsymbol{C} \boldsymbol{U} \right) d\Omega - \int_{\Omega} \nabla_x \eta \cdot \left(\rho_0 \boldsymbol{A} \nabla_x p_0 - \rho_0 \boldsymbol{C} \boldsymbol{U} \right) d\Omega = 0, \tag{3.4}$$

one may further modify the expression, by exploiting the gauss divergence theorem;

$$\int_{\Gamma} \left(\eta \rho_0 \boldsymbol{A} \nabla_x p_0 - \eta \rho_0 \boldsymbol{C} \boldsymbol{U} \right) \cdot \boldsymbol{n} d\Gamma - \int_{\Omega} \nabla_x \eta \cdot \left(\rho_0 \boldsymbol{A} \nabla_x p_0 - \rho_0 \boldsymbol{C} \boldsymbol{U} \right) d\Omega = 0, \tag{3.5}$$

which leads to the weak form of the Homogenized Reynolds Equation:

$$\int_{\Omega} \nabla_x \eta \cdot \left(\rho_0 \boldsymbol{A} \nabla_x p_0 - \rho_0 \boldsymbol{C} \boldsymbol{U} \right) d\Omega = \int_{\Gamma} \left(\eta \rho_0 \boldsymbol{A} \nabla_x p_0 - \eta \rho_0 \boldsymbol{C} \boldsymbol{U} \right) \cdot \boldsymbol{n} d\Gamma. \tag{3.6}$$

For computations, both the test function η and macroscopic pressure distribution p_0 can be assumed to have following form in the domain Ω,

$$p_0 = \sum_{I}^{N} p_I N_I \qquad \eta = \sum_{J}^{M} \eta_J M_J. \tag{3.7}$$

Here, Galerkin finite element discretization necessitates that $M = N$ and $M_I = N_I$, enabling the substitution of Eq. 3.7 in to the Eq. 3.6 to get discretized format of the Homogenized Reynolds Equation:

$$\begin{aligned} &\sum_{I} \eta_I \sum_{J} \left[\nabla_x N_I \cdot \left(\rho_0 \boldsymbol{A} \nabla_x N_J \right) \right] F_x p_J \\ &= \sum_{I} \eta_I \nabla_x N_I \left(\rho_0 \boldsymbol{A} \left(p_J \nabla_x N_J \right) - \rho_0 \boldsymbol{C} \boldsymbol{U} \right) F_x. \end{aligned} \tag{3.8}$$

Here, N_I and N_J are shape functions, with F_x denoting the integration weights calculated during computations. It should be highlighted that, all equations used during the simulations are discretized in a similar manner as shown above, as they are not to be discussed explicitly for the remainder of this work. For the case without any non-linearities, the Eq. 3.8 can be solved directly for $p_J = p_0$ with ease. Nonetheless, for a PCST fluid, a linearization has to be carried out on Eq. 3.6 for the macroscopic pressure solution p_0, which is done in the next section.

3.3 Newton-Raphson Linearization

When the fluid is Newtonian or just Shear-Thinning (ST), the Reynolds Equation can be solved directly, as there is no non-linearity associated with equations. However, when either compressibility or piezoviscosity is included, the pressure dependency of ρ density and μ viscosity requires an iterative approach for the convergence to an accurate solution.

Albeit there are multiple ways which can be utilized during this process, since a finite elements framework is used, the Reynolds Equation is linearized using **Newton-Raphson**; a previous example of its implementation for the context of homogenization of Reynolds Equation can be found in [106, 58]. The stiffness $\boldsymbol{K}$ and residual $\boldsymbol{R}$ matrices are defined for the plane slider analysis respectively as shown below:

$$\begin{aligned}
\boldsymbol{K} = \sum_I \sum_J \; & \nabla_x N_I \left[(\nabla_p \rho_0) \; \boldsymbol{A} \; (\nabla_x p_0)^T N_J \right] F_x \\
& + \nabla_x N_I \left[\rho_0 \; \boldsymbol{A} \; (\nabla_x N_J)^T \right] F_x \\
& - \nabla_x N_I \left[\nabla_p \rho_0 \; \boldsymbol{C} \; N_J \right] F_x \\
& + \nabla_x N_I \left[\rho_0 \; (\nabla_p \boldsymbol{A}) \; (\nabla_x p_0)^T \; N_J \right] F_x \\
& - \nabla_x N_I \left[\rho_0 \; (\nabla_p \boldsymbol{C}) \; N_J \; \right] F_x,
\end{aligned} \tag{3.9}$$

$$\boldsymbol{R} = \sum_I \left(-\nabla_x N_I \left[\rho_0 \; \boldsymbol{A} \; (\nabla_x p_0)^T \right] F_x + \nabla_x N_I \left[\rho_0 \; \boldsymbol{C} \right] F_x \right). \tag{3.10}$$

In the expressions provided above, N_I, N_J are shape functions from finite element discretization, and F_x are weight functions obtained for the integration as described previously. The pressure p_0 can be obtained at each iteration after assembly operation on the matrices 3.9 and 3.10 as follows:

$$\boldsymbol{K}\Delta p_0^k = \boldsymbol{R} \qquad \Delta p_0^k = \boldsymbol{K}^{-1}\boldsymbol{R} \qquad p_0^{k+1} = p_0^k + \Delta p_0. \tag{3.11}$$

The system can be solved iteratively until the convergence is reached using 3.11. For convergence, a tolerance of 10^{-9} is used with criterion of residuals of the following form:

$$\frac{||p_0^{k+1} - p_0^k||}{||p_0^{k+1}||} < 10^{-9}. \tag{3.12}$$

3.4 DNS of Navier-Stokes Equations

Even though homogenized model 3.2 itself can be validated by only using linear Reynolds equation of 3.1, since there are various new models implemented in this work concurrently using modified viscosity approach 2.5, a further validation is done using **DNS of Navier-Stokes Equations** for an incompressible fluid flow,

$$\frac{\partial \boldsymbol{u}}{\partial t} + \boldsymbol{u}\left(\nabla \cdot \boldsymbol{u}\right) = -\nabla p + \nabla \cdot \left(\mu \nabla \boldsymbol{u}\right). \tag{3.13}$$

The Navier-Stokes solutions are obtained using **OpenFoam®**, by modifying the standard incompressible solver *icoFoam* for Newtonian and Piezoviscous and Shear-thinning (PST) case. Compressibility is not incorporated into DNS framework, since the compressible solvers are proven to be quite unstable with the addition of piezoviscosity. Regardless, just PST fluid is adequate for a complete homogenization validation as the homogenized coefficients are not dependent of ρ in the first place; as it was shown in Eq. 2.66 and 2.67. The pressure result validation of homogenized LRE with DNS solutions can be found in Sec. 4.2.2. Moreover, the DNS results are used also in validating the shear stress τ in the interface walls; to ensure the framework's compatibility with texture optimization incorporating the traction reduction and amplification. These validations can be found in Sec. 4.2.3. It should be emphasized that, to the best of our knowledge, although there are numerous studies comparing Reynolds Equation pressure results to DNS [30, 12], there is not a single work directly comparing the wall shear stress, in the context of rough hydrodynamic lubrication. The DNS simulations are done for both *smooth* and *rough* interfaces; the modified icoFoam solvers for Newtonian and PST fluids can be found in the Appendix B.1 and B.2 respectively.

3.5 Texture Optimization Procedure

Texture optimization for the interface is carried out by an in-house MATLAB script utilizing the well known MMA algorithm. While the algorithm itself is used as it is, the objective functions, constraints and sensitivities of the homogenized tensors are required to be defined rigorously. The sensitivies of the homogenized tensors $\boldsymbol{A}$ and $\boldsymbol{F}$ with preliminary definitions can be found in 3.5.1, the objective functions utilized for energy dissipation minimization and maximization are presented in 3.5.2 and the design constraints imposed are given in 3.5.3. The definitions of the tensors, intermediate quantities and sensitivies follow the format provided in [49, 57], and the new geometry variable sensitivities are defined in the manner that can be found in [90].

3.5.1 Homogenized Tensor Sensitivities

For sake of simplicity, the homogenized tensors presented in Eq. 2.80 and 2.81 is written by exploiting the substituions defined below:

$$\boldsymbol{\Gamma} = \boldsymbol{I} + \nabla_y \chi_p \quad , \quad \boldsymbol{\Phi} = \left(\frac{h}{2}\right)\boldsymbol{I} + \left(\frac{h^3}{12\mu}\right)\nabla_y \chi_c = b\boldsymbol{I} + a\nabla_y \chi_c. \tag{3.14}$$

In the equation above, additional substitutions of $a = \frac{h^3}{12\mu}$ and $b = \frac{h}{2}$ is made. The substitutions shown in Eq. 3.14 is made to ensure the sensitivity expressions can be kept compact, and ease their implementation in a computational environment. The sensitivities of $\boldsymbol{A}, \boldsymbol{C}, \boldsymbol{F}$ can be separately defined as **Film Thickness Variable Sensitivity** and **Geometry Variable Sensitivity**; since the textures are obtained by allowing the alteration of the interface spatial design and the geometry of each unit cell in the domain by invoking MMA. For both sensitivity types, one may start by writing cell problems of Eq. 2.64 and 2.65 in weak form using the substitutions given above in Eq. 3.14:

$$\langle a\nabla\boldsymbol{\eta}\boldsymbol{\Gamma}^T\rangle = 0 \quad , \quad \langle\nabla\boldsymbol{\theta}\boldsymbol{\Phi}^T\rangle = 0 \tag{3.15}$$

where $\boldsymbol{\eta}$ and $\boldsymbol{\theta}$ are periodic test functions. By substituting the vector fields defined in section 2.6 as $\nabla_y\chi_p = \boldsymbol{\lambda}$ in place of test functions, one may get the following modified expressions:

$$\langle a\boldsymbol{\lambda}\boldsymbol{\Gamma}^T\rangle = 0 \quad , \quad \langle\boldsymbol{\lambda}\boldsymbol{\Phi}^T\rangle = 0. \tag{3.16}$$

One may also write down the homogenized coefficients $\boldsymbol{A}$ and $\boldsymbol{C}$ presented on Eq. 2.66 and 2.67 using the simplified notation of

$$\boldsymbol{A} = \langle a\boldsymbol{\Gamma}^T\rangle \quad , \quad \boldsymbol{C} = \boldsymbol{D}^T = \langle\boldsymbol{\Phi}^T\rangle. \tag{3.17}$$

By addition of Eq. 3.16 to Eq. 3.17, one can obtain the alternative expressions for $\boldsymbol{A}$ and $\boldsymbol{C}$:

$$\boldsymbol{A} = \langle\boldsymbol{\Gamma}a\boldsymbol{\Gamma}^T\rangle \quad , \quad \boldsymbol{C} = \boldsymbol{D}^T = \langle\boldsymbol{\Gamma}\boldsymbol{\Phi}^T\rangle \tag{3.18}$$

from which the sensitivities can be evaluated; which is done in the following sections.

3.5.1.1 Film Thickness Variable Sensitivity

Firstly starting with the analyses of film thickness, one may define the arbitrary design variable ζ as a function of microscopic length scale y, where the film thickness is $h = h(\zeta)$. By taking the derivative of the expressions given in Eq. 3.18, one may observe t hat terms involving $\frac{\partial\boldsymbol{\Gamma}}{\partial\zeta}$ are equivalent to Eq. 3.16; leading to the following expressions,

$$\frac{\partial \boldsymbol{A}}{\partial \zeta} = \left\langle \boldsymbol{\Gamma} \frac{\partial a}{\partial \zeta} \boldsymbol{\Gamma} \right\rangle \quad , \quad \frac{\partial \boldsymbol{C}}{\partial \zeta} = \left\langle \boldsymbol{\Gamma} \left(\frac{\partial b}{\partial \zeta} \boldsymbol{I} + \frac{\partial a}{\partial \zeta} \boldsymbol{\Lambda}^T \right) \right\rangle \tag{3.19}$$

where, $\boldsymbol{\Lambda} = \nabla_y \chi_c$. For stress factor tensors $\boldsymbol{D}$ and $\boldsymbol{F}$ defined in section 2.7, the sensitivity expressions can be written as

$$\frac{\partial \boldsymbol{F}}{\partial \zeta} = \left\langle \frac{\partial e}{\partial \zeta} \boldsymbol{I} - \frac{\partial b}{\partial \zeta} \left(\Lambda + \Lambda^T \right) - \frac{\partial a}{\partial \zeta} \boldsymbol{\Lambda} \boldsymbol{\Lambda}^T \right\rangle \quad , \quad \frac{\partial \boldsymbol{D}}{\partial \zeta} = \left(\frac{\partial \boldsymbol{C}}{\partial \zeta} \right)^T \tag{3.20}$$

where $e = \frac{\mu}{h}$. It can be observed from Eqs. 3.19 and 3.20 that all sensitivities shown, only include derivatives with respect to the coefficients a, b and e, which makes the computation slightly straightforward.

3.5.1.2 Geometry Variable Sensitivity

In addition to optimizing the topology by changing the film thickness, the unit cell geometry is also being modified to allow for the creation of better performing textures. The geometry of the unit cell is changed by the application of a linear transformation $\boldsymbol{y} = \boldsymbol{P}\boldsymbol{y_0}$. The design variable of $\boldsymbol{P}$ is signified by the γ. The integration notation of the following form on any arbitary quantity $\mathcal{F}$ is used to indicate

$$\langle \mathcal{F} \rangle_o = |\mathcal{Y}_o|^{-1} \int_{\mathcal{Y}_o} \mathcal{F} dv_o. \tag{3.21}$$

Having defined the fundamental notation, the sensitivities can be derived starting with $\boldsymbol{A}$,

$$\frac{\partial \boldsymbol{A}}{\partial \gamma} = \frac{\partial}{\partial \gamma} \left\langle \boldsymbol{\Gamma} a \boldsymbol{\Gamma}^T \right\rangle_o = \left\langle \frac{\partial \boldsymbol{\lambda}}{\partial \gamma} a \boldsymbol{\Gamma} \right\rangle_o + \left\langle \boldsymbol{\Gamma} a \frac{\partial \boldsymbol{\lambda}}{\partial \gamma} \right\rangle_o \tag{3.22}$$

further definitions are made $\nabla_o = \frac{\partial}{\partial \boldsymbol{y}_o}$ and $\boldsymbol{M} = \boldsymbol{P}^{-1}$ so that

$$\boldsymbol{\mathcal{X}} = \nabla_o \chi_p \quad , \quad \boldsymbol{\lambda} = \boldsymbol{\mathcal{X}} \boldsymbol{M}. \tag{3.23}$$

The new definitions are used to rewrite the terms in Eq. 3.22. using the new definition, the first term shown in Eq. 3.22 takes the form of

$$\left\langle \frac{\partial \mathbf{\Gamma}}{\partial \gamma} a \mathbf{\Gamma} \right\rangle_o = \left\langle \frac{\partial \boldsymbol{\mathcal{X}}}{\partial \gamma} \boldsymbol{M} a \mathbf{\Gamma}^T \right\rangle + \left\langle \boldsymbol{\mathcal{X}} \frac{\partial \boldsymbol{M}}{\partial \gamma} a \mathbf{\Gamma}^T \right\rangle \tag{3.24}$$

where the first term vanishes due to Eq. 3.16. Subsequently, applying a similar procedure to second term with the addition of

$$\boldsymbol{E} = \frac{\partial \boldsymbol{P}}{\partial \gamma} \boldsymbol{M} \quad , \quad \frac{\partial \boldsymbol{M}}{\partial \gamma} = -\boldsymbol{M}\boldsymbol{E}, \tag{3.25}$$

leading to the final form of the geometry sensitivity for $\boldsymbol{A}$

$$\frac{\partial \boldsymbol{A}}{\partial \gamma} = -\left\langle a \left(\boldsymbol{\lambda} \boldsymbol{E} \mathbf{\Gamma}^T + \mathbf{\Gamma} \boldsymbol{E}^T \boldsymbol{\lambda}^T \right) \right\rangle. \tag{3.26}$$

Adopting the same approach for the second cell problem solution,

$$\mathbf{\Theta} = \nabla_o \nabla_y \chi_c \quad , \quad \mathbf{\Lambda} = \mathbf{\Theta} \boldsymbol{M}, \tag{3.27}$$

which is utilized to obtain the geometry sensitivity for $\boldsymbol{C}$ in the same format as Eq. 3.26

$$\frac{\partial \boldsymbol{C}}{\partial \gamma} = -\left\langle -\boldsymbol{\lambda} \boldsymbol{E} \mathbf{\Phi}^T + \mathbf{\Gamma} a \boldsymbol{E}^T \mathbf{\Lambda}^T \right\rangle. \tag{3.28}$$

The geometry sensitivity for the tensor $\boldsymbol{D}$ is just the transpose of the Eq. 3.28 as noted previously. Lastly, by combining the previous substitutions done for $\boldsymbol{A}$ and $\boldsymbol{C}$, the final sensitivity expression is obtained for $\boldsymbol{F}$:

$$\frac{\partial \boldsymbol{F}}{\partial \gamma} = \left\langle \mathbf{\Lambda} \boldsymbol{E} \mathbf{\Phi}^T \right\rangle + \left\langle \mathbf{\Phi} \boldsymbol{E}^T \mathbf{\Lambda}^T \right\rangle. \tag{3.29}$$

Thus, the geometry sensitivity expressions in their final form only require the derivative of the linear transformation with respect to γ $\frac{\partial \boldsymbol{P}}{\partial \gamma}$, which eases the computation process. It should also be noted that, since the homogenized problem analyses is also based on the same finite elements framework, the variational basis utilized in discretization is exactly the same in pressure solutions and sensitivity calculations; ensuring that framework works in successful conjunction even in coarse resolutions.

3.5.2 Objective Functions

Prior to definition of optimization objective function, how the film thickness is varied should be described. Since the textures are imposed on possible bearing geometries such as plane slider or a squeeze film, the maximum and minimum height of the textures should be adjusted accordingly to the smooth film thickness h_0. The film thickness variation can be expressed in the following fashion

$$\bar{h} = \bar{h}_{min} + \left(\bar{h}_{max} - \bar{h}_{min}\right) \rho \tag{3.30}$$

where $\rho \in [0, 1]$ is a filtered variable that determines the roughness distribution. $\bar{h}_{max}$ is designated to be $0.8h_0$ of the mean film thickness, to avoid collision between walls of the interface whilst allowing a broad band for possible textures, by a tolerance in following manner

$$\bar{h}_{max} = 0.8h_0 \quad , \quad \bar{h}_{min} = -\bar{h}_{max}. \tag{3.31}$$

While the tolerance of 0.8 can be increased further to facilitate better MMA performance, the numerical instabilities may emerge during the computation of pressure and performance variables, specifically when piezoviscosity is included. The total film thickness with texture h is then expressed as follows with a visual guide on

$$h = h_0 - \bar{h}. \tag{3.32}$$

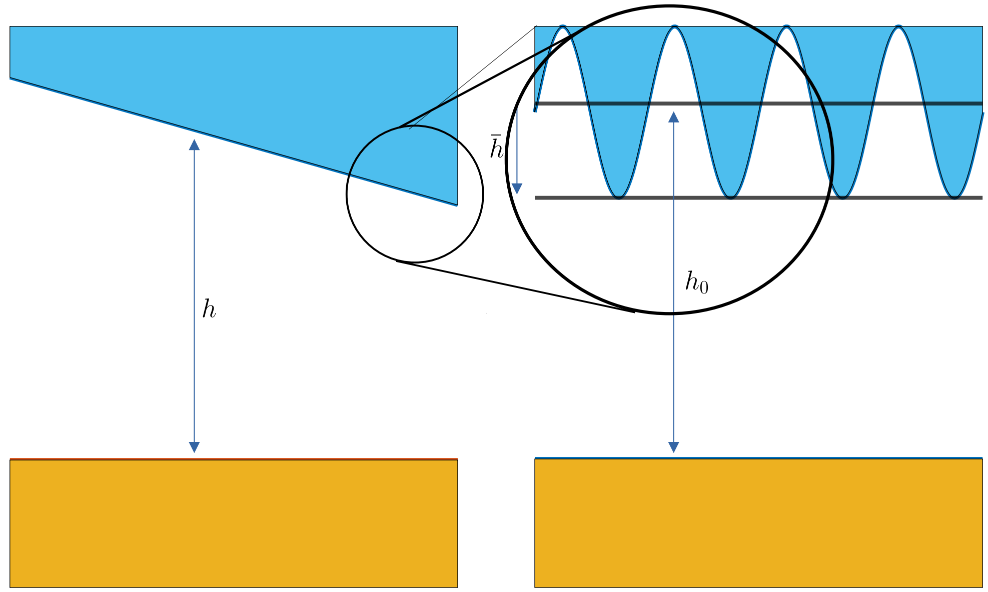

Figure 3.2: Left handside shows the homogeneous illustration, while righthandside indicates the zoomed in view to showcase heterogenuity of the optimization domain.

There are two objective functions implemented within scope of this work, both of which are of same nature; with one being dependent time other not. The energy dissipation expression defined in the Eq. 2.82 is utilized as the objective function for the plane slider profile:

$$f_0 = \kappa_1 \left(\nabla_x p_0 \cdot \boldsymbol{A} \nabla_x p_0 + \boldsymbol{U} \cdot \boldsymbol{F} \boldsymbol{U} \right) + \kappa_2. \tag{3.33}$$

Here, κ_1 non-zero scaling factor used to change between f_0 maximization and minimization depending on the sign, whereas κ_2 is a scaling constant used so that the objective function is bounded within the limits defined by MMA. For a squeeze film however, as the magnitude of p_0 and $\boldsymbol{\nabla p_0}$ is changing alongside the mean film thickness h_0, a time averaging is done over a cycle of contraction and expansion to get the optimal surface,

$$f_0 = \frac{\kappa_1}{\mathcal{T}} \int_t \left(\nabla_x p_0 \cdot \boldsymbol{A} \nabla_x p_0 + \boldsymbol{U} \cdot \boldsymbol{F} \boldsymbol{U} \right) dt + \kappa_2. \tag{3.34}$$

3.5.3 Constraints

The optimization is carried out by enforcing two constraints on the process. Similar to sensitivity, they are called space and geometry constraints. The space constraint is quite important for the application as it ensures that the pre-defined $\bar{h}$ profile of Eq. 3.35 average is preserved in the final texture:

$$\langle \bar{h} \rangle^2 = 0. \tag{3.35}$$

Whereas the geometry constraint ensures that the size of the unit cell optimized is bounded by

$$(\det(\boldsymbol{P}) - 1)^2 = 0. \tag{3.36}$$

It should be highlighted that this constraint itself does not have an impact on homogenization results, as the absolute size of the unit cell is not relevant.

Chapter 4

Results and Discussion

4.1 Geometry of the Interface and Assumptions

For hydrodynamic contacts, many different geometries can be assumed, for different system response. However, since the scope of this research aims to attain optimal system response by application of a generated micro-texture through homogenization, simple geometries can be used during the validation process. Therefore, only two geometries are implemented in this work: a **plane slider** and **parabolic slider**. It should be indicated that, for DNS comparison with Reynolds equation solutions, only plane slider has been implemented to prevent possible numerical unstability problems related to parabolic slider.

One may find the utilized geometries in the figure shown below. For DNS validation, solutions are post-processed on the red line in the mid-section of the channel throughout the streamwise direction, which are shown in the Figs. 4.1 and 4.2.

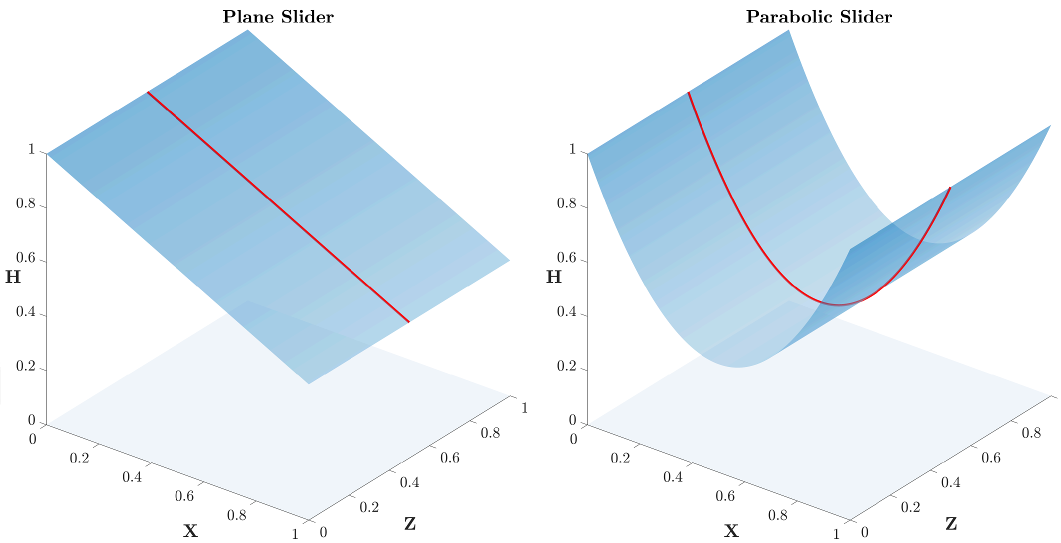

Figure 4.1: Smooth Plane Slider and Parabolic Slider Domain View. Red lines indicate the place where solutions are evaluated.

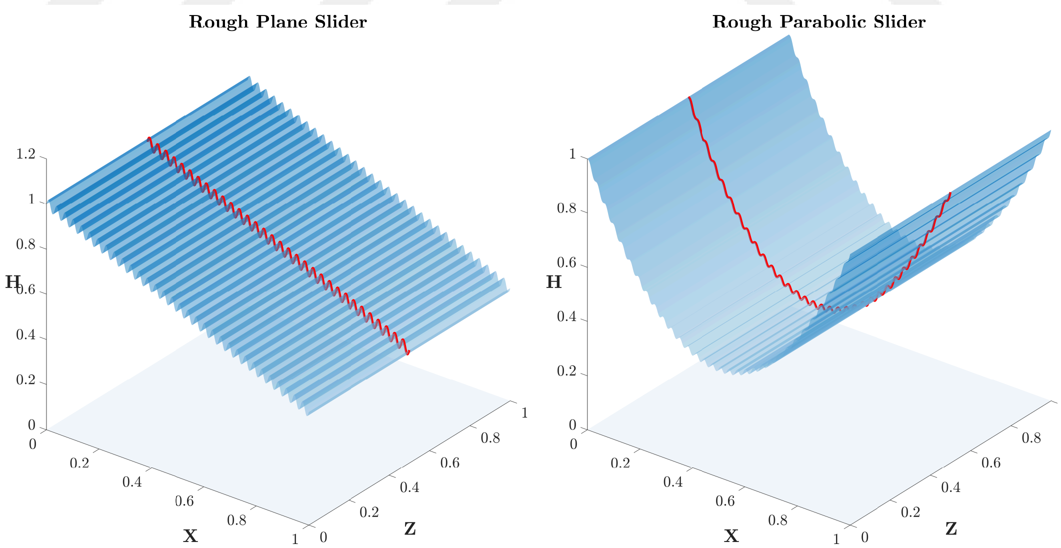

Figure 4.2: Sinusoidal Roughness applied Plane Slider and Parabolic Slider Domain View. Red lines indicate the place where solutions are evaluated.

4.2 Model Validation

4.2.1 Homogenization Method Validation

The homogenization method is expected to be the same as linear Reynolds equation when the roughness frequency $\omega \longrightarrow \infty$ is sufficiently large. It has been found from the simulations that, starting at $\omega = 128$, the homogenized Reynolds matches quite well to the direct solution of linear Reynolds for an interface with periodic roughness.

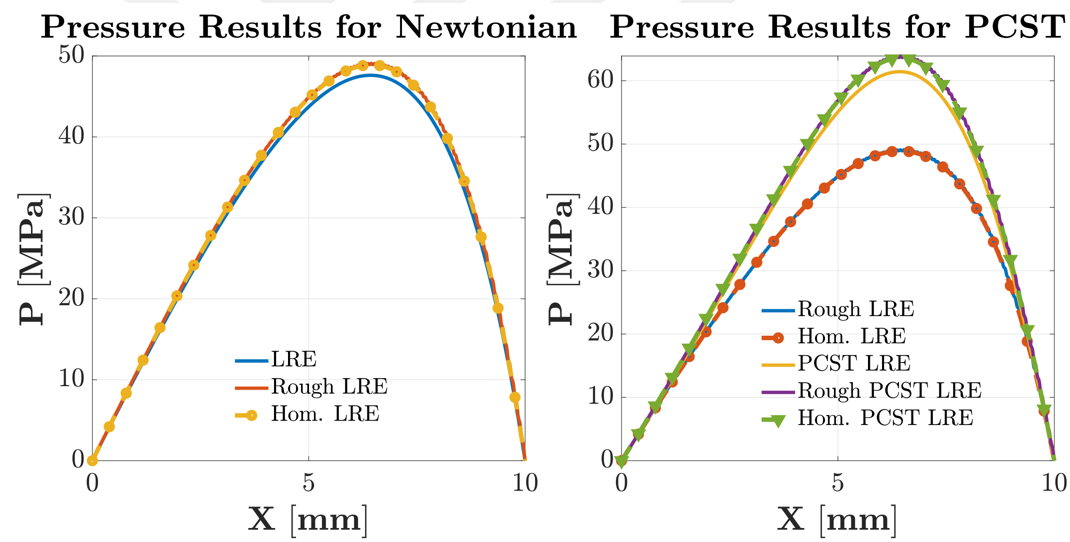

Figure 4.3: Plane Slider Results obtained from Reynolds equation solutions. **RE** stands for simple linear Reynolds Equation solution, **PCST** for the case with piezoviscous, shear-thinning and compressibility fluid, **Rough** stands for linear Reynolds solutions obtained for a sinusoidal roughness applied interface; and **Hom.** stands for rough solutions obtained from Homogenized Reynolds Equation at $\omega = 128$.

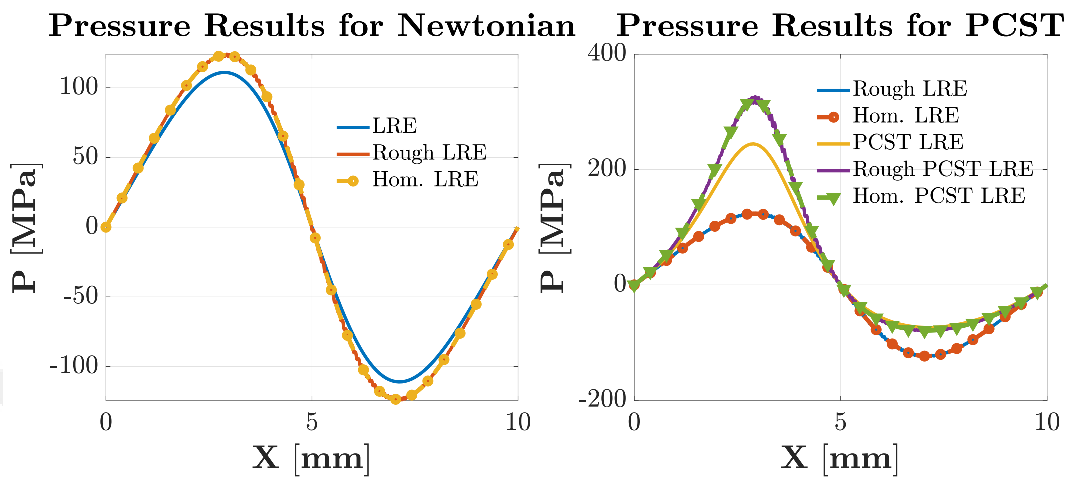

Figure 4.4: Parabolic Slider Results obtained from Reynolds equation solutions. **RE** stands for simple linear Reynolds Equation solution, **PCST** for the case with piezoviscous, shear-thinning and compressibility fluid, **Rough** stands for linear Reynolds solutions obtained for a sinusoidal roughness applied interface; and **Hom.** stands for rough solutions obtained from Homogenized Reynolds Equation at $\omega = 128$.

2D solutions were also obtained for the plane slider profile shown in Fig. 4.1 to be used on optimization scheme. 2D solutions are also obtained for PST, ST and PZ fluids also to observe the possible changes in the optimization behaviour due to drastic changes in the pressure profile. Solutions are obtained in 2D case by non-dimensionalizing it, to increase the numerical efficiency of the system as the numbers in dimensional form are quite low in magnitude ($\approx 10^{-18}$). The non-dimensionalization is done as follows:

$$\begin{aligned} x^* &= \frac{x}{L} & y^* &= \frac{y}{h_0} & z^* &= \frac{z}{L} & h^* &= \frac{h}{h_0} \\ \rho^* &= \frac{\rho}{\rho_0} & \eta^* &= \frac{\eta}{\eta_0} & U_1^* &= \frac{U_1}{U_{ref}} \\ U_2^* &= \frac{U_2}{U_{ref}} & p^* &= \frac{p}{p_0} & \Lambda^* &= \frac{\eta_0 U_{ref} L}{h_0^2 p_0} \end{aligned} \tag{4.1}$$

Above, Λ^* is the **Bearing Number**. An exemplary 2D solution comparing Newtonian and PCST fluid flow results can be found below:

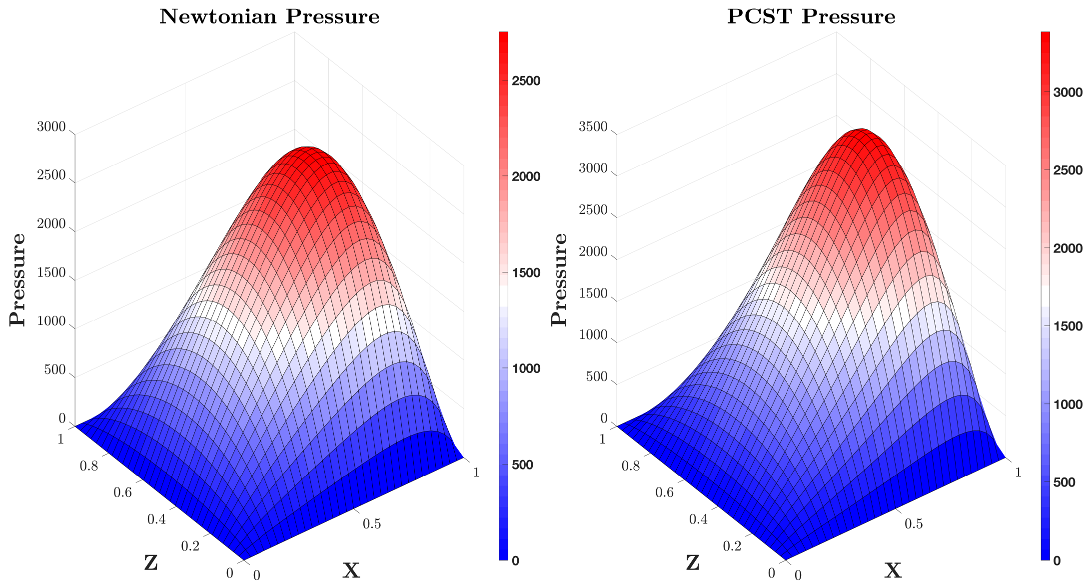

Figure 4.5: Smooth Plane Slider Pressure solutions in non-dimensional form for Newtonian and PCST fluid flow case.

Different cases accounting for distinct fluid effect combinations of those discussed in Secs. 2.2, 2.3 and 2.4 to acquire different cases that can enable better optimization results were computed. Quadratic convergence behaviour with Newton-Raphson for PCST case can also be shown in logarithmic scale with the residuals defined in Eq. 3.10:

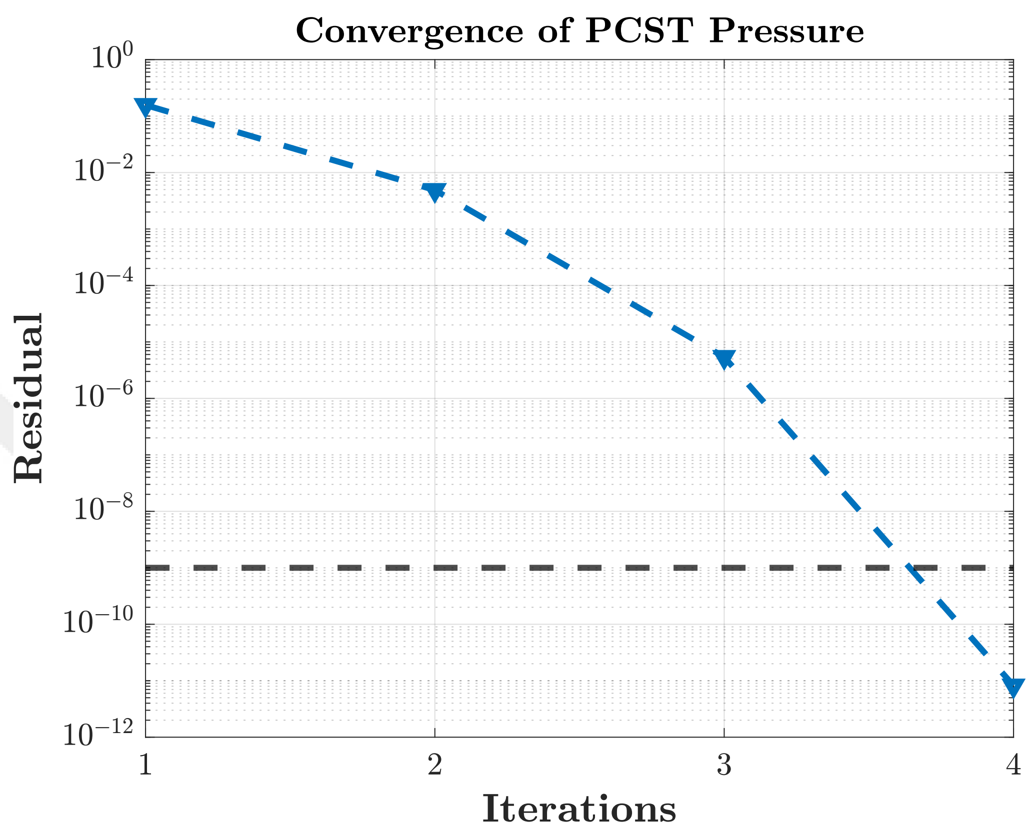

Figure 4.6: 2D Plane Slider Pressure Convergence results for a PCST fluid with Newton-Raphson with tolerance 10^{-9}.

As it was discussed previously, these fluid effects are used to amplify the performance of optimization algorithm and to observe possible distinctions amongst the obtained micro textures.

4.2.2 LRE and homogenized LRE Validation with DNS

The Navier-Stokes solutions were obtained for different a of roughness and ω frequency for a sinusoidal periodic roughness applied geometry of $h = h_0 + a \sin(\omega x/L)$ for the sake of completeness.

The frequency is increased starting from $\omega = 4$ up until $\omega = 128$; in which case homogenization regime holds well with linear Reynolds. The amplitude is increased starting from $a = 0.1$ μm until the $a = 0.5$ μm. While it should be possible to increase these values further, the increase in computational cost to resolve the roughness and instability issues related to refinement in rough geometry made this process obsolete.

There are several things that is to be observed on Navier-Stokes comparison, which are listed as follows below:

- Regardless of the frequency ω and a, the linear Reynolds Equation (LRE) solutions should agree with DNS.
- At frequency $\omega = 64$ and $\omega = 128$ the homogenized Reynolds should be able to match both DNS and LRE.
- PST fluid in combination with increased roughness amplitude a should lead to a substantial amplification in pressure magnitude.

To highlight the prediction in the last point above, a series of DNS solutions for smooth and rough Newtonian and PST case with amplitude of $a = 0.5$ μm can be found below in Fig. 4.7:

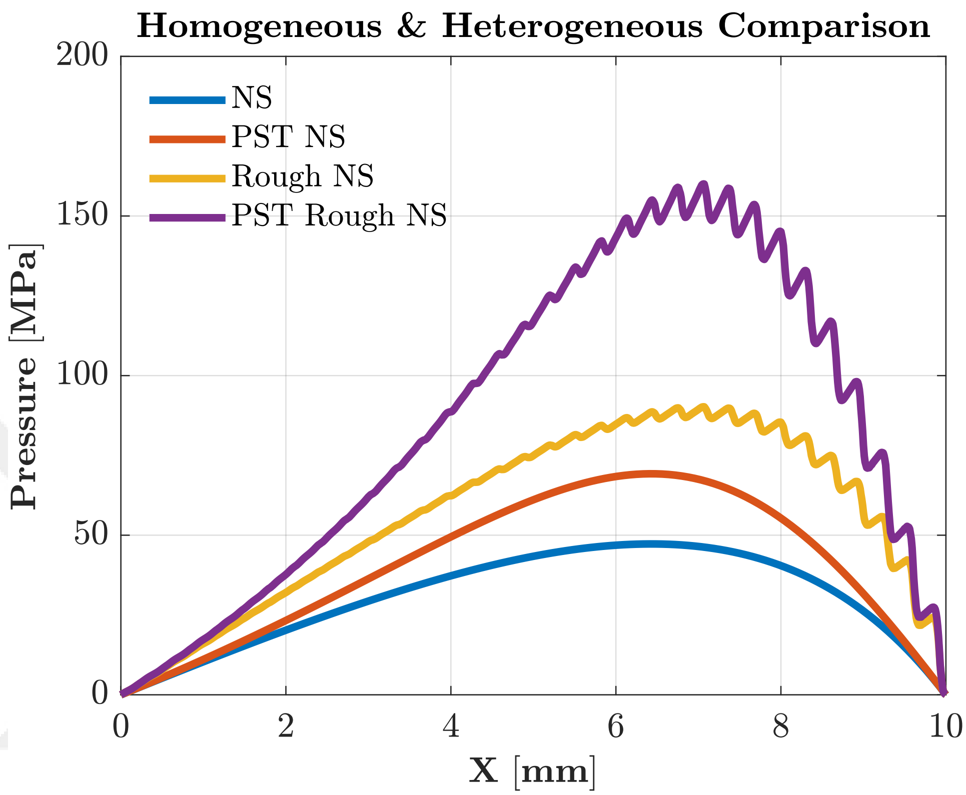

Figure 4.7: Plane Slider pressure results at the midline of the domain through streamwise direction for Newtonian and PST case both at smooth surface and rough texture with amplitude $a = 0.5$ μm and frequency $\omega = 32$.

The roughness amplitude drastically impacts the overall pressure magnitude amplification caused by the piezoviscosity. This also leads to increased chance of numerical instabilities in DNS.

To check whether linear Reynolds solution for heterogeneous profiles match regardless of the case, a test case was created with different amplitudes at the roughness frequency of $\omega = 32$, which can be found in the Fig. 4.8 The results are obtained for different roughness frequencies ω and amplitude a up until the point the numerical cost of DNS becomes computationally expensive. However, this is not an issue, as around $\omega = 128$, the Homogenized Reynolds predictions match completely with Navier-Stokes. This can be observed in the Fig. 4.9 shows the results at $a = 0.1$ μm.

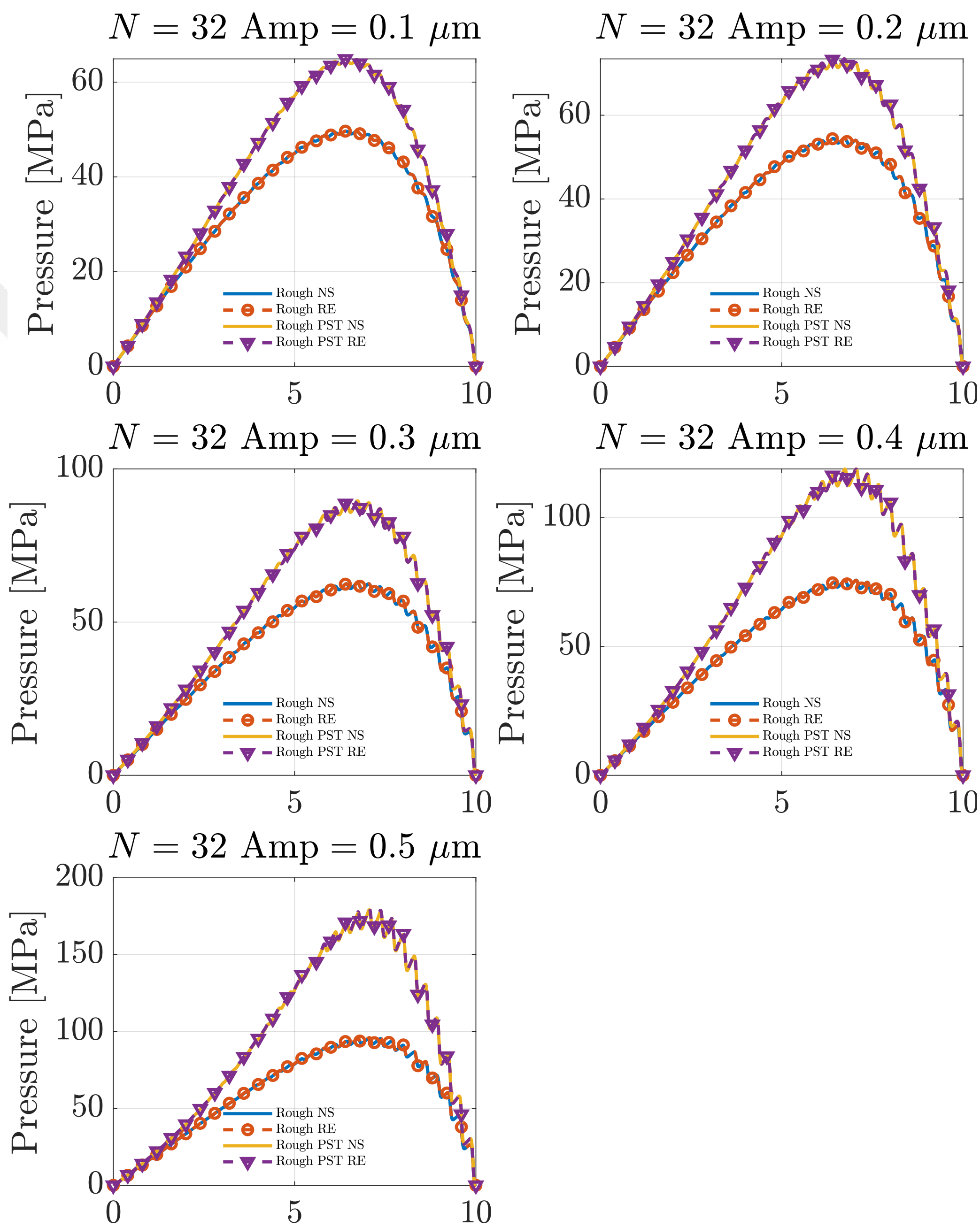

Figure 4.8: Plane Slider Pressure Results Comparison between LRE and Navier-Stokes for different roughness amplitudes of a sinusoidal height profile at frequency of $\omega = 32$.

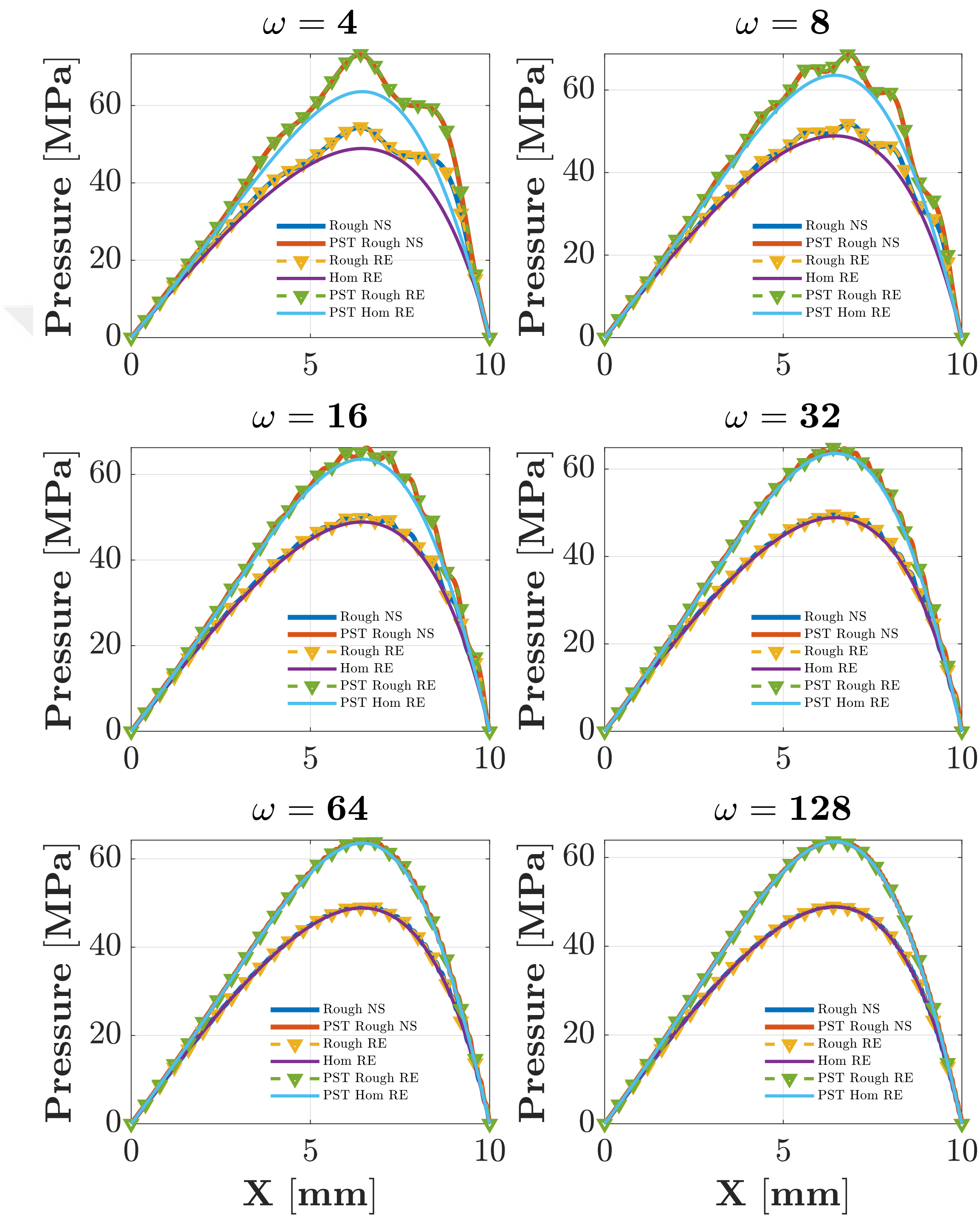

Figure 4.9: Plane Slider Pressure Results Comparison between LRE, Hom. RE and Navier-Stokes for different roughness frequencies of a sinusoidal height profile at amplitude of 0.1 μm.

4.2.3 Traction Validation with Navier-Stokes

While the homogenization framework is thoroughly validated for the pressure solutions, since this numerical framework is also utilized for optimization of the hydrodynamic contacts for possible energy dissipation or friction maximization and minimization, the relevant quantity of shear-stress in either top or lower wall of the interface is also compared to DNS solutions for the sake of completeness.

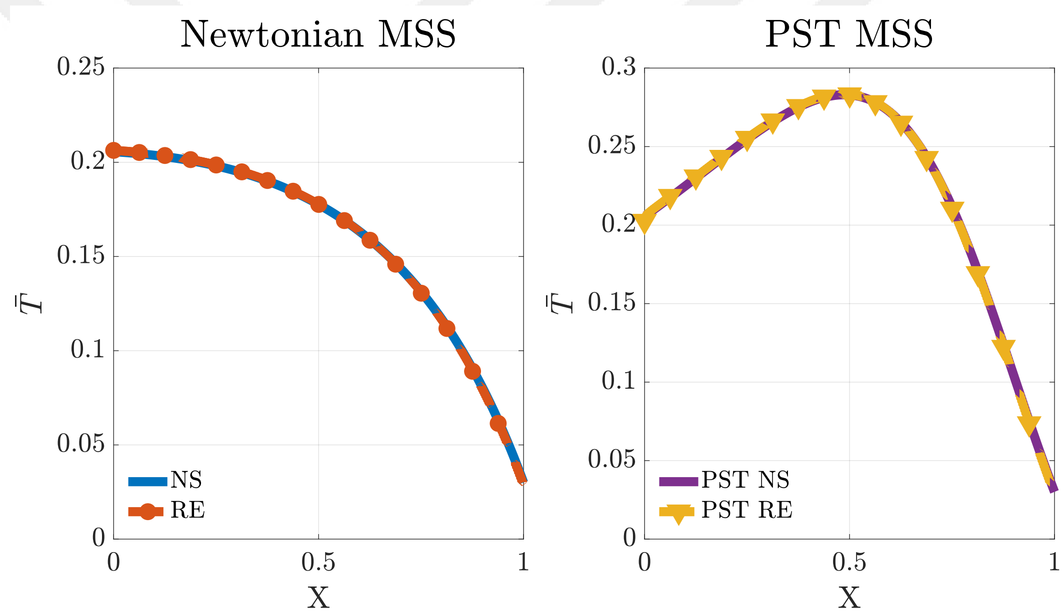

Figure 4.10: Plane Slider shear stress τ at moving smooth wall (MSS) obtained for homogeneous case from Reynolds Equation and Navier-Stokes Equations for Newtonian and Piezoviscous, Shear-Thinning (PST) fluid flows.

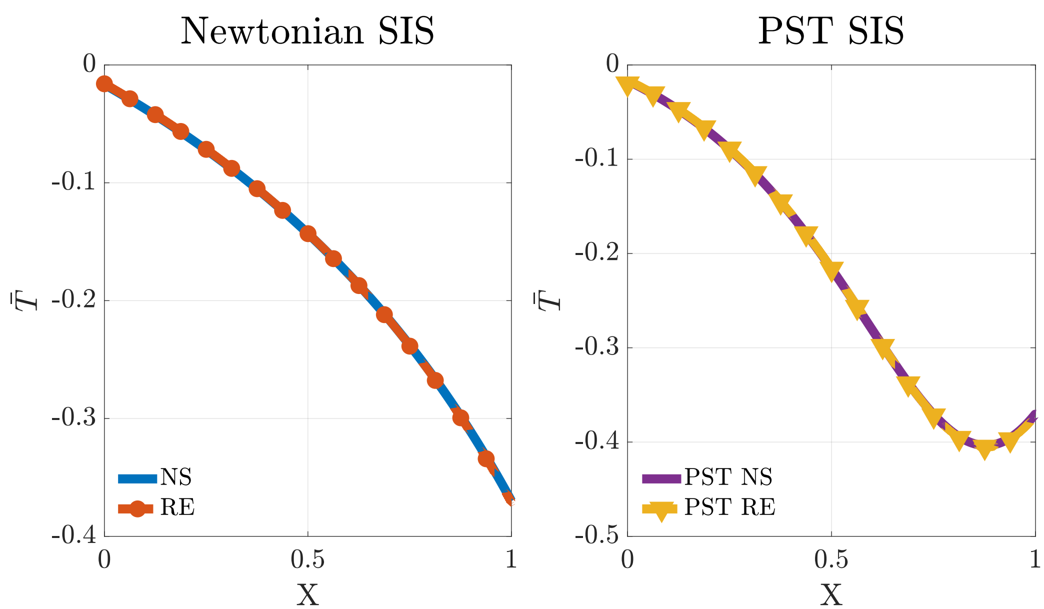

Figure 4.11: Plane Slider shear stress τ at inclined stationary wall (SIS) obtained for homogeneous case from Reynolds Equation and Navier-Stokes Equations for Newtonian and Piezoviscous, Shear-Thinning (PST) fluid flows.

Consequently, as the homogenization is a key aspect of texture optimization, the above validation for smooth surfaces illustrated on Figs. 4.10 and 4.11 should also be done for surfaces with a periodic roughness on them. The LRE traction results and Homogenized LRE traction results are once again compared to DNS solutions for different frequencies in the figures shown below. For $\omega = 4$, the DNS results are only compared with LRE, as the homogenization is not applicable for low frequency. However, it can be observed in Figs. 4.12, 4.13 and 4.15 that the LRE and DNS is in a complete agreement. Nonetheless, since homogenized LRE is utilized to gain a computational advantage in pressure solutions and texture optimization, it was also fared against DNS solutions in Figs. 4.14 and 4.16.

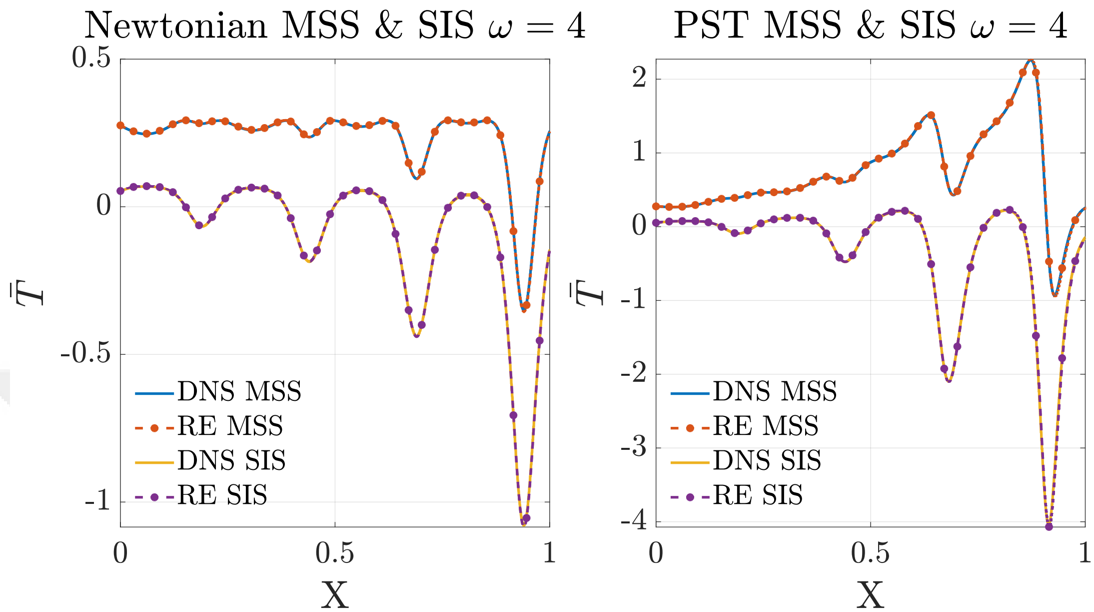

Figure 4.12: Plane Slider shear stress τ comparison between DNS and LRE for MSS and SIS for rough stationary upper surface with $\omega = 4$ and $a = 0.5\mu$m.

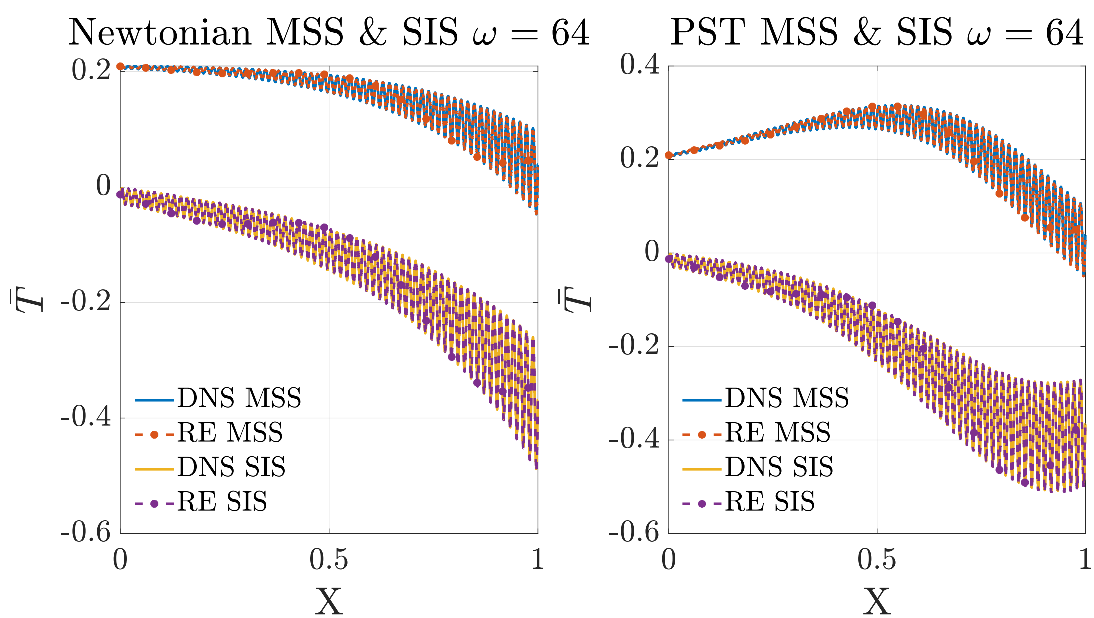

Figure 4.13: Plane Slider shear stress τ comparison between DNS and LRE for MSS and SIS for rough stationary upper surface with $\omega = 64$ and $a = 0.1\mu$m.

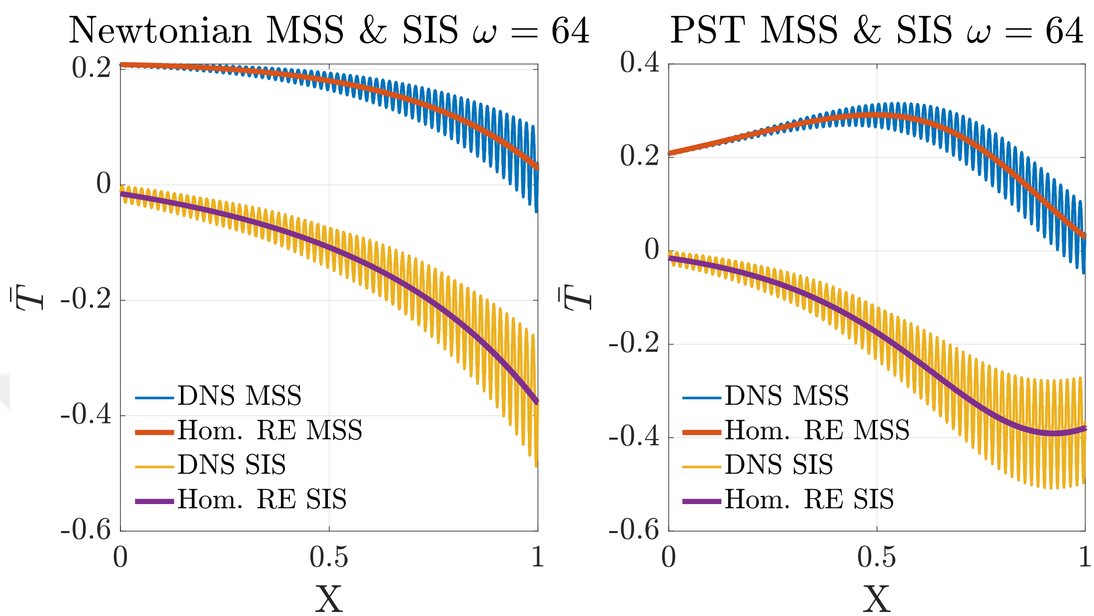

Figure 4.14: Plane Slider shear stress τ comparison between DNS and Homogenized LRE for MSS and SIS for rough stationary upper surface with $\omega = 64$ and $a = 0.1\mu$m.

The results show a great agreement for both smooth and inclined walls in both fluid flows; nevertheless, the difference in traction is caused mainly by the variable viscosity μ of the PST fluid flow. However, since the main goal is to optimize the interfaces in which there is a periodic roughness or micro-texture, this validation is ought to be carried out for a case in which a sinusoidal roughness is existent for homogenized LRE performance with respect to the DNS. Applying the same procedure to a case of Navier-Stokes solutions of with the rough profile of $a =$ 0.1 μm and frequency of $\omega = 128$, the acquired results can be found below:

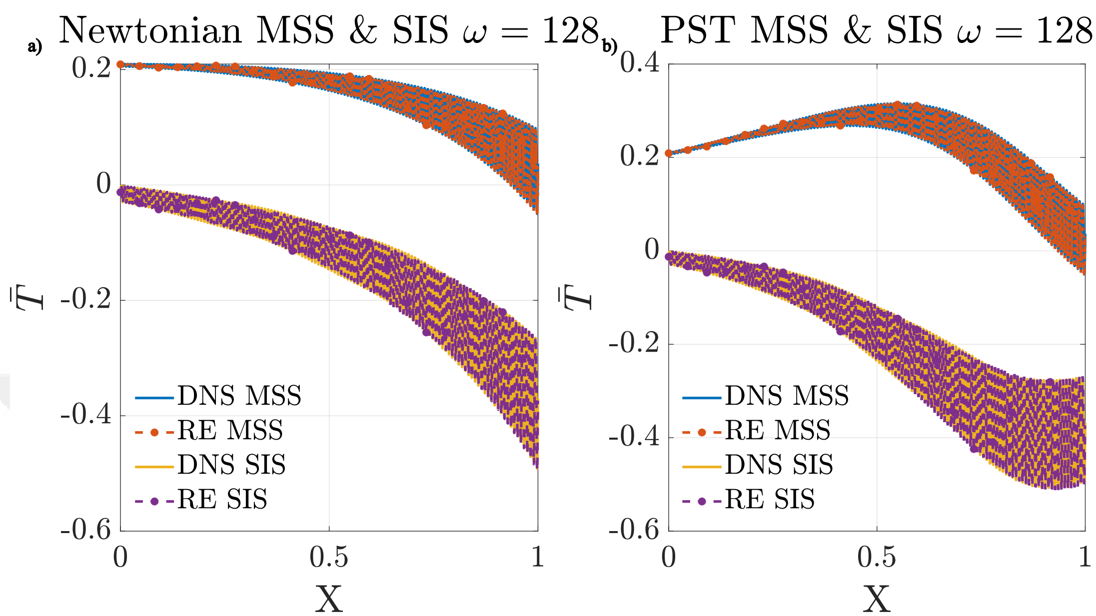

Figure 4.15: Plane Slider shear stress τ comparison between DNS and LRE for MSS and SIS for rough stationary upper surface with $\omega = 128$ and $a = 0.1\mu$m.

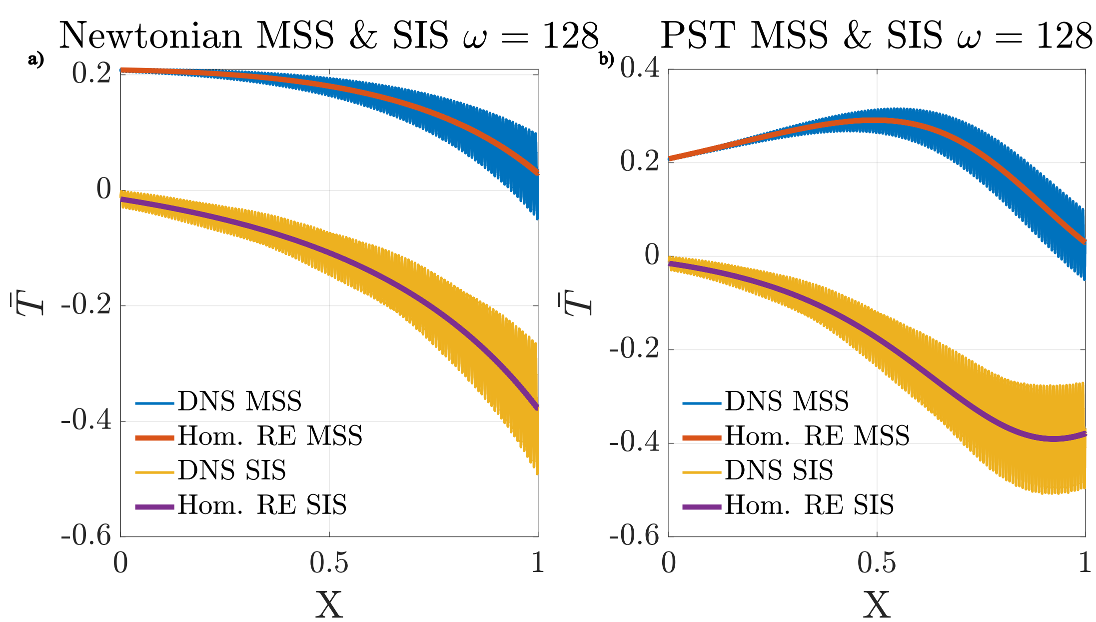

Figure 4.16: Plane Slider shear stress τ comparison between DNS and Homogenized LRE for MSS and SIS for rough stationary upper surface with $\omega = 128$ and $a = 0.1\mu$m.

It can be inferred from Fig. 4.16, the homogenized LRE traction prediction can accurately follow the real highly oscillatory traction profile; provided that the roughness frequency is adequately high. The above results are quite relevant for the ultimate goal of the project, as they demonstrate that the acquired novel computational framework is a valid approximation of DNS solutions for both pressure and traction of Newtonian and complex rheology fluids. Hence, homogenization-based framework can be utilized for the creation of textures designed to moderate energy dissipation minimization and maximization.

4.3 Energy Dissipation and Friction Minimization & Maximization with Texture Optimization

Having done all prerequisite validations both on pressure profile p and shear-stress on the interface surface τ, the texture optimization can now be used. First application is the energy dissipation minimization or maximization by inducing the equations provided in the Sec. 2.8. Dissipation maximization is the first subtitle discussed in this chapter, as it is generally much simpler than the minimization due to physical and computational constraints explained in the Sec. 2.8.

In the literature on previous applications of a micro-texture on a hydrodynamic interface, a single periodic structure is used to account for transition to the optimal response of the whole domain. This approach is shown to be fine for most practical purposes, as the system behaviour is shown to be drastically altered in a positive way. Nonetheless, since the performance parameters such ash_0, p, ∇p_0 and μ changes across the entire domain, specifically for a non-Newtonian fluids of the type shown in this work, ideally multiple textures should be applied to different parts of a domain. Therefore, in this work, the solution domain is partitioned so that, different representative optimization parameters can be input into the MMA; from which the whole domain can be solved with homogenized Reynolds equation again to observe the change in the system. While this approach would lead to a substantial increase in computational power necessity, it should also facilitate an overall increase in optimization performance as the number of partitioned sub-sectors N is incremented. One may also expect that at some certain number of sectors N, the system response would saturate, meaning it may not be amplified further than it.

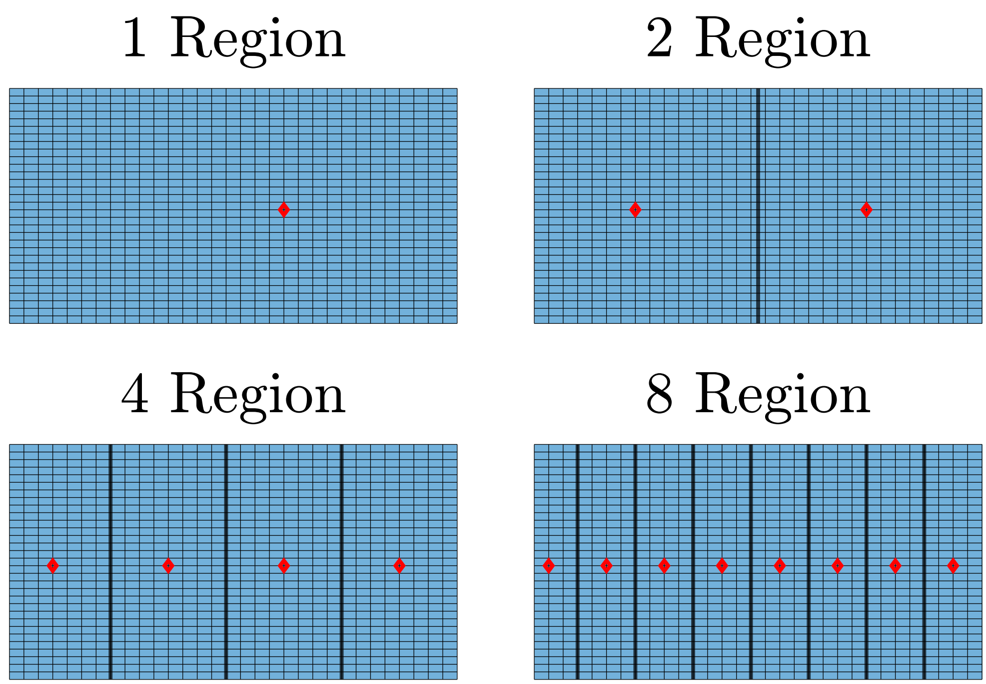

Figure 4.17: Rectangular sectoring with regions $N = 1, 2, 4, 8$. Red markers indicate the point in which ∇p_0, p_0 and h values are taken for optimization input, while the black lines indicate the region borders.

4.3.1 Energy Dissipation Maximization

The energy dissipation maximization is done on three different fluids: PCST fluid as the piezoviscosity and compressibility should significantly increase friction due to increase in ρ and μ; ST fluid as it would diminish the efficiency of the optimized texture by reducing the magnitude of the fluid viscosity; and lastly Newtonian case which would yield a standard expected behaviour. All of which are utilized to distinguish between the degree of applicability of each fluid type for different engineering purposes. For the plane slider, sub-sectors are created such that the they are propagated only on streamwise direction, as the $\boldsymbol{U}$ is non-zero and spanwise velocity component is $\boldsymbol{W} = 0$ and h is reduced in that direction, so that specimen points would have distinctive p_0, $\nabla_x p_0$ and h values for the region they are representing. One may find the sectoring demonstration on Fig. 4.17.

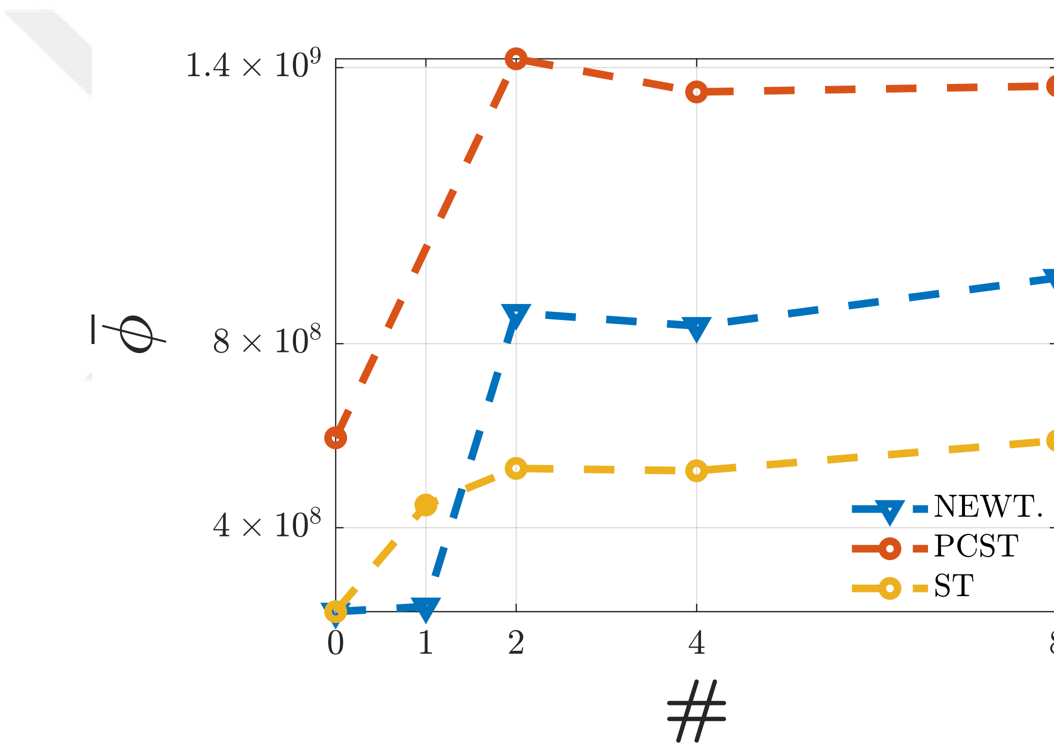

Figure 4.18: The energy dissipation ϕ maximization with MMA texture optimization of $N = 1, 2, 4, 8$ partitions on the domain for PCST (Piezoviscous, Compressible and Shear-Thinning), Newtonian and ST (Shear-Thinning) fluid types using the homogenized Reynolds Equation. 0 index stands for the smooth (homogeneous) texture.

It can be inferred from Fig. 4.18 that the intuitive guesses were correct; the PCST fluid enables a substantial amplification of the the energy dissipation significantly, due to combined effect of the increased viscosity and pressure. In addition to it, shear-thinning effect can not be observed directly, as the piezoviscosity is highly prominent. On the other hand, shear-thinning only, leads to a substantial decrease in energy dissipation maximization performance, because of the dampened viscosity and pressure.

4.3.2 Traction Maximization

Similar to the energy dissipation maximization, as the traction $\bar{T}$ is a quantity directly related to the energy dissipation, the expectancy is that a PCST fluid should lead to the best maximization trend. The Fig. 4.19 approves of this expectancy, since increases in friction and pressure contribution due to piezo-viscosity and compressibility are directly impactful on the energy dissipation; therefore, leading to a nearly exact trend of maximization with respect to the number of sectors #.

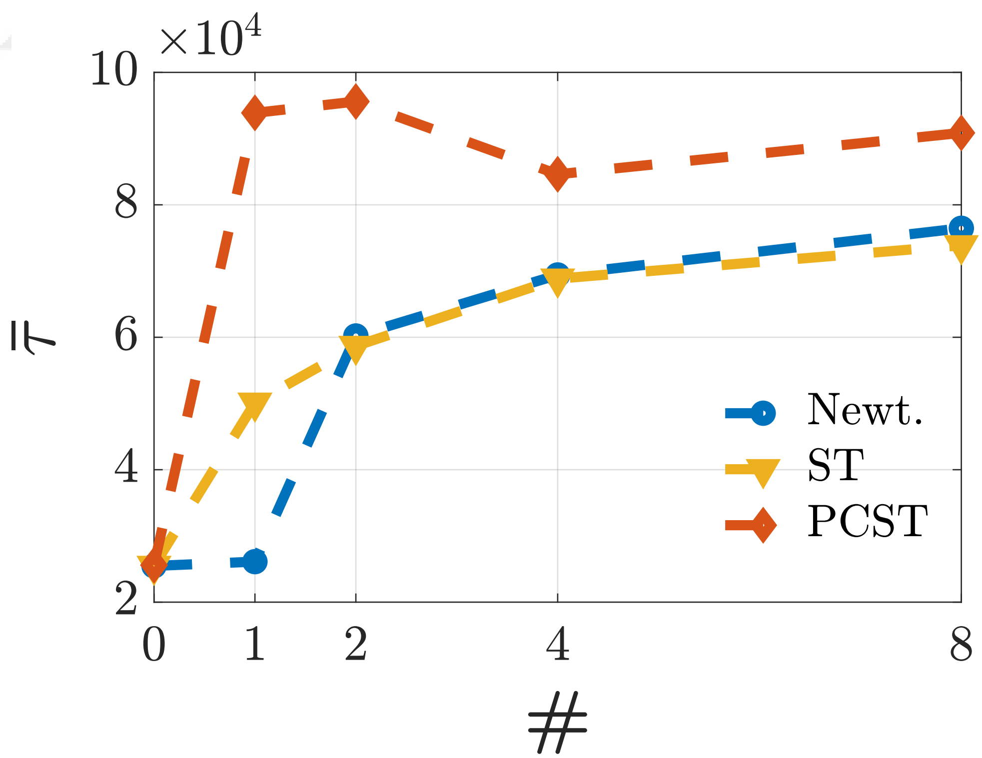

Figure 4.19: The traction τ maximization with MMA texture optimization of $N = 1, 2, 4, 8$ partitions on the domain for PCST (Piezoviscous, Compressible and Shear-Thinning), Newtonian and ST (Shear-Thinning) fluid types using the homogenized Reynolds Equation. 0 index stands for the smooth (homogeneous) texture.

4.3.3 Energy Dissipation Minimization

The dissipation minimization cannot be done in a thorough manner by applying a suitable micro texture because of the issue related to inevitable maximization of ϕ_F due to application of any structure to the interface surface, as explained in Sec. 2.8, for the **sliding** profiles where $\boldsymbol{U} \neq 0$. Therefore, the energy dissipation minimization is done using a **squeeze film** where the Couette term can vanish entirely. Therefore a squeeze film setup is created, using the same procedure described in this work for a series of timesteps.
It should be emphasized that, in the current squeeze film setup, an additional non-linearity related to pressure gradient $\nabla_x p_0$ dependence of strain rate through the expressions Eqs. 2.19a and 2.19a appears. To handle this obstacle in the macroscopic solution, a new Newton-Raphson linearization has to be carried out, which is done down below from Eqs. 4.2 to 4.4. However, the homogenization that was carried out in Sec. 2.6, was not carried out accounting for this new dependency on $\nabla_x p_0$, hence, the current homogenized tensors, may not be able to reflect the shear-thinning physics in a complete manner for a squeeze film. Therefore, the validity of the current setup is checked, just after the derivation on Newton-Raphson is done down below, in a heuristic approach, to validate whether that the current homogenized model is still able to predict the direct LRE solutions for a non-Newtonian squeeze film setup or not. Moreover, the devised case should not only enable accurate homogenized solutions, the new rough and smooth results should have a relevant difference between them.

The results are obtained by additional linearization of homogenized tensor $\boldsymbol{A}$ with respect to $\nabla_{\boldsymbol{x}} p_0 = \boldsymbol{G} = \frac{\partial p_0}{\partial x}\hat{i} + \frac{\partial p_0}{\partial z}\hat{k}$, by exploiting chain rule,

$$\frac{\partial \boldsymbol{A}}{\partial \boldsymbol{G}} = \frac{\partial \boldsymbol{A}}{\partial \mu}\frac{\partial \mu}{\partial \dot{\gamma}}\frac{\partial \dot{\gamma}}{\partial \boldsymbol{G}}, \tag{4.2}$$

which results in a new Newton-Raphson Scheme, and new stiffness and residual matrices $\boldsymbol{K}$ and $\boldsymbol{R}$, devised in a similar fashion to one in Sec. 3.3; specifically for a squeeze film macroscopic pressure solution with a PCST lubricant:

$$
\begin{aligned}
\boldsymbol{K} = \sum_I \sum_J \; & \nabla_x N_I \left[(\nabla_p \rho_0) \; \boldsymbol{A} \; (\nabla_x p_0)^T N_J \right] F_x \\
& + \nabla_x N_I \left[\rho_0 \; \boldsymbol{A} \; (\nabla_x N_J)^T \right] F_x \\
& - \nabla_x N_I \left[\nabla_p \rho_0 \; \boldsymbol{C} \; N_J \right] F_x \\
& + \nabla_x N_I \left[\rho_0 \; (\nabla_{\boldsymbol{G}} \boldsymbol{A}) \; (\nabla_x p_0)^T \; (\nabla_x N_J)^T \right] F_x \\
& + \nabla_x N_I \left[\rho_0 \; (\nabla_p \boldsymbol{A}) \; (\nabla_x p_0)^T \; N_J \right] F_x \\
& - \nabla_x N_I \left[\rho_0 \; (\nabla_p \boldsymbol{C}) \; N_J \; \right] F_x ,
\end{aligned}
\tag{4.3}
$$

$$
\boldsymbol{R} = \sum_I \left(- \nabla_x N_I \left[\rho_0 \; \boldsymbol{A} \; (\nabla_x p_0)^T \right] F_x + \nabla_x N_I \left[\rho_0 \; \boldsymbol{C} \right] F_x - N_I \dot{h}_0 F_x \right) . \tag{4.4}
$$

Here, $\dot{h}_0$ indicates the derivative of mean film thickness h_0 with respect to time t. The comparison between the pressure distributions of PCST, ST and Newtonian fluid flows can be found illustrated on Fig. 4.20; alongside the Heterogeneous and Homogenized comparison on Fig. 4.21 down below. Moreover, an exemplary 2D PCST pressure distributions over time used in the optimization scheme explained in the Sec. 3.5 can be found in the Fig. 4.22.

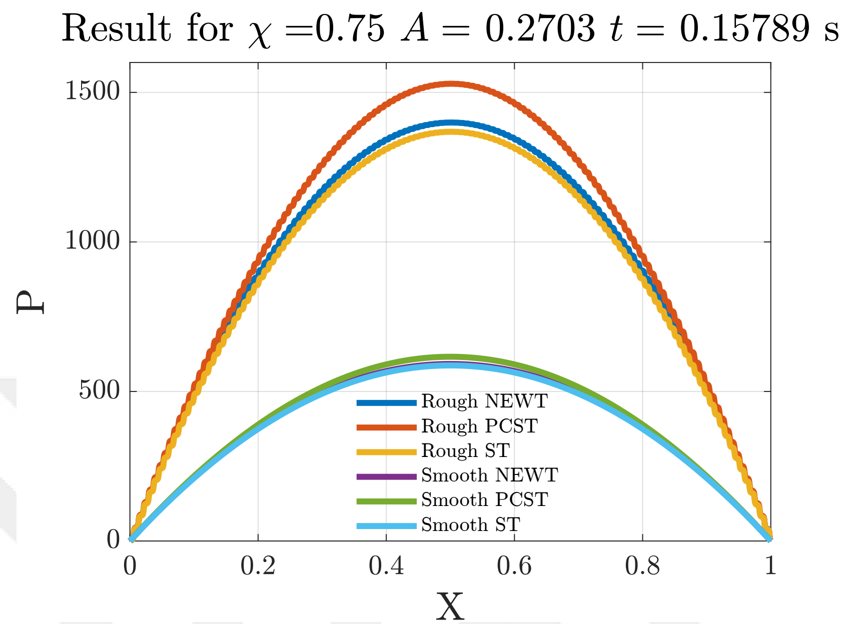

Figure 4.20: 1D LRE Results for the comparison of PCST, ST and Newtonian fluids for Heterogeneous and Homogeneous Reynolds Equation, using new Newton-Raphson Scheme for $\nabla_x p_0$ at $\omega = 128$. $y/h = \chi = 0.75$ and $A = 0.20$.

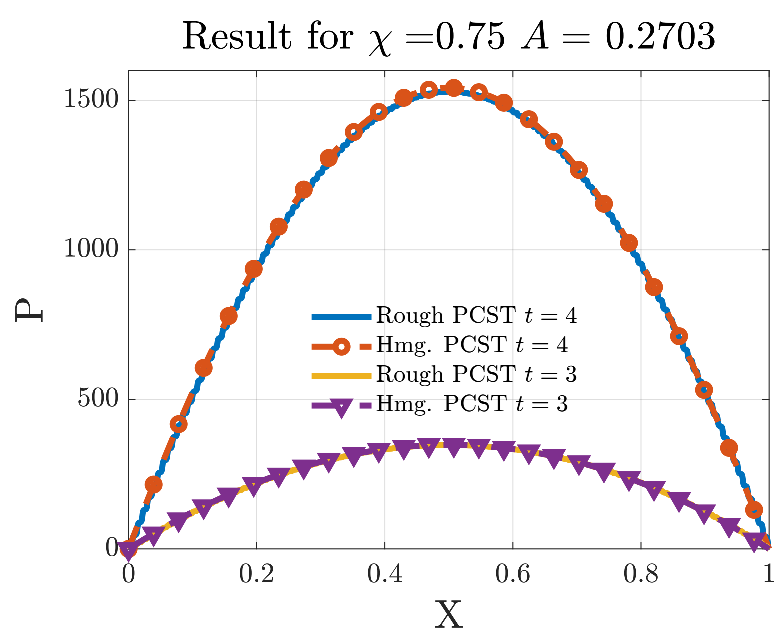

Figure 4.21: 1D PCST Results for the comparison of Heterogeneous and Homogenized Reynolds Equation, using new Newton-Raphson Scheme for $\nabla_x p_0$ at $\omega = 128$. $y/h = \chi = 0.75$ and $A = 0.20$.

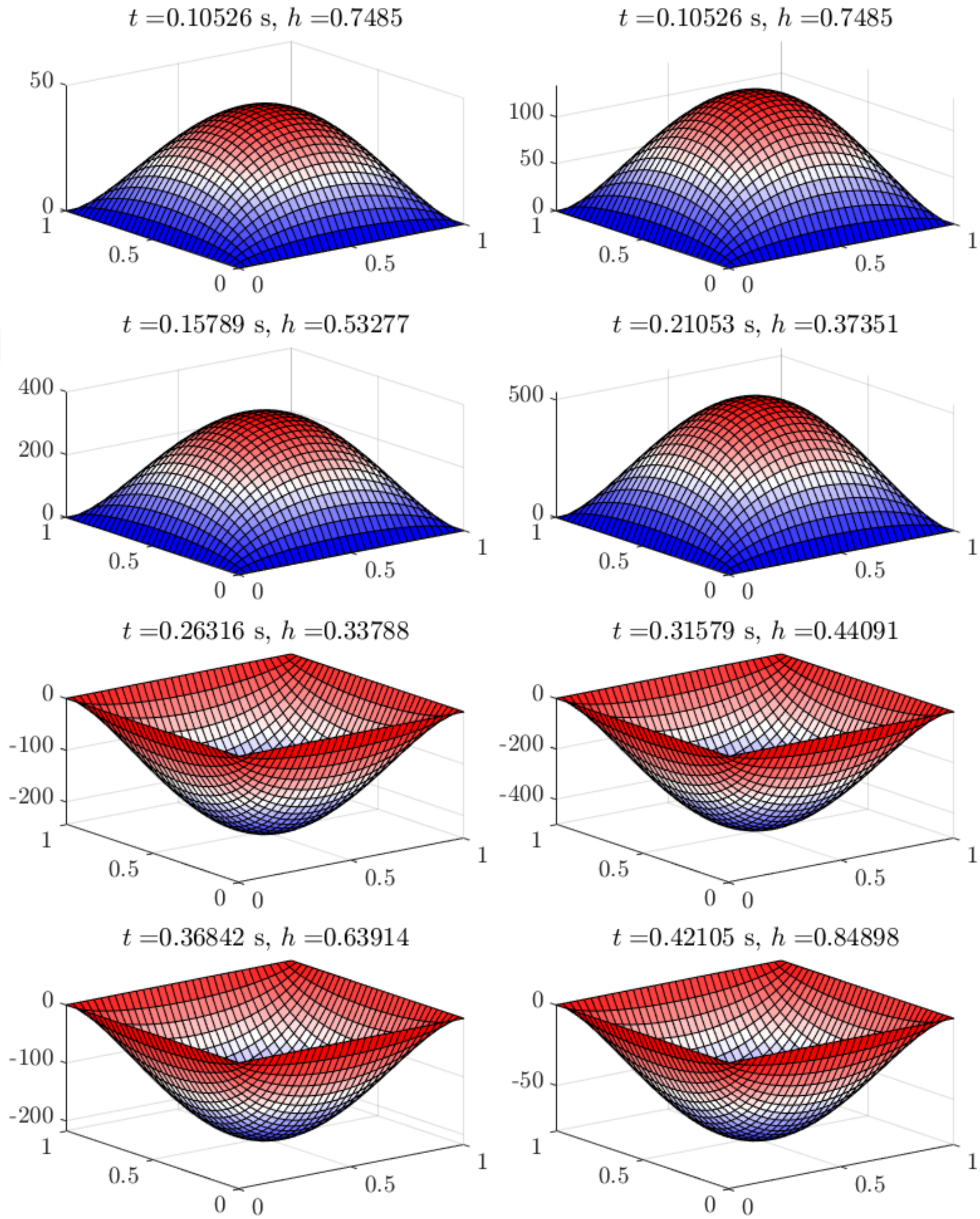

Figure 4.22: 2D PCST LRE Results for the squeeze film flow over time, using new Newton-Raphson Scheme for $\nabla_x p_0$ at $\omega = 128$. $y/h = \chi = 0.75$ and $A = 0.20$.

With this approximation on homogenization and a slight modification to the

Newton-Raphson scheme with respect to the ∇p_0 shown on Eq. 4.3, a maximum error of 0.67% is acquired for the squeeze film pressure distributions. Hence, one may use the same numerical framework with a slight approximation, for energy dissipation minimization. The dissipation minimization is carried out using triangular sectors as shown on Fig. 4.23, due to the fact that the squeeze film pressure distribution is symmetric both in streamwise and spanwise axes.

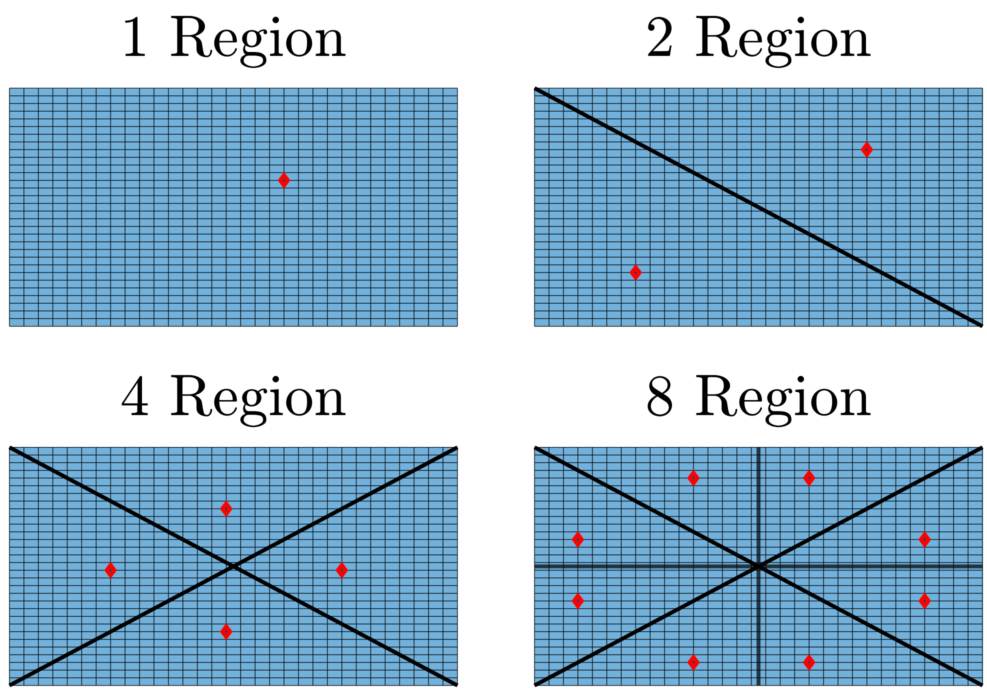

Figure 4.23: Triangular Sectoring with regions $N = 1, 2, 4, 8$. Red markers indicate the point in which ∇p_0, p_0 and h values are taken for optimization input, while the black lines indicate the region borders.

For single region optimization, the specimen point is taken to be a different coordinate than the center, as the ∇p_0 value is negligible; leading to a failure of optimization scheme. The textures for Newtonian and PCST fluid flows can be found for different setups from Fig.4.24 to Fig. 4.31 shown below. To assess the performance of the optimization scheme, dimples were also enforced in some cases to reach a comparative basis, as they are known from previous results of [57] to minimize energy dissipation.

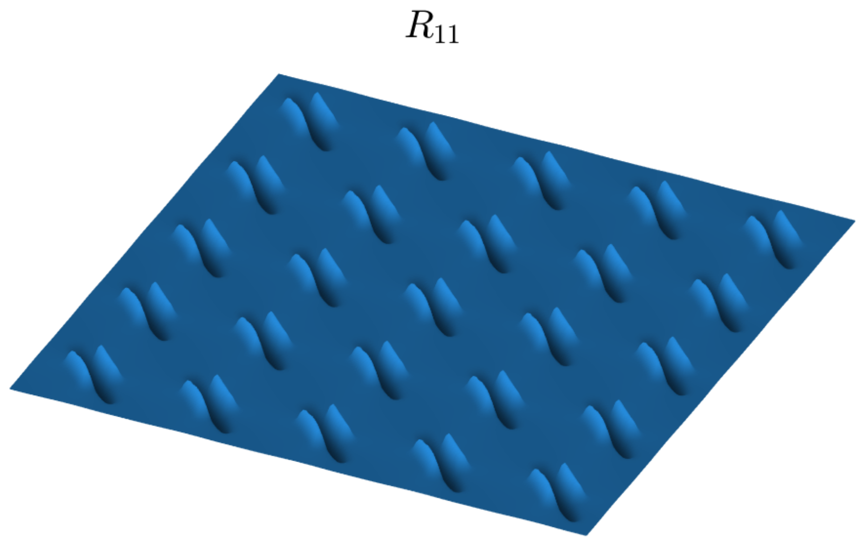

Figure 4.24: Texture obtained with triangular sectoring of a single region for Newtonian fluid.

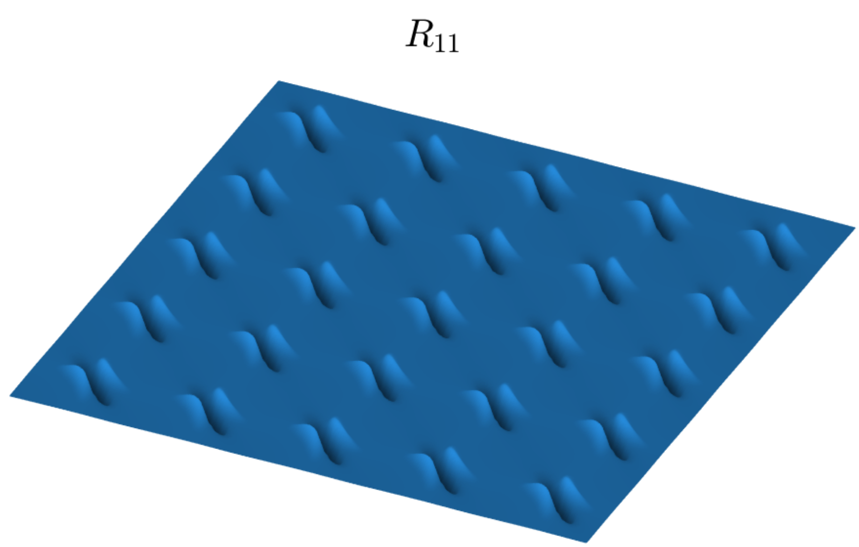

Figure 4.25: Texture obtained with triangular sectoring of a single region for PCST fluid.

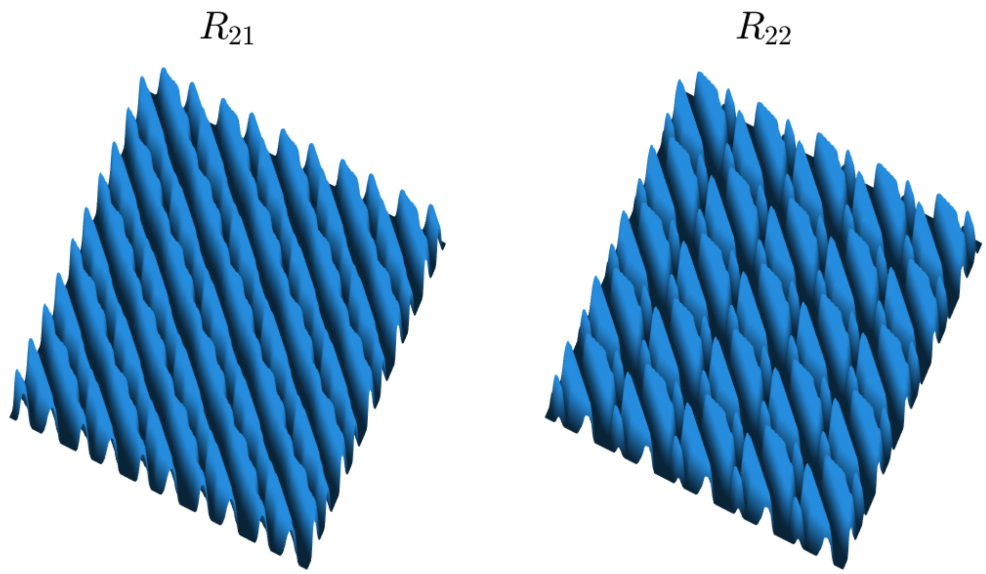

Figure 4.26: Textures obtained with triangular sectoring of 2 region partition for Newtonian fluid.

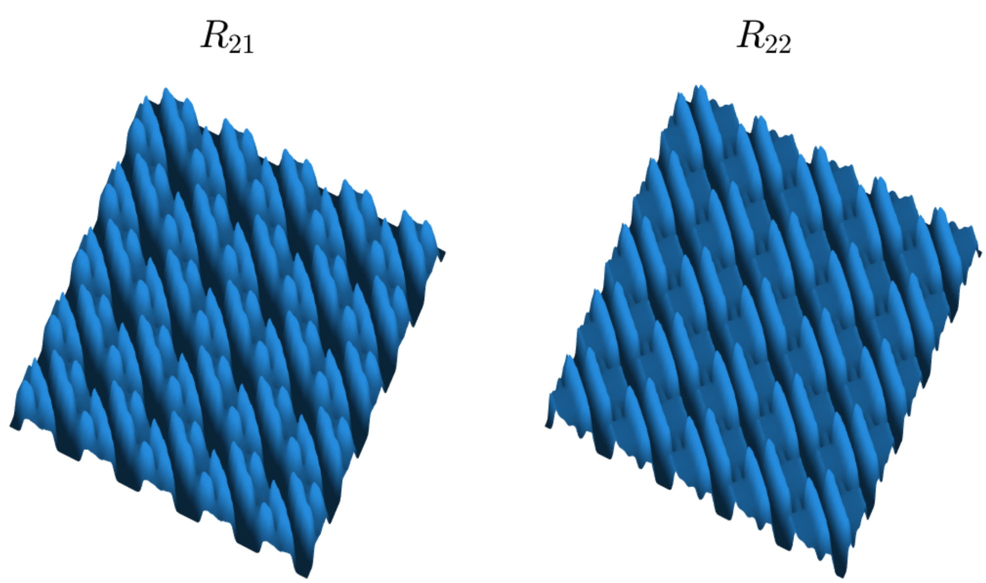

Figure 4.27: Textures obtained with triangular sectoring of 2 region partition for PCST fluid.

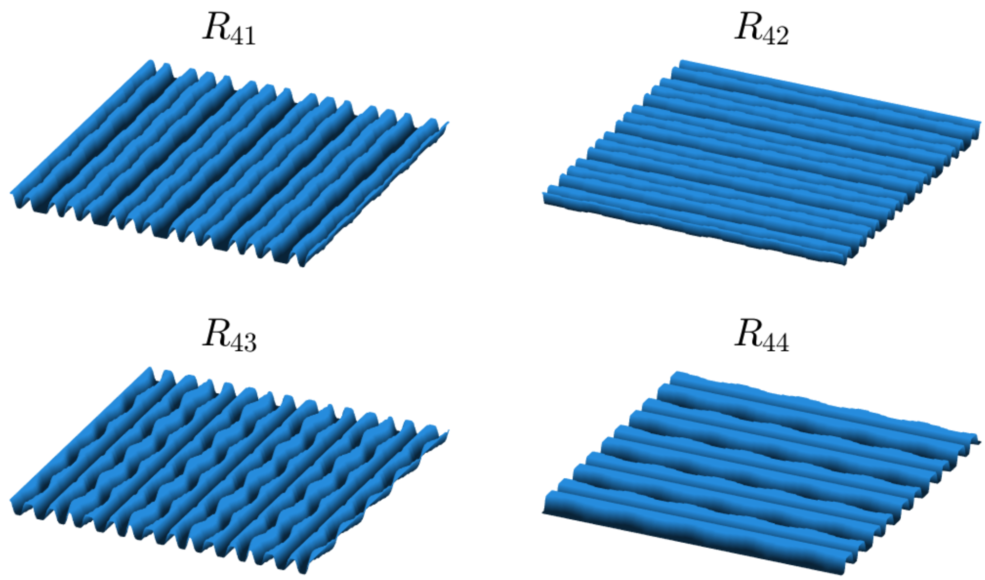

Figure 4.28: Textures obtained with triangular sectoring of 4 region partition for Newtonian fluid.

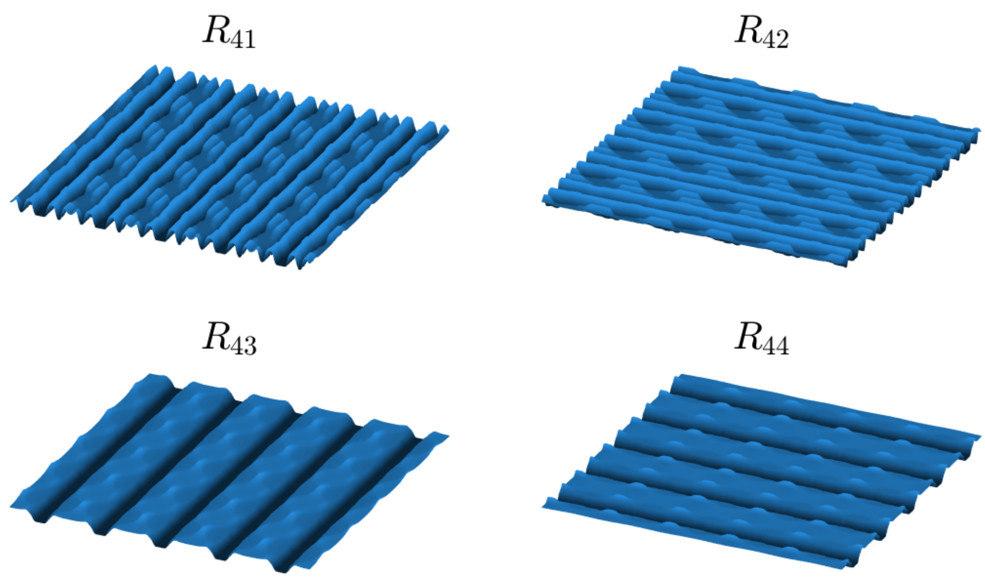

Figure 4.29: Textures obtained with triangular sectoring of 4 region partition for PCST fluid.

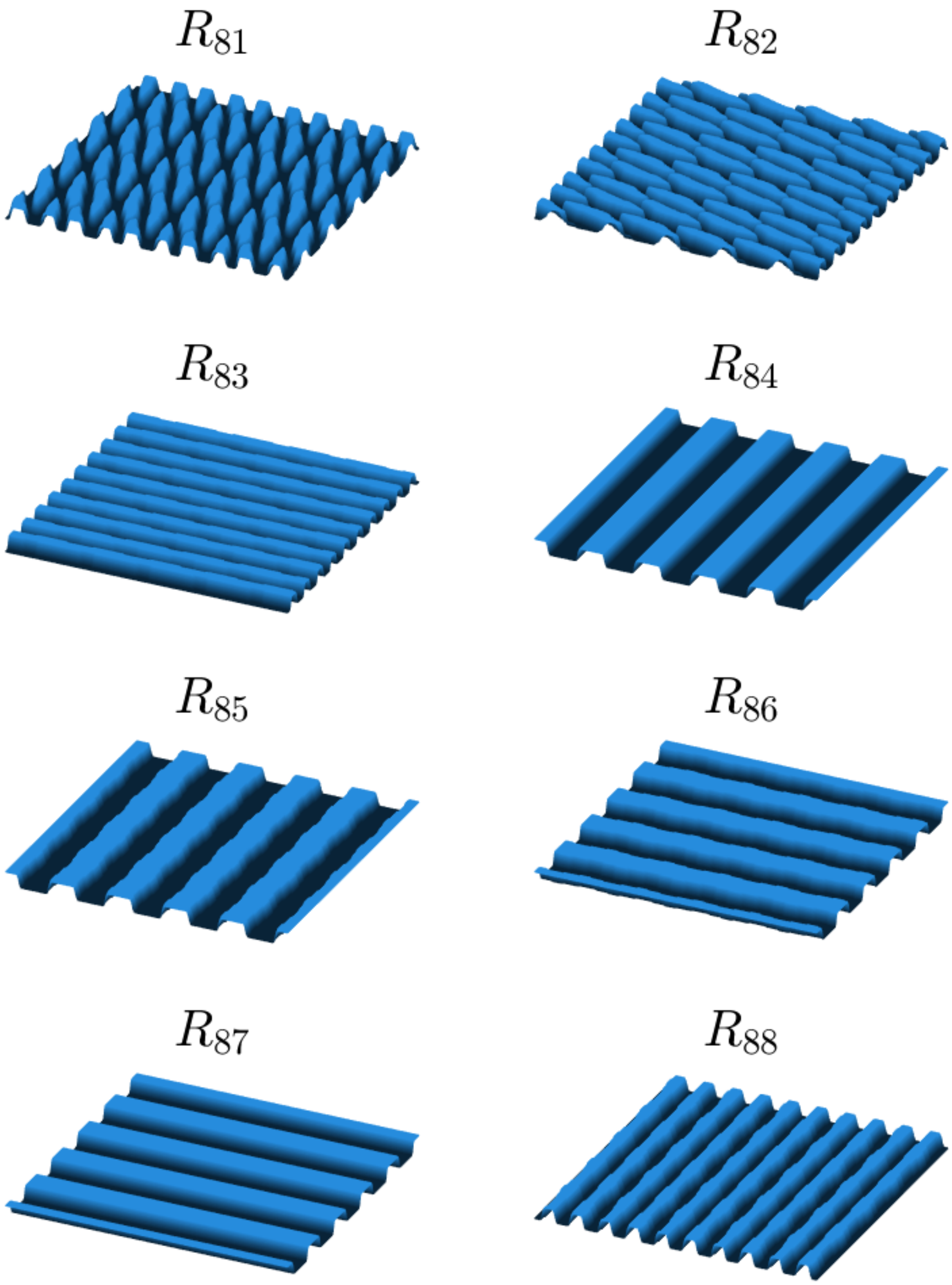

Figure 4.30: Textures obtained with triangular sectoring of 8 region partition for Newtonian fluid.

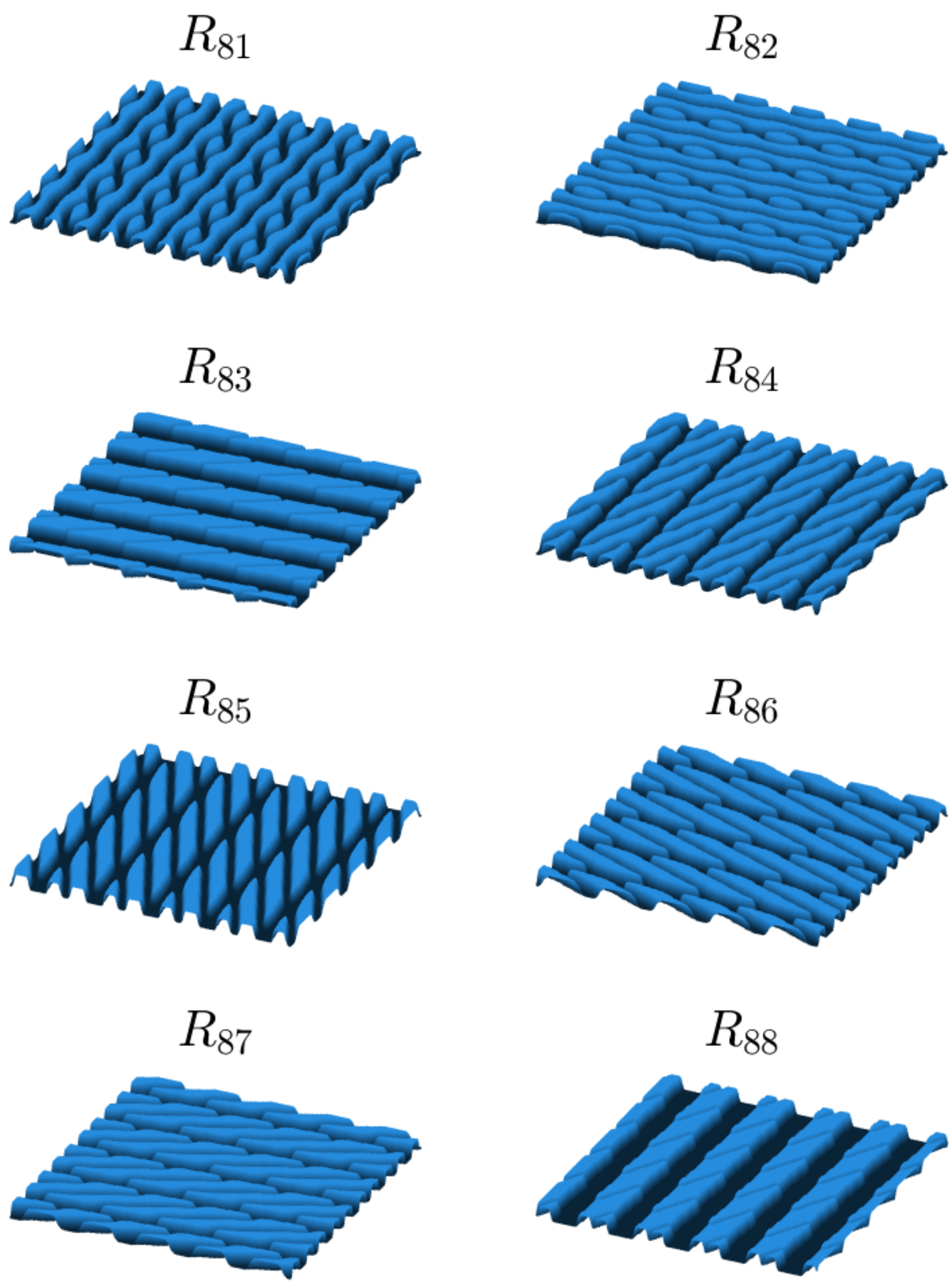

Figure 4.31: Textures obtained with triangular sectoring of 8 region partition for PCST fluid.

Compared to the textures shown above, dimple textures illustrated below have less variety, mostly due to it having a better geometry fitting to the optimization constraints discussed in Sec. 4.3. Regardless of the similar appearances for both Newtonian and PCST fluid flows, the depth and height of dimples are not the same.

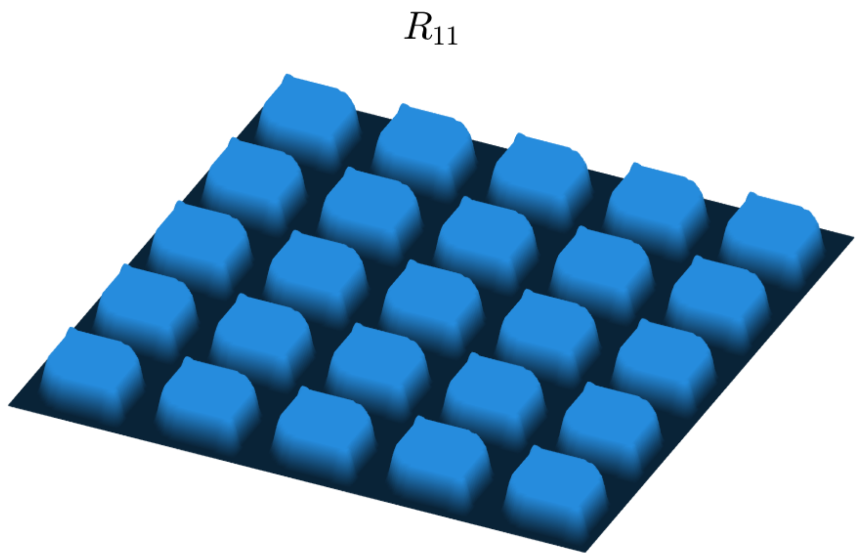

Figure 4.32: Dimple Texture obtained with triangular sectoring of a single region for Newtonian fluid.

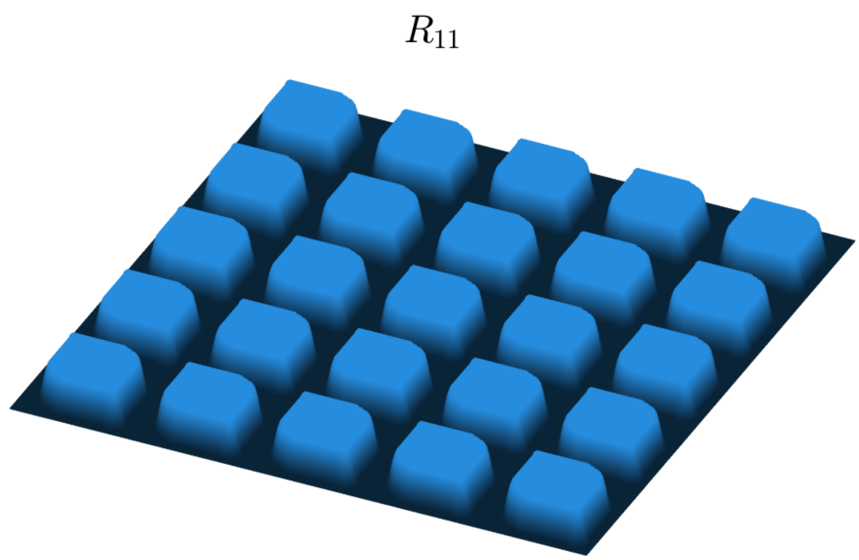

Figure 4.33: Dimple Texture obtained with triangular sectoring of a single region for PCST fluid.

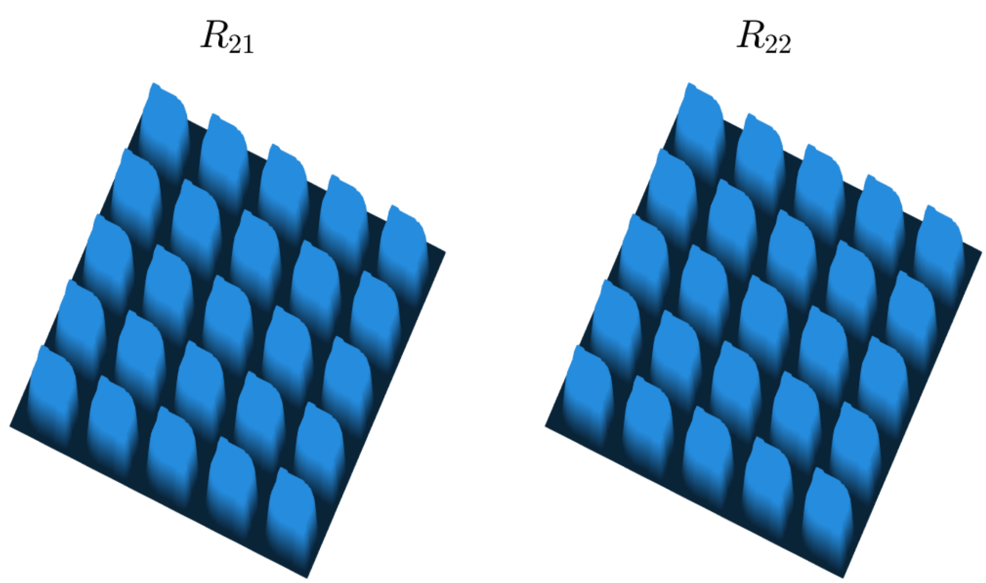

Figure 4.34: Dimple Textures obtained with triangular sectoring of 2 region partition for Newtonian fluid.

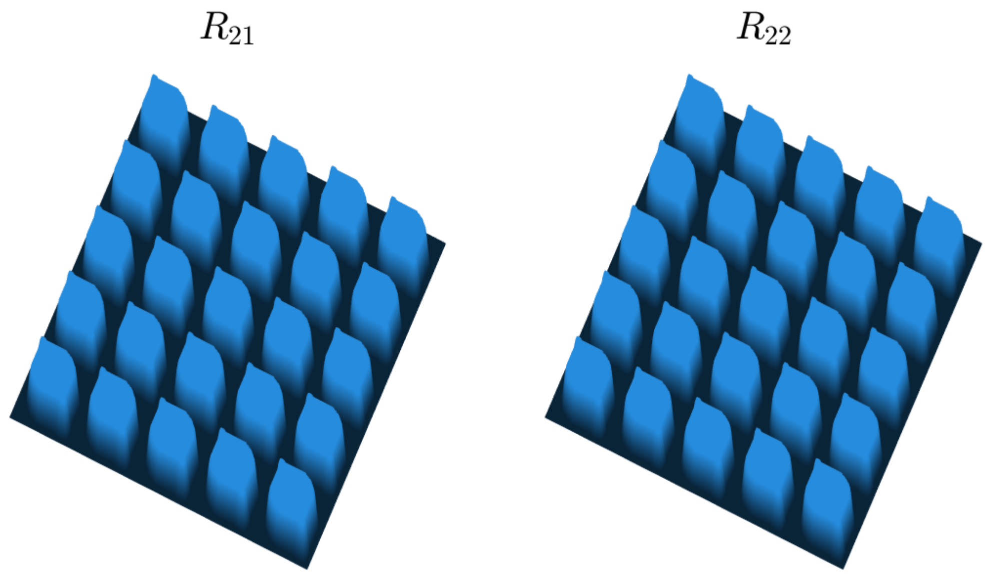

Figure 4.35: Dimple Textures obtained with triangular sectoring of 2 region partition for PCST fluid.

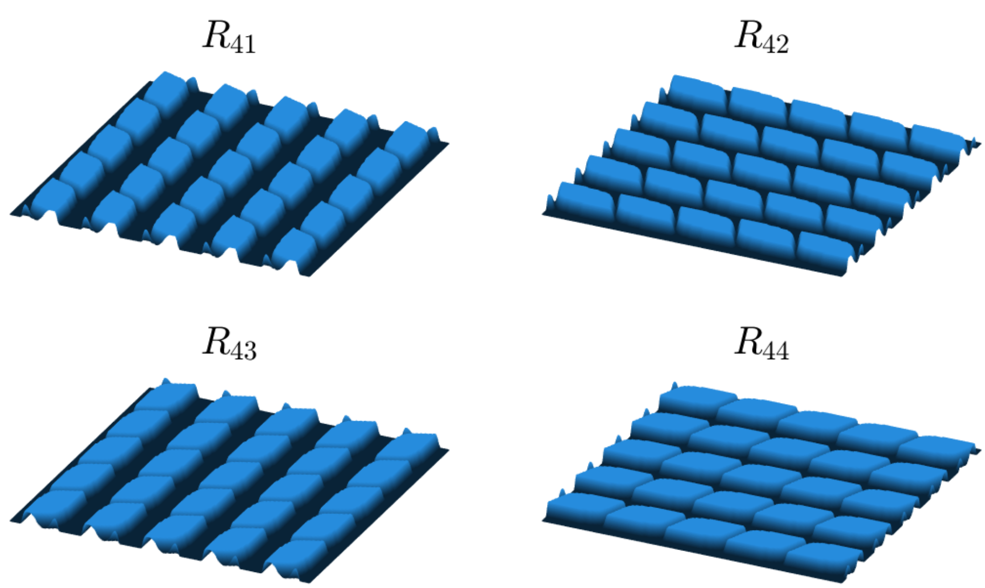

Figure 4.36: Dimple Textures obtained with triangular sectoring of 4 region partition for Newtonian fluid.

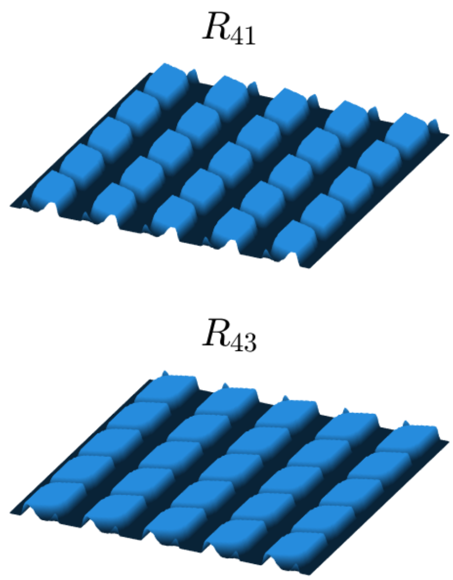

Figure 4.37: Dimple Textures obtained with triangular sectoring of 4 region partition for PCST fluid.

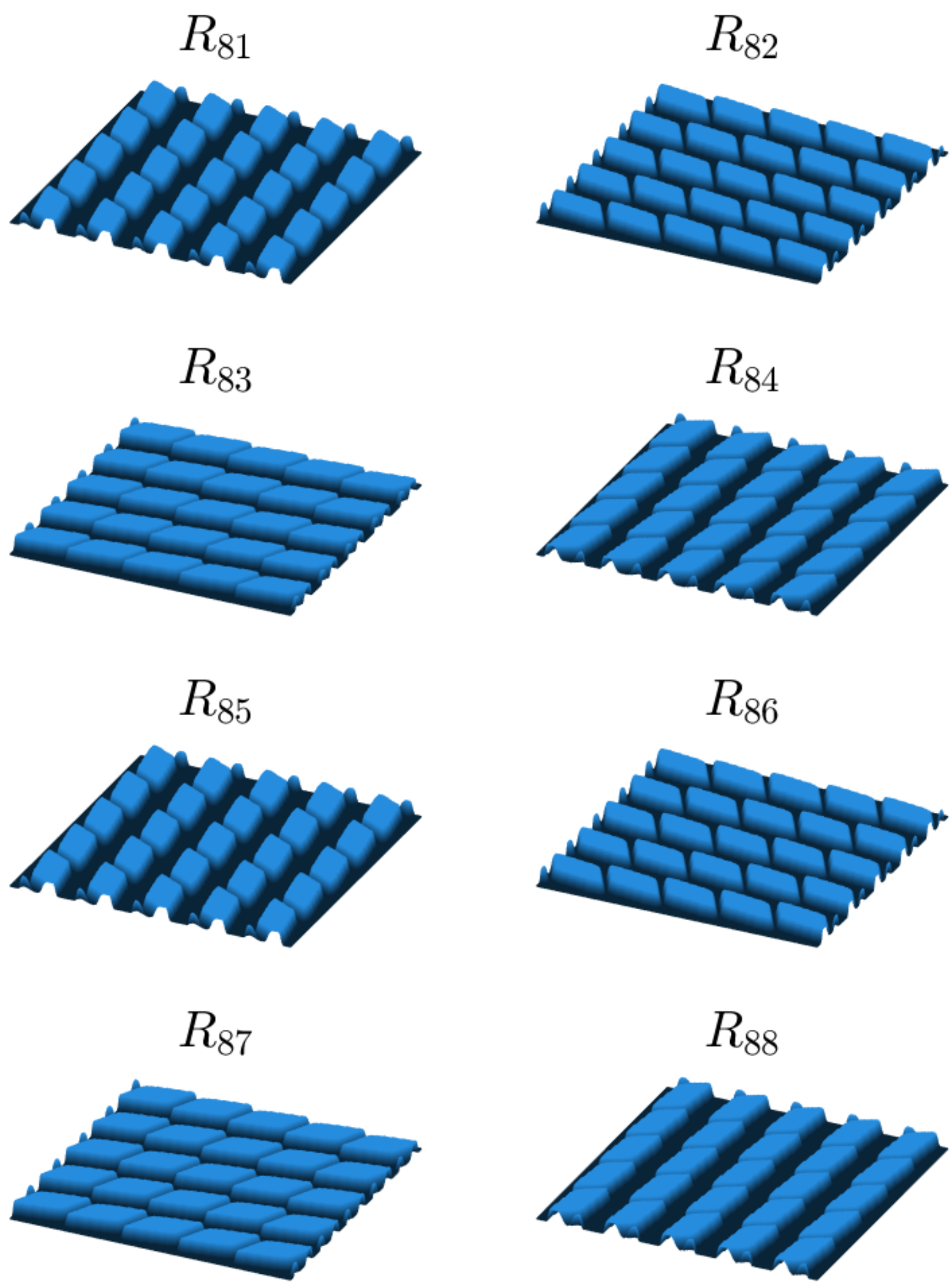

Figure 4.38: Dimple Textures obtained with triangular sectoring of 8 region partition for Newtonian fluid.

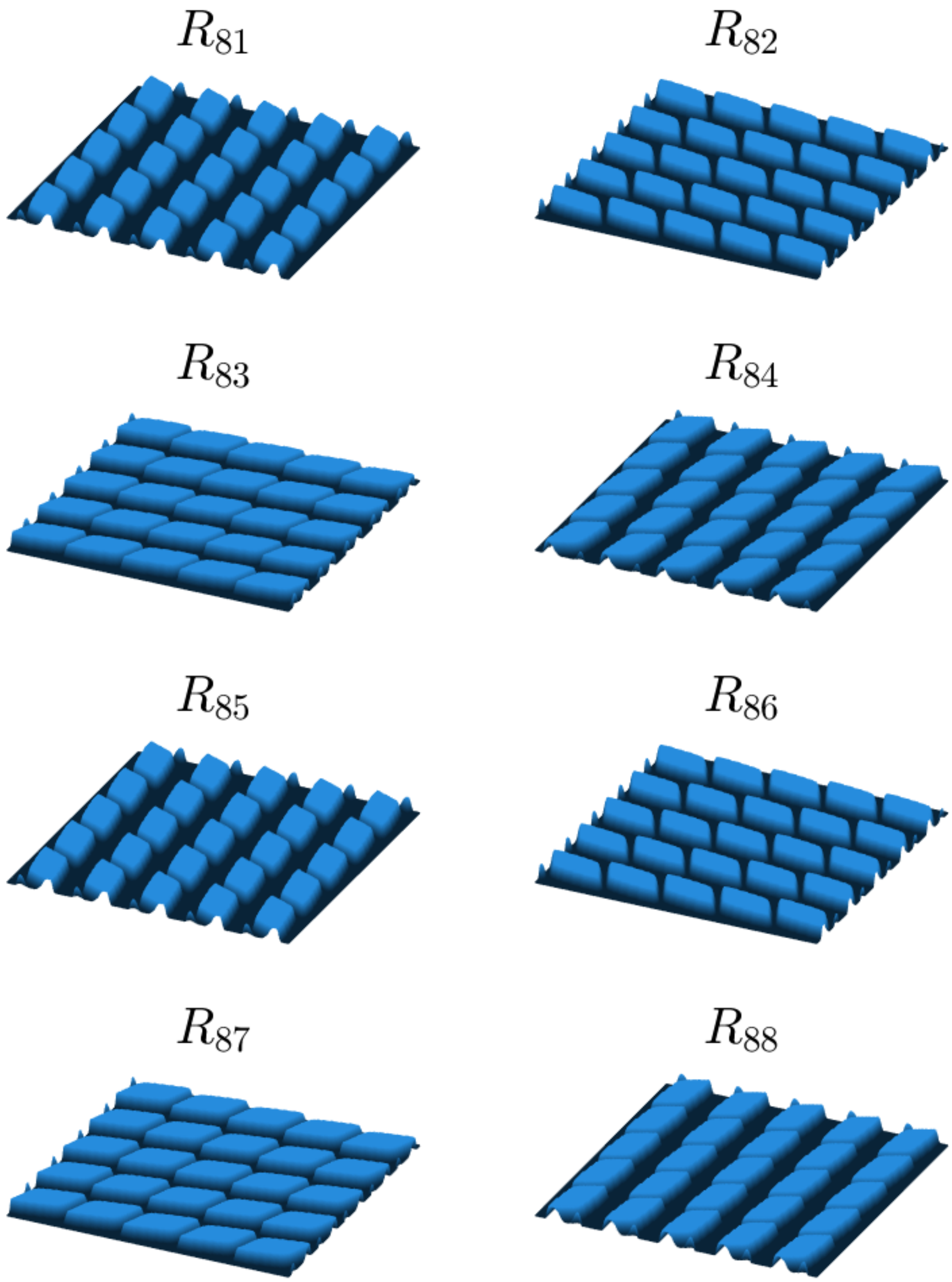

Figure 4.39: Dimple Textures obtained with triangular sectoring of 8 region partition for PCST fluid.

The textures lead to an ϕ_A distribution for different number of domain partitions, as shown below on Fig. 4.40 for Newtonian rheology. The region borders can be distinguished by the formation of valleys and hills on the edges of the domain. Since ∇p_0 is higher in the edges, decreasing towards the center, the ϕ_A is also way larger on the outer parts.

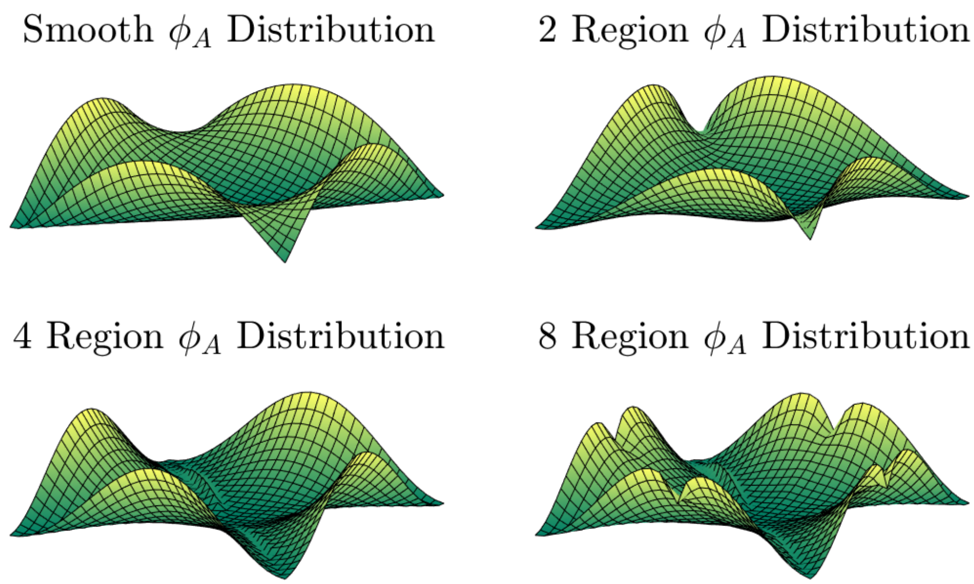

Figure 4.40: Dimple Textures ϕ_A distribution for different number of domain partitions.

The energy dissipation results, in their normalized forms with respect to the smooth energy dissipation ϕ_0 can be found for different rheology fluids with respect to the number of domain divisions on Figs. 4.41, 4.42, 4.43 provided below:

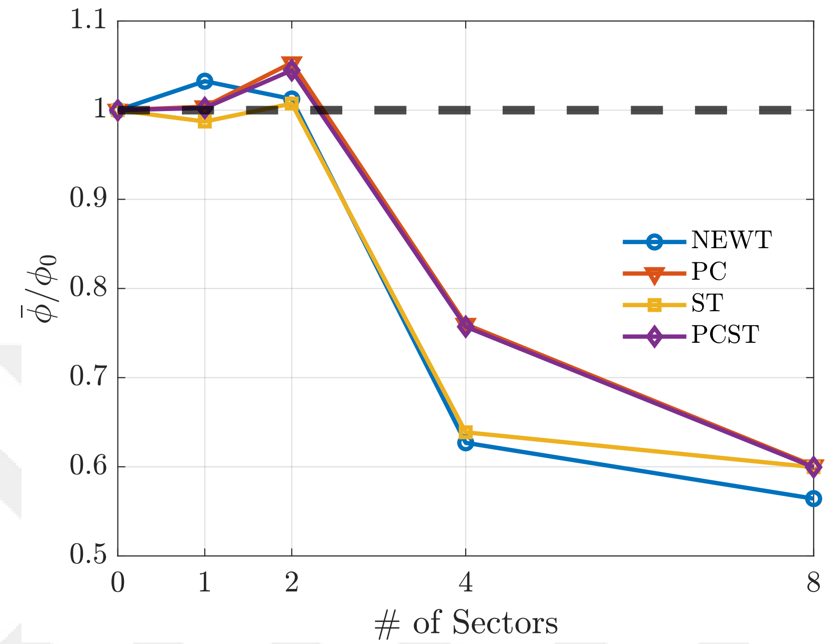

Figure 4.41: Triangular Sectoring Dissipation Minimization with respect to # of sectors for different rheology fluids. ϕ_0 is the smooth dissipation and $\bar{\phi}$ is the textured dissipation. $\tau_0 = 20$.

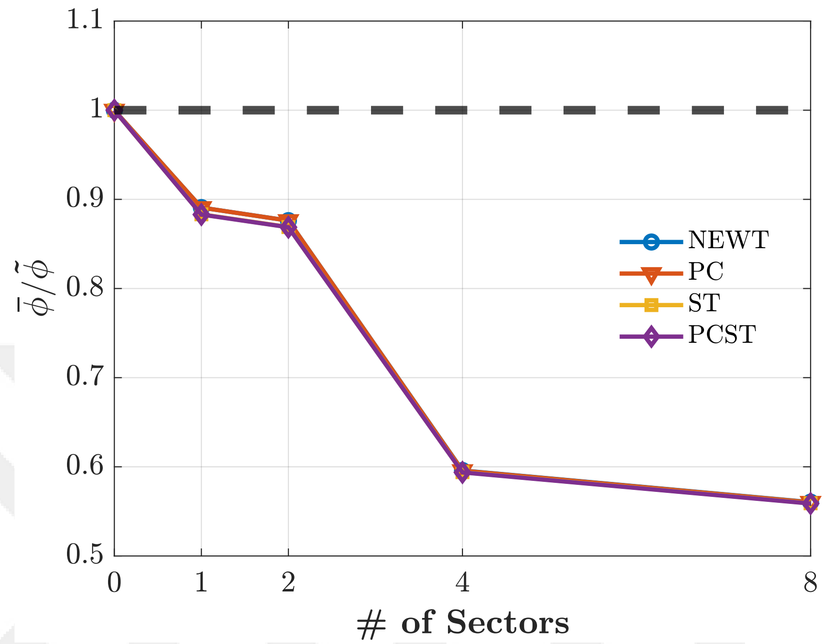

Figure 4.42: Newtonian Dimple texture enforced triangular Sectoring Dissipation Minimization with respect to # of sectors for different rheology fluids. ϕ_0 is the smooth dissipation and $\bar{\phi}$ is the textured dissipation. $\tau_0 = 20$.

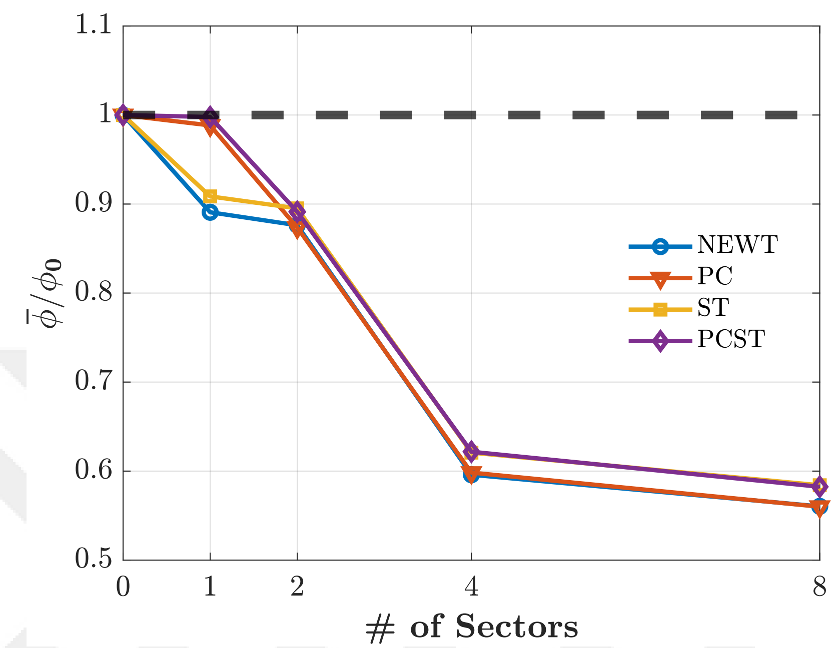

Figure 4.43: Dimple texture enforced triangular Sectoring Dissipation Minimization with respect to # of sectors for different rheology fluids. ϕ_0 is the smooth dissipation and $\bar{\phi}$ is the textured dissipation. $\tau_0 = 20$.

It can be observed from results that the energy dissipation minimization attempts fail for low number of regions when dimples are not enforced as a surface geometry. Regardless, increasing the partitioning to 4 sectors, leads to a substantial reduction in energy dissipation, compared to the utilization of 1 and 2 sector divisions. Furthermore, reduction in energy dissipation seems to be irrelevant from 4 division onwards, as the drop is insignificant. Therefore, for the squeeze film applications usage of 4 sectors may prove to be quite effective in reducing energy dissipation for lubrication applications. Furthermore, as it can be observed from Fig. 4.42, application of the same texture leads to approximately the same trend in energy dissipation drop; irrelevant of the fluid rheology. That is, texture dominates over the lubricant rheology. One may find the additional textures used for energy dissipation maximization and minimization for PC and ST fluids in Appendix A.1.

Chapter 5

Conclusions

Thus, a novel homogenization-based computational framework that can be used for texture optimization of hydrodynamic interfaces lubricated by variable viscosity and density liquids by efficient means is achieved in this work. A plane slider and a squeeze film was utilized in this work to highlight the applicability of the optimization scheme in tribology applications involving bearings.

A homogenized model that is applicable both in 1D and 2D studies, is derived by exploiting the modified viscosity approach for a piezoviscous, compressible and shear-thinning fluid. Although literature includes similar homogenized models for Newtonian and non-Newtonian effects, no such model that takes advantage of modified viscosity approach to get a highly simplified and accurate homogenized LRE can be found in the past literature. The model is then thoroughly validated by comparing the homogenized LRE with direct LRE solutions and DNS solutions for a piezoviscous and shear-thinning fluids. Results illustrate a great agreement for both LRE and DNS. Hence, a valid homogenized model that significantly alleviate the computational difficulty of resolving roughness in low scales is obtained in a rigorous manner.

A further validation is also carried out for the traction τ on the interface surfaces, as it is a crucial parameter for the analysis and modulation of friction for energy losses. The homogenized model also has great agreement with DNS for a highly oscillatory quantity such as traction even for quite high frequency sinusoidal roughness profiles.

By utilizing the same finite elements framework used in pressure solutions, the homogenized model is then used for the optimization of the surface textures for energy dissipation minimization and maximization was done with MMA, as it is ultimate goal of lubrication applications to alter ϕ by manipulating friction. For both cases, results are highly satisfactory, with a clear difference in the performance of maximization and minimization between different rheology lubricants. PCST fluid creates the highest energy dissipation ϕ maximization, whereas, for minimization, Newtonian fluid is simply the overall best. For applications necessitating increased grip, like CVT and wheel train transmission, the friction increasing surfaces can be coupled with PCST fluid. For energy dissipation minimization, periodic dimple geometries can be utilized coupled with Newtonian fluids. It should be noted that because piezoviscosity is dependent on pressure to be quite high in the domain, whether it can be achieved for such applications as listed previously must be delved further.

Further correlaries related to the texture shapes and partitioning of the domain can be made by observing the illustrations. The texture dominates over rheology, as combining the exactly same geometries with different fluid rheologies lead to a highly similar trend, which indicates that rheology is ineffective when textures are not optimized with respect to the possible non-linear effects. Moreover, while the division of domain into smaller partitions indeed results in a better optimization performance with increasing number of sub-sectors, it seems to result in a significant change from $N = 2$ to $N = 4$, with a quite apparent stagnation for higher number of N. Hence, for both practical purposes such as manufacturability, and provided that computational findings do reflect the real response in good agreement, the divisions higher than $N = 2$ and $N = 4$ may be unnecessary and unrealizable.

On the other hand, while the homogenized model is shown to be valid for a wide range of periodic roughness profiles, this is an approximation in its base.

It is expected that instead of trying to resolve the true roughness, homogenized LRE analyses of the optimized textures should yield an adequate result to the real response; by taking advantage of the modern micro and nano manufacturing techniques. It should also be highlighted once again that, energy minimization with texture application is restricted to the interfaces where streamwise and spanwise velocities eliminated, which limits the applicability of it to a handful lubrication applications.

Lastly, it was mentioned that under high pressure conditions as studied in this work, the viscoelastic effects should also be accounted for ideally. Provided that the current homogenization based numerical framework is extended to the viscoelastic lubricants while employing accurate models, a major practical advantage can be gained for computational tribology studies.

Bibliography

[1] B. J. Hamrock, S. R. Schmid, and B. O. Jacobson, *Fundamentals of Fluid Film Lubrication.* Marcel Dekker, 2004.

[2] A. Z. Szeri, *Fluid Film Lubrication.* Cambridge University Press, 12 2010.

[3] I. Tzanakis, M. Hadfield, B. Thomas, S. Noya, I. Henshaw, and S. Austen, "Future perspectives on sustainable tribology," *Renewable and Sustainable Energy Reviews*, vol. 16, pp. 4126–4140, 08 2012.

[4] L. Rayleigh, "I. notes on the theory of lubrication," *The London, Edinburgh, and Dublin Philosophical Magazine and Journal of Science*, vol. 35, pp. 1–12, 01 1918.

[5] A. Codrignani, D. Savio, L. Pastewka, B. Frohnapfel, and R. van Ostayen, "Optimization of surface textures in hydrodynamic lubrication through the adjoint method," *Tribology International*, vol. 148, pp. 106352–106352, 08 2020.

[6] M. P. Bendsøe and O. Sigmund, *Topology Optimization.* Springer Berlin Heidelberg, 2004.

[7] P. W. Christensen, A. Klarbring, and S. O. Service, *An Introduction to Structural Optimization.* Springer Netherlands, 2009.

[8] D. B. Hamilton, J. A. Walowit, and C. M. Allen, "A theory of lubrication by microirregularities," *Journal of Basic Engineering*, vol. 88, p. 177, 1966.

[9] D. Gropper, L. Wang, and T. J. Harvey, "Hydrodynamic lubrication of textured surfaces: A review of modeling techniques and key findings," *Tribology International*, vol. 94, pp. 509–529, 02 2016.

[10] A. Vakis, V. Yastrebov, J. Scheibert, L. Nicola, D. Dini, C. Minfray, A. Almqvist, M. Paggi, S. Lee, G. Limbert, J. Molinari, G. Anciaux, R. Aghababaei, S. Echeverri Restrepo, A. Papangelo, A. Cammarata, P. Nicolini, C. Putignano, G. Carbone, S. Stupkiewicz, J. Lengiewicz, G. Costagliola, F. Bosia, R. Guarino, N. Pugno, M. Müser, and M. Ciavarella, "Modeling and simulation in tribology across scales: An overview," *Tribology International*, vol. 125, pp. 169–199, 09 2018.

[11] B. Veltkamp, J. Jagielka, K. Velikov, and D. Bonn, "Lubrication with non-newtonian fluids," *Physical review applied*, vol. 19, 01 2023.

[12] T. Almqvist and R. Larsson, "Some remarks on the validity of reynolds equation in the modeling of lubricant film flows on the surface roughness scale," *Journal of Tribology*, vol. 126, p. 703–710, 10 2004.

[13] O. Reynolds, "Iv. on the theory of lubrication and its application to mr. beauchamp tower's experiments, including an experimental determination of the viscosity of olive oil," *Philosophical Transactions of the Royal Society of London*, vol. 177, pp. 157–234, 01 1886.

[14] W.-z. Wang, H. Chen, Y.-z. Hu, and H. Wang, "Effect of surface roughness parameters on mixed lubrication characteristics," *Tribology International*, vol. 39, pp. 522–527, 06 2006.

[15] G. Bayada, S. Martin, and C. Vázquez, "Micro-roughness effects in (elasto)hydrodynamic lubrication including a mass-flow preserving cavitation model," *Tribology International*, vol. 39, pp. 1707–1718, 12 2006.

[16] A. Almqvist, *On the effects of surface roughness in lubrication*. PhD thesis, 2006.

[17] G. Bayada and M. Chambat, "The transition between the stokes equations and the reynolds equation: A mathematical proof," *Applied Mathematics & Optimization*, vol. 14, pp. 73–93, 04 1986.

[18] I. N. Yıldıran, I. Temizer, and B. Çetin, "Homogenization in hydrodynamic lubrication: Microscopic regimes and re-entrant textures," *Journal of Tribology*, vol. 140, 07 2017.

[19] G. Bayada and M. Chambat, "New models in the theory of the hydrodynamic lubrication of rough surfaces," *Journal of Tribology*, vol. 110, pp. 402–407, 07 1988.

[20] Y. Mitsuya and S. Fukui, "Stokes roughness effects on hydrodynamic lubrication. part i—comparison between incompressible and compressible lubricating films," *Journal of Tribology*, vol. 108, pp. 151–158, 04 1986.

[21] J. Y. Jang and M. M. Khonsari, *Lubrication with a Newtonian Fluid*, pp. 2142–2146. Boston, MA: Springer US, 2013.

[22] H. Ahmed and L. Biancofiore, "A modified viscosity approach for shear thinning lubricants," *Physics of Fluids*, vol. 34, p. 103103, 10 2022.

[23] J. M. Bennett, "Recent developments in surface roughness characterization," *Measurement Science and Technology*, vol. 3, pp. 1119–1127, 12 1992.

[24] M. Anguiano and F. J. Suárez-Grau, "Nonlinear reynolds equations for non-newtonian thin-film fluid flows over a rough boundary," *IMA Journal of Applied Mathematics*, vol. 84, pp. 63–95, 10 2018.

[25] M. Anguiano, "Homogenization of a non-stationary non-newtonian flow in a porous medium containing a thin fissure," *European Journal of Applied Mathematics*, vol. 30, pp. 248–277, 02 2018.

[26] S. Bair and W. Winer, "Some observations in high pressure rheology of lubricants," *Journal of Lubrication Technology*, vol. 104, pp. 357–364, 07 1982.

[27] F. Pérez-Ràfols, P. Wall, and A. Almqvist, "On compressible and piezoviscous flow in thin porous media," *Proceedings of the Royal Society A: Mathematical, Physical and Engineering Sciences*, vol. 474, p. 20170601, 01 2018.

[28] J. M. Skotheim and L. Mahadevan, “Soft lubrication,” *Physical Review Letters*, vol. 92, 06 2004.

[29] S. Stupkiewicz, J. Lengiewicz, P. Sadowski, and S. Kucharski, “Finite deformation effects in soft elastohydrodynamic lubrication problems,” *Tribology International*, vol. 93, pp. 511–522, 01 2016.

[30] T. Almqvist, A. Almqvist, and R. Larsson, “A comparison between computational fluid dynamic and reynolds approaches for simulating transient ehl line contacts,” *Tribology International*, vol. 37, p. 61–69, 01 2004.

[31] I. Temizer and S. Stupkiewicz, “Formulation of the reynolds equation on a time-dependent lubrication surface,” *Proceedings - Royal Society. Mathematical, Physical and Engineering Sciences*, vol. 472, pp. 20160032–20160032, 03 2016.

[32] G. E. Morales-Espejel, “Surface roughness effects in elastohydrodynamic lubrication: A review with contributions,” *Proceedings of the Institution of Mechanical Engineers, Part J: Journal of Engineering Tribology*, vol. 228, pp. 1217–1242, 12 2013.

[33] H. P. Evans, R. W. Snidle, and K. Sharif, “Deterministic mixed lubrication modelling using roughness measurements in gear applications,” *Tribology International*, vol. 42, pp. 1406–1417, 10 2009.

[34] D. Dowson, “A generalized reynolds equation for fluid-film lubrication,” *International Journal of Mechanical Sciences*, vol. 4, p. 159–170, 03 1962.

[35] Y. Peiran and W. Shizhu, “A generalized reynolds equation for non-newtonian thermal elastohydrodynamic lubrication,” *Journal of Tribology*, vol. 112, pp. 631–636, 10 1990.

[36] J. Shukla, S. Kumar, and P. Chandra, “Generalized reynolds equation with slip at bearing surfaces: Multiple-layer lubrication theory,” *Wear*, vol. 60, pp. 253–268, 05 1980.

[37] R. Wolff and A. Kubo, "A generalized non-newtonian fluid model incorporated into elastohydrodynamic lubrication," *Journal of Tribology*, vol. 118, pp. 74–82, 01 1996.

[38] Q. Yang, P. Huang, and Y. Fang, "A novel reynolds equation of non-newtonian fluid for lubrication simulation," *Tribology international*, vol. 94, pp. 458–463, 02 2016.

[39] B. Najji, B. Bou-Said, and D. Berthe, "New formulation for lubrication with non-newtonian fluids," *Journal of Tribology*, vol. 111, pp. 29–34, 01 1989.

[40] T. Gustafsson, K. Rajagopal, R. Stenberg, and J. Videman, "Nonlinear reynolds equation for hydrodynamic lubrication," *Applied Mathematical Modelling*, vol. 39, pp. 5299–5309, 09 2015.

[41] I. K. Dien and H. G. Elrod, "A generalized steady-state reynolds equation for non-newtonian fluids, with application to journal bearings," *Journal of Lubrication Technology*, vol. 105, pp. 385–390, 07 1983.

[42] X. K. Li, "Non-newtonian lubrication with the phan-thien–tanner model," *Journal of Engineering Mathematics*, vol. 87, pp. 1–17, 08 2013.

[43] G. Bayada, L. Chupin, and B. Grec, "Viscoelastic fluids in thin domains: a mathematical proof," *Asymptotic Analysis*, vol. 64, pp. 185–211, 2009.

[44] G. Bayada, L. Chupin, and S. Martin, "Non newtonian visco-elastic olroyd-b model for lubrication," 11 2010.

[45] F. T. Akyildiz and H. Bellout, "Viscoelastic lubrication with phan-thein-tanner fluid (ptt)," *Journal of Tribology*, vol. 126, pp. 288–291, 04 2004.

[46] S. Torquato, *Random Heterogeneous Materials*. Springer Science & Business Media, 04 2013.

[47] P. Wall, "Homogenization of reynolds equation by two-scale convergence," *Chinese Annals of mathematics. Ser. B/Chinese Annals of mathematics. Series B*, vol. 28, pp. 363–374, 04 2007.

[48] G. Pavliotis and A. Stuart, *Multiscale Methods*. Springer Science & Business Media, 01 2008.

[49] A. Waseem, I. Temizer, J. Kato, and K. Terada, "Homogenization-based design of surface textures in hydrodynamic lubrication," *International Journal for Numerical Methods in Engineering*, vol. 108, pp. 1427–1450, 04 2016.

[50] G. Bayada and M. Chambat, "Homogenization of the stokes system in a thin film flow with rapidly varying thickness," *Mathematical Modeling and Numerical Analysis*, vol. 23, pp. 205–234, 01 1989.

[51] G. Bayada, *Paper III(i) - Application of the homogenization method to Reynolds roughness*, pp. 53–59. Butterworth-Heinemann, 1984.

[52] J. H. Tripp, "Surface roughness effects in hydrodynamic lubrication: the flow factor method," *Journal of Lubrication Technology*, vol. 105, pp. 458–463, 07 1983.

[53] D. c. Sun, "On the effects of two-dimensional reynolds roughness in hydrodynamic lubrication," *Proceedings of the Royal Society of London. Series A, Mathematical and Physical Sciences*, vol. 364, pp. 89–106, 12 1978.

[54] H. G. Elrod, "A general theory for laminar lubrication with reynolds roughness," *Journal of Lubrication Technology*, vol. 101, pp. 8–14, 01 1979.

[55] A. Almqvist, E. Essel, L.-E. Persson, and P. Wall, "Homogenization of the unstationary incompressible reynolds equation," *Tribology international*, vol. 40, pp. 1344–1350, 09 2007.

[56] E. N. Ahmed, A. Bottaro, and G. Tanda, "A homogenization approach for buoyancy-induced flows over micro-textured vertical surfaces," *Journal of Fluid Mechanics*, vol. 941, 05 2022.

[57] A. Waseem, I. Temizer, J. Kato, and K. Terada, "Micro-texture design and optimization in hydrodynamic lubrication via two-scale analysis," *Structural and Multidisciplinary Optimization*, vol. 56, pp. 227–248, 05 2017.

[58] G. Buscaglia and M. Jai, "Sensitivity analysis and taylor expansions in numerical homogenization problems," *Numerische Mathematik*, vol. 85, pp. 49–75, 03 2000.

[59] M. Anguiano and R. Bunoiu, "Homogenization of bingham flow in thin porous media," *Networks and heterogeneous media*, vol. 15, pp. 87–110, 01 2020.

[60] F. J. Suárez-Grau, "Homogenization of a micropolar fluid past a porous media with nonzero spin boundary condition," *Mathematical Methods in the Applied Sciences*, vol. 44, pp. 4835–4857, 12 2020.

[61] M. Anguiano, M. Bonnivard, and F. J. Suárez-Grau, "Carreau law for non-newtonian fluid flow through a thin porous media," *Quarterly journal of mechanics and applied mathematics*, vol. 75, pp. 1–27, 02 2022.

[62] A. Bottaro, "Flow over natural or engineered surfaces: an adjoint homogenization perspective," *Journal of Fluid Mechanics*, vol. 877, 08 2019.

[63] A. Bottaro, "Homogenized boundary conditions for micro-textured surfaces," in *50+ Years of AIMETA* (G. Rega, ed.), (Cham), pp. 383–397, Springer International Publishing, 2022.

[64] M. Anguiano and F. J. Suárez-Grau, "The transition between the navier–stokes equations to the darcy equation in a thin porous medium," *Mediterranean Journal of Mathematics*, vol. 15, 02 2018.

[65] Y. Zhengan and Z. Hongxing, "Homogenization of a stationary navier-stokes flow in porous medium with thin film," *Acta Mathematica Scientia*, vol. 28, pp. 963–974, 10 2008.

[66] C. Barus, "Note on the dependence of viscosity on pressure and temperature," *Proceedings of the American Academy of Arts and Sciences*, vol. 27, p. 13, 1891.

[67] P. W. Bridgman, "The effect of pressure on the viscosity of forty-three pure liquids," *Proceedings of the American Academy of Arts and Sciences*, vol. 61, p. 57–99, 1926.

[68] Y.-R. Jeng, B. J. Hamrock, and D. E. Brewe, "Piezoviscous effects in nonconformal contacts lubricated hydrodynamically," *ASLE transactions*, vol. 30, pp. 452–464, 06 1986.

[69] R. W. Hewson, N. Kapur, and P. H. Gaskell, "Analytical and numerical solutions of thin lubricating films for differing shear-thinning viscosity models," *Proceedings of the Institution of Mechanical Engineers. Part J, Journal of Engineering Tribology*, vol. 221, pp. 355–366, 03 2007.

[70] A. Rastogi and R. Gupta, "Accounting for lubricant shear thinning in the design of short journal bearings," *Journal of Rheology*, vol. 35, pp. 589–603, 05 1991.

[71] P. G. Grützmacher, F. J. Profito, and A. Rosenkranz, "Multi-scale surface texturing in tribology—current knowledge and future perspectives," *Lubricants*, vol. 7, p. 95, 10 2019.

[72] C. Gachot, A. Rosenkranz, S. Hsu, and H. Costa, "A critical assessment of surface texturing for friction and wear improvement," *Wear*, vol. 372-373, pp. 21–41, 02 2017.

[73] I. Etsion, "State of the art in laser surface texturing," *Journal of Tribology*, vol. 127, p. 248, 2005.

[74] M. Marian, A. Almqvist, A. Rosenkranz, and M. Fillon, "Numerical micro-texture optimization for lubricated contacts—a critical discussion," *Friction*, vol. 10, 04 2022.

[75] H. L. Costa, J. Schille, and A. Rosenkranz, "Tailored surface textures to increase friction—a review," *Friction*, vol. 10, 03 2022.

[76] N. Srivastava and I. Haque, "Nonlinear dynamics of a friction-limited drive: Application to a chain continuously variable transmission (cvt) system," *Journal of Sound and Vibration*, vol. 321, pp. 319–341, 03 2009.

[77] N. Wang, D. Li, W. Song, S. C. Xiu, and X. Meng, "Effect of surface texture and working gap on the braking performance of the magnetorheological

fluid brake," *Smart Materials and Structures*, vol. 25, pp. 105026–105026, 09 2016.

[78] B. E. Sabey, T. Williams, and G. N. Lupton, "Factors affecting the friction of tires on wet roads," *SAE Technical Papers on CD-ROM/SAE Technical Paper Series*, vol. 79, 02 1970.

[79] I. Etsion, G. Halperin, V. Brizmer, and Y. Kligerman, "Experimental investigation of laser surface textured parallel thrust bearings," *Tribology Letters*, vol. 17, pp. 295–300, 08 2004.

[80] R. Rahmani, A. Shirvani, and H. Shirvani, "Optimization of partially textured parallel thrust bearings with square-shaped micro-dimples," *Tribology Transactions*, vol. 50, pp. 401–406, 06 2007.

[81] R. Rahmani, I. Mirzaee, A. Shirvani, and H. Shirvani, "An analytical approach for analysis and optimisation of slider bearings with infinite width parallel textures," *Tribology International*, vol. 43, pp. 1551–1565, 08 2010.

[82] L. Wang, "Use of structured surfaces for friction and wear control on bearing surfaces," *Surface Topography: Metrology and Properties*, vol. 2, p. 043001, oct 2014.

[83] A. Almqvist, E. K. Essel, J. Fabricius, and P. Wall, "Reiterated homogenization applied in hydrodynamic lubrication," *Proceedings of the Institution of Mechanical Engineers. Part J, Journal of engineering tribology*, vol. 222, pp. 827–841, 07 2008.

[84] M. Scaraggi, "Lubrication of textured surfaces: a general theory for flow and shear stress factors," *Physical Review E*, vol. 86, 08 2012.

[85] M. Scaraggi, "Textured surface hydrodynamic lubrication: Discussion," *Tribology Letters*, vol. 48, pp. 375–391, 08 2012.

[86] M. Rom and S. Müller, "A new model for textured surface lubrication based on a modified reynolds equation including inertia effects," *Tribology International*, vol. 133, pp. 55–66, 05 2019.

[87] B. A. Çakal, I. Temizer, K. Terada, and J. Kato, “Microscopic design and optimization of hydrodynamically lubricated dissipative interfaces,” *International Journal for Numerical Methods in Engineering*, vol. 120, pp. 153–178, 06 2019.

[88] K. Svanberg, “The method of moving asymptotes—a new method for structural optimization,” *International Journal for Numerical Methods in Engineering*, vol. 24, pp. 359–373, 02 1987.

[89] K. Svanberg, “A class of globally convergent optimization methods based on conservative convex separable approximations,” *SIAM Journal on Optimization*, vol. 12, pp. 555–573, 01 2002.

[90] S. Pekol, O. Kilinc, and I. Temizer, “A Computational Design Framework for Lubrication Interfaces with Active Micro-Textures,” *Journal of Tribology*, pp. 1–30, 07 2024.

[91] G. Kabacaoğlu and I. Temizer, “Homogenization of soft interfaces in time-dependent hydrodynamic lubrication,” *Computational Mechanics*, vol. 56, pp. 421–441, 07 2015.

[92] M. Kane and B. Bou-Saïd, “A study of roughness and non-newtonian effects in lubricated contacts,” *Journal of Tribology*, vol. 127, pp. 575–581, 06 2005.

[93] C. J. A. Roelands, J. C. Vlugter, and H. I. Waterman, “The viscosity-temperature-pressure relationship of lubricating oils and its correlation with chemical constitution,” *Journal of Basic Engineering*, vol. 85, p. 601–607, 12 1963.

[94] S. Bair, “Generalized newtonian viscosity functions for hydrodynamic lubrication,” *Tribology International*, vol. 117, p. 15–23, 01 2018.

[95] C. Arcoumanis, P. Ostovar, and R. Mortier, “Mixed lubrication modelling of newtonian and shear thinning liquids in a piston-ring configuration,” *SAE Technical Papers*, 10 1997.

[96] H. Eyring, “Viscosity, plasticity, and diffusion as examples of absolute reaction rates,” *The Journal of Chemical Physics*, vol. 4, pp. 283–291, 04 1936.

[97] M. Khonsari and D. Hua, “Generalized non-newtonian elastohydrodynamic lubrication,” *Tribology International*, vol. 26, pp. 405–411, 12 1993.

[98] S. Bair and W. O. Winer, “A rheological model for elastohydrodynamic contacts based on primary laboratory data,” *Journal of Lubrication Technology*, vol. 101, p. 258–264, 07 1979.

[99] C. Venner and J. Bos, “Effects of lubricant compressibility on the film thickness in ehl line and circular contacts,” *Wear*, vol. 173, pp. 151–165, 04 1994.

[100] D. Dowson and G. R. Higginson, “Elasto-hydrodynamic lubrication,” *Elsevier eBooks*, 01 1977.

[101] M. Protter and C. J. Morrey, *A First Course in Real Analysis.* Springer Science & Business Media, 12 2012.

[102] N. Brunetière and A. Francisco, “Multiscale modeling applied to the hydrodynamic lubrication of rough surfaces for computation time reduction,” *Lubricants*, vol. 6, p. 83, 09 2018.

[103] Y. Efendiev, T. Hou, S. Antman, J. Marsden, L. Sirovich, W. Yalchin, A. Thomas, and Y. Hou, *Multiscale Finite Element Methods.* Springer Nature, 01 2009.

[104] Y. Xie, Y. Li, S. Suo, X. Liu, J. Li, and Y. Wang, “A mass-conservative average flow model based on finite element method for complex textured surfaces,” *Science China. Physics, Mechanics & Astronomy*, vol. 56, pp. 1909–1919, 09 2013.

[105] B. Nilsson and P. Hansbo, “Adaptive finite element methods for hydrodynamic lubrication with cavitation,” *International Journal for Numerical Methods in Engineering*, vol. 72, pp. 1584–1604, 04 2007.

[106] G. Bayada and M. Jai, "Application of the homogenization to thin film gas lubrication," *Tribology Series*, vol. 31, pp. 433–440, 01 1996.

Appendix A

Additional Minimization Textures

A.1 Energy Dissipation Minimization Textures for PC and ST Fluids

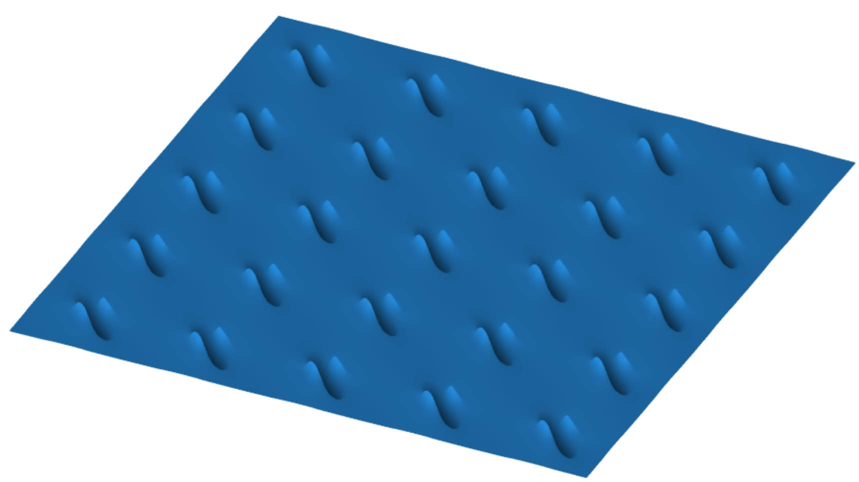

Figure A.1: Dimple Texture obtained with triangular sectoring of a single region for Shear-Thinning fluid.

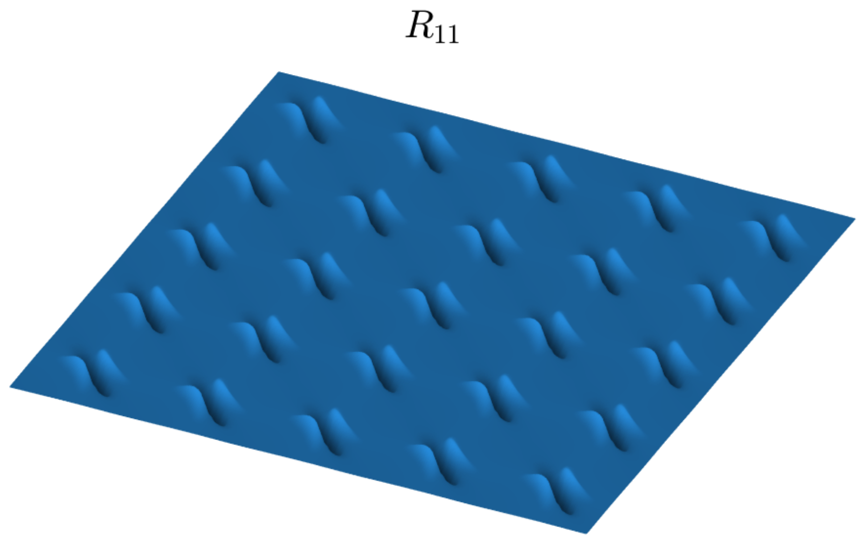

Figure A.2: Dimple Texture obtained with triangular sectoring of a single region for Piezoviscous & Compressible fluid.

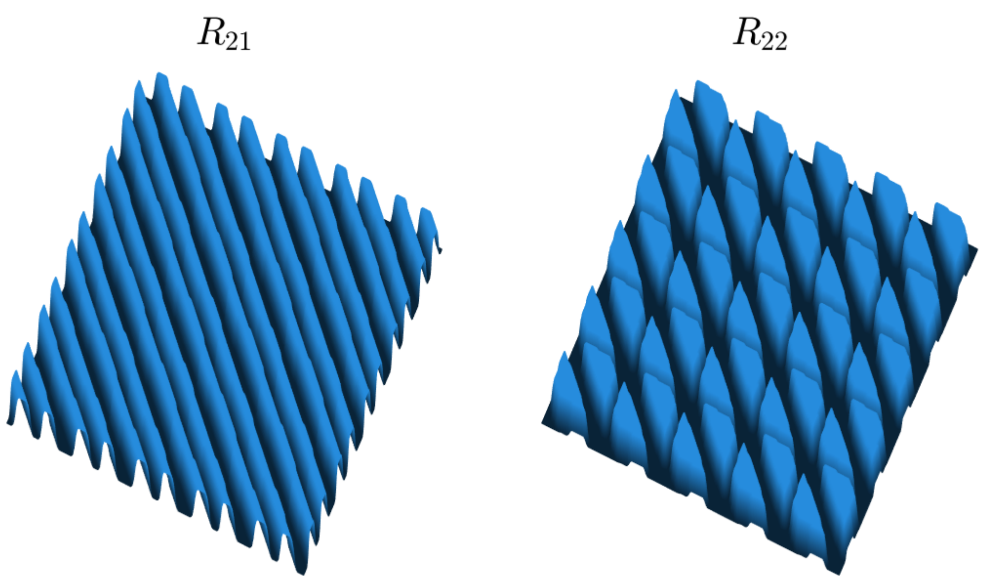

Figure A.3: Dimple Textures obtained with triangular sectoring of 2 region partition for Shear-Thinning fluid.

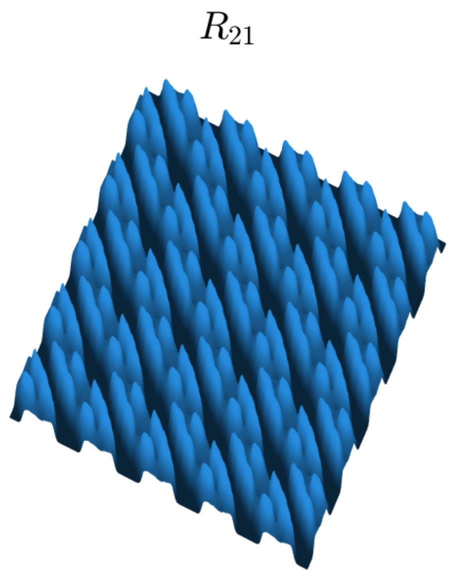

Figure A.4: Dimple Textures obtained with triangular sectoring of 2 region partition for Piezoviscous & Compressible fluid.

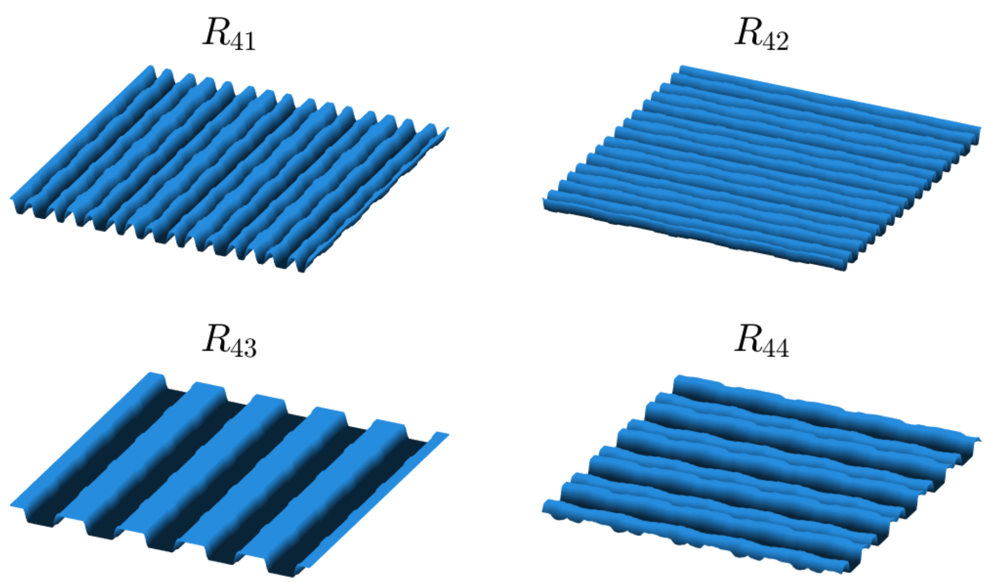

Figure A.5: Dimple Textures obtained with triangular sectoring of 4 region partition for Shear-Thinning fluid.

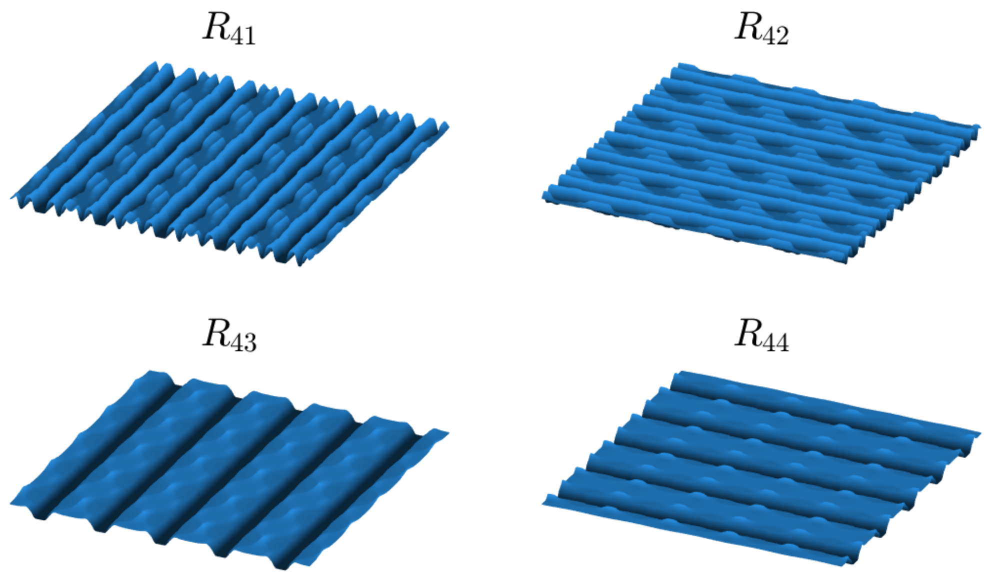

Figure A.6: Dimple Textures obtained with triangular sectoring of 4 region partition for Piezoviscous & Compressible fluid.

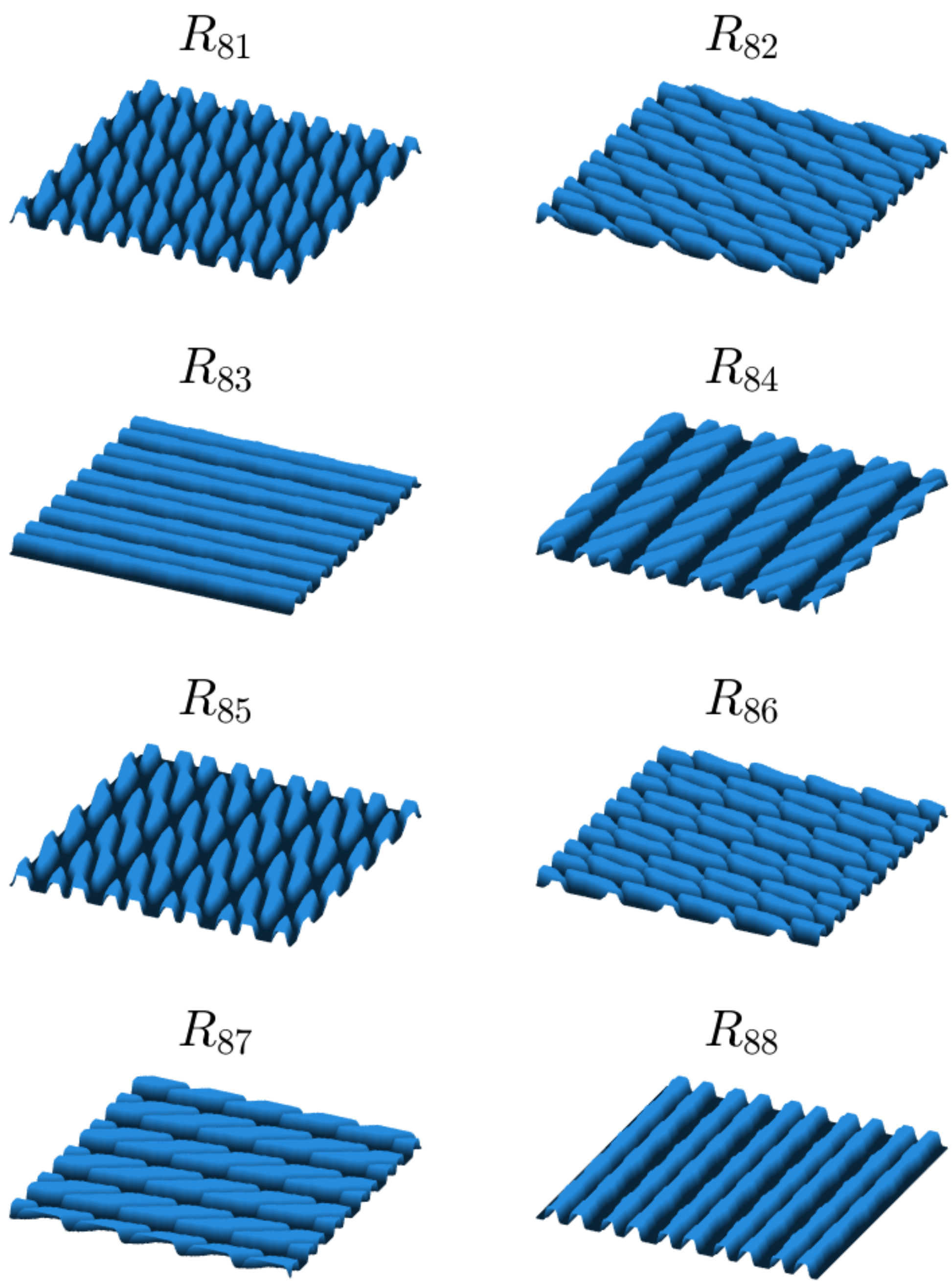

Figure A.7: Dimple Textures obtained with triangular sectoring of 8 region partition for Shear-Thinning fluid.

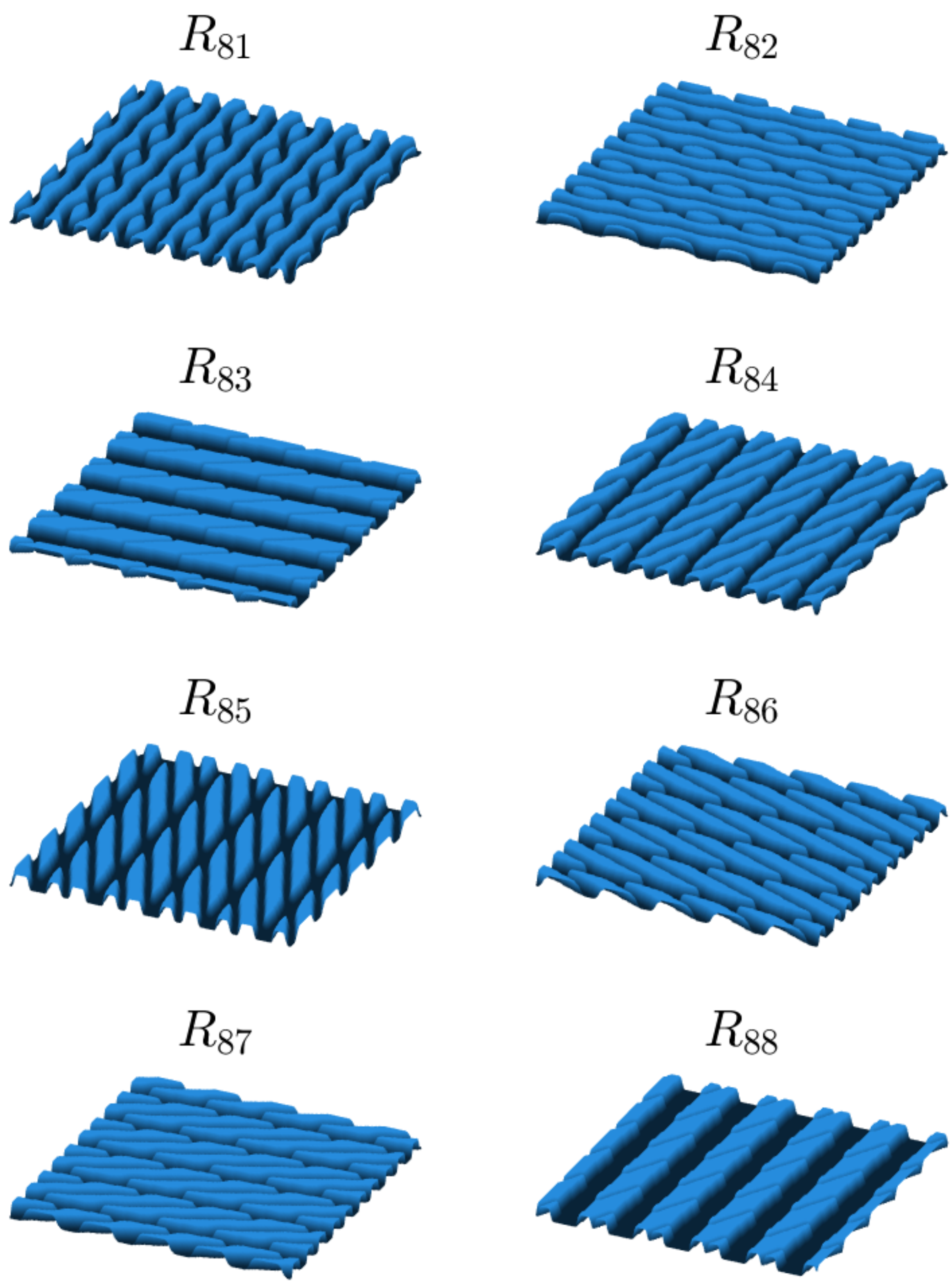

Figure A.8: Dimple Textures obtained with triangular sectoring of 8 region partition for Piezoviscous & Compressible fluid.

Appendix B

OpenFoam Solvers

B.1 Newtonian Solver

```
/*---------------------------------------------------------------------------*\
  =========                 |
  \\      /  F ield         | OpenFOAM: The Open Source CFD Toolbox
   \\    /   O peration     | Website: https://openfoam.org
    \\  /    A nd           | Copyright (C) 2011-2021 OpenFOAM Foundation
     \\/     M anipulation  |
-------------------------------------------------------------------------------
License
    This file is part of OpenFOAM.

    OpenFOAM is free software: you can redistribute it and/or modify it
    under the terms of the GNU General Public License as published by
    the Free Software Foundation, either version 3 of the License, or
    (at your option) any later version.

    OpenFOAM is distributed in the hope that it will be useful, but
        WITHOUT
```

```
    ANY WARRANTY; without even the implied warranty of MERCHANTABILITY or
    FITNESS FOR A PARTICULAR PURPOSE.  See the GNU General Public License
    for more details.

    You should have received a copy of the GNU General Public License
    along with OpenFOAM.  If not, see <http://www.gnu.org/licenses/>.

Application
    icoFoam

Description
    Transient solver for incompressible, laminar flow of Newtonian fluids.

\*---------------------------------------------------------------------------*/

#include "fvCFD.H"
#include "pisoControl.H"

// * * * * * * * * * * * * * * * * * * * * * * * * * * * * * * * * * * * * //

int main(int argc, char *argv[])
{
    #include "setRootCaseLists.H"
    #include "createTime.H"
    #include "createMesh.H"

    pisoControl piso(mesh);

    #include "createFields.H"
    #include "initContinuityErrs.H"
```

```
// * * * * * * * * * * * * * * * * * * * * * * * * * * * * * * * *
   * * * //

Info<< "\nStarting time loop\n" << endl;

const dimensionedScalar ptol = dimensionedScalar("ptol",
   p.dimensions(), 1e-9);
const dimensionedScalar utol = dimensionedScalar("utol",
   U.dimensions(), 1e-7);

while (runTime.loop())
{
   Info<< "Time = " << runTime.userTimeName() << nl << endl;

   #include "CourantNo.H"

   pAtPreviousStep = p;
   UAtPreviousStep = U;

   // Momentum predictor

   fvVectorMatrix UEqn
   (
      fvm::ddt(U)
    + fvm::div(phi, U)
    - fvm::laplacian(nu, U)
   );

   if (piso.momentumPredictor())
   {
      solve(UEqn == -fvc::grad(p));
   }

   // --- PISO loop
   while (piso.correct())
```

```
{
    volScalarField rAU(1.0/UEqn.A());
    volVectorField HbyA(constrainHbyA(rAU*UEqn.H(), U, p));
    surfaceScalarField phiHbyA
    (
        "phiHbyA",
        fvc::flux(HbyA)
      + fvc::interpolate(rAU)*fvc::ddtCorr(U, phi)
    );

    adjustPhi(phiHbyA, U, p);

    // Update the pressure BCs to ensure flux consistency
    constrainPressure(p, U, phiHbyA, rAU);

    // Non-orthogonal pressure corrector loop
    while (piso.correctNonOrthogonal())
    {
        // Pressure corrector

        fvScalarMatrix pEqn
        (
            fvm::laplacian(rAU, p) == fvc::div(phiHbyA)
        );

        pEqn.setReference(pRefCell, pRefValue);

        pEqn.solve();

        if (piso.finalNonOrthogonalIter())
        {
            phi = phiHbyA - pEqn.flux();
        }
    }
```

```
            #include "continuityErrs.H"

            U = HbyA - rAU*fvc::grad(p);
            U.correctBoundaryConditions();
        }
    //convTerm = div(phi, U);
    //viscTerm = laplacian(nu, U);
        runTime.write();

        Info<< "ExecutionTime = " << runTime.elapsedCpuTime() << " s"
            << "  ClockTime = " << runTime.elapsedClockTime() << " s"
            << nl << endl;

        if (Foam::sum(Foam::mag(p - pAtPreviousStep)) < ptol &&
            Foam::sum(Foam::mag(U - UAtPreviousStep)) < utol)
        {
            Info << "Steady State Reached At: " << runTime.value() <<
                nl;
            runTime.writeNow();
            break;
        }
    }


    Info<< "End\n" << endl;

    return 0;
}


//
    ************************************************************************
    //
```

B.2 Non-Newtonian Solver (Piezoviscous and Shear-Thinning)

```
/*---------------------------------------------------------------------------*\
  =========                 |
  \\      /  F ield         | OpenFOAM: The Open Source CFD Toolbox
   \\    /   O peration     |
    \\  /    A nd           | Copyright (C) 2011-2016 OpenFOAM Foundation
     \\/     M anipulation  |
-------------------------------------------------------------------------------
License
    This file is part of OpenFOAM.

    OpenFOAM is free software: you can redistribute it and/or modify it
    under the terms of the GNU General Public License as published by
    the Free Software Foundation, either version 3 of the License, or
    (at your option) any later version.

    OpenFOAM is distributed in the hope that it will be useful, but
        WITHOUT
    ANY WARRANTY; without even the implied warranty of MERCHANTABILITY
        or
    FITNESS FOR A PARTICULAR PURPOSE.  See the GNU General Public License
    for more details.

    You should have received a copy of the GNU General Public License
    along with OpenFOAM.  If not, see <http://www.gnu.org/licenses/>.

Application
    nonNewtonianIcoFoam

Description
    Transient solver for incompressible, laminar flow of non-Newtonian
        fluids.
```

```
\*---------------------------------------------------------------------------*/

#include "fvCFD.H"
#include "pisoControl.H"
#include "fvModels.H"

// * * * * * * * * * * * * * * * * * * * * * * * * * * * * * * * * * * *
   * * * //

int main(int argc, char *argv[])
{
    #include "postProcess.H"

    #include "setRootCase.H"
    #include "createTime.H"
    #include "createMeshNoClear.H"
    #include "createControl.H"
    #include "createFields.H"
    #include "initContinuityErrs.H"

    // * * * * * * * * * * * * * * * * * * * * * * * * * * * * * * * * *
        * * * //

    Info<< "\nStarting time loop\n" << endl;


    const scalar z = lubricationProperties.lookupOrDefault("z", 0.0);
    const scalar p0 = lubricationProperties.lookupOrDefault("p0", 0.0)
        / ambientDensity;

    const dimensionedScalar c1 = dimensionedScalar("c1",
        p.dimensions(), 1.0);
    const dimensionedScalar c2 = dimensionedScalar("c2",
        nu.dimensions(), 1.0);
```

```
const dimensionedScalar c3 = dimensionedScalar("c3", dimTime, 1.0);

const scalar c4 = 2.0;
const scalar c5 = 7.0e6;

const dimensionedScalar tau0 = dimensionedScalar("tau0",
    p.dimensions(), c5 / ambientDensity);
const dimensionedScalar c6 = dimensionedScalar("c1",
    nu.dimensions(), 1.0);

const dimensionedScalar ptol = dimensionedScalar("ptol",
    p.dimensions(), 1e-9);
const dimensionedScalar utol = dimensionedScalar("utol",
    U.dimensions(), 1e-7);

const bool piezo =
    lubricationProperties.lookupOrDefault<bool>("piezo", false);
const bool shear =
    lubricationProperties.lookupOrDefault<bool>("shear", false);

if (piezo)
{
    Info << "Piezo-viscosity: Enabled" << nl;
} else {
    Info << "Piezo-viscosity: Disabled" << nl;
}

if (shear)
{
    Info << "Shear-thinning: Enabled" << nl;
} else {
    Info << "Shear-thinning: Disabled" << nl;
}
```

```
const bool adjustTimeStep =
    runTime.controlDict().lookupOrDefault("adjustTimeStep", false);
scalar maxCo =
    runTime.controlDict().lookupOrDefault<scalar>("maxCo", 1.0);
scalar maxDeltaT =
    runTime.controlDict().lookupOrDefault<scalar>("maxDeltaT",
    0.025);

while (runTime.loop())
{

    Info<< "Time = " << runTime.timeName() << nl << endl;

    #include "CourantNo.H"
   //#include "setDeltaT.H"

    //Debugging Kinematic Viscosity Function


    if (piezo)
    {
        dimlessP = p / c1;
        dimlessNu = ambientViscosity *
            Foam::exp((Foam::log(ambientViscosity * ambientDensity)
            + 9.67) * (-1.0 + Foam::pow((1.0 + dimlessP / p0), z)));
            //ambientViscosity
        nu = dimlessNu * c2;
    }

    if (shear)
    {
        strainRate = Foam::sqrt(c4) * mag(symm(fvc::grad(U)));
        nu = nu * (1 - Foam::pow(Foam::tanh(strainRate * nu /
            tau0), 2.0));
    }
```

```
Info << "Maximum Kinematic Viscosity: " <<
    Foam::max(mag(dimlessNu)) << nl;

pAtPreviousStep = p;
UAtPreviousStep = U;

//End Kinematic Viscosity Calcualtion

//fluid.correct();

// Momentum predictor

fvVectorMatrix UEqn
(
    fvm::ddt(U)
  + fvm::div(phi, U)
  - fvm::laplacian(nu, U)
  - (fvc::grad(U) & fvc::grad(nu))
);


if (piso.momentumPredictor())
{
    solve(UEqn == -fvc::grad(p));
}

// --- PISO loop
while (piso.correct())
{
    volScalarField rAU(1.0/UEqn.A());
    volVectorField HbyA(constrainHbyA(rAU*UEqn.H(), U, p));
    surfaceScalarField phiHbyA
    (
```

```
            "phiHbyA",
            fvc::flux(HbyA)
          + fvc::interpolate(rAU)*fvc::ddtCorr(U, phi)
        );

        adjustPhi(phiHbyA, U, p);

        // Update the pressure BCs to ensure flux consistency
        constrainPressure(p, U, phiHbyA, rAU);

        // Non-orthogonal pressure corrector loop
        while (piso.correctNonOrthogonal())
        {
            // Pressure corrector

            fvScalarMatrix pEqn
            (
                fvm::laplacian(rAU, p) == fvc::div(phiHbyA)
            );

            pEqn.setReference(pRefCell, pRefValue);

            pEqn.solve();

            if (piso.finalNonOrthogonalIter())
            {
                phi = phiHbyA - pEqn.flux();
            }
        }

        #include "continuityErrs.H"

        U = HbyA - rAU*fvc::grad(p);
        U.correctBoundaryConditions();
    }
```

```
        runTime.write();

        Info<< "ExecutionTime = " << runTime.elapsedCpuTime() << " s"
            << "  ClockTime = " << runTime.elapsedClockTime() << " s"
            << nl << endl;

        if (Foam::sum(Foam::mag(p - pAtPreviousStep)) < ptol &&
            Foam::sum(Foam::mag(U - UAtPreviousStep)) < utol)
        {
            Info << "Steady State Reached At: " << runTime.value() <<
                nl;
            runTime.writeNow();
            break;
        }
    }

    Info<< "End\n" << endl;

    Info << "Maximum Pressure: " << Foam::max(mag(p));

    Info << "p0 = " << p0 << nl;

    return 0;
}


//
    ************************************************************************
    //
```